論文 / 著書情報
Article / Book Information

題目(和文)	量子情報処理に向けた表面弾性波駆動単一電子輸送
Title(English)	Surface Acoustic Wave-Driven Single-Electron Transport for Quantum Information Processing
著者(和文)	太田俊輔
Author(English)	Shunsuke Ota
出典(和文)	学位:博士(工学), 学位授与機関:東京工業大学, 報告番号:甲第12697号, 授与年月日:2024年3月26日, 学位の種別:課程博士, 審査員:小寺 哲夫,波多野 睦子,若林 整,岩﨑 孝之,藤澤 利正,山本 倫久
Citation(English)	Degree:Doctor (Engineering), Conferring organization: Tokyo Institute of Technology, Report number:甲第12697号, Conferred date:2024/3/26, Degree Type:Course doctor, Examiner:,,,,,
学位種別(和文)	博士論文
Type(English)	Doctoral Thesis

Surface Acoustic Wave-Driven Single-Electron Transport for Quantum Information Processing

Shunsuke Ota

A dissertation submitted for
the degree of Doctor of Engineering

Supervised by
Associate Professor Tetsuo Kodera

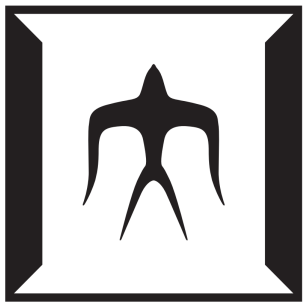

TOKYO INSTITUTE OF TECHNOLOGY

2023

Abstract

This thesis explores surface acoustic wave (SAW)-driven single-electron transport as a fundamental tool for quantum information processing. It thoroughly examines the stability of SAW-driven single-electron transport and demonstrates the first-ever location-specific electron transport by SAWs. Building on this pivotal work, the study develops an on-demand single-electron source using a newly developed single-pulse SAW technique, offering insights into the dynamics of moving electric potentials. Additionally, as an important improvement, we make efforts to analyze and reduce the effects of crosstalk from SAW generator circuits, an essential aspect for achieving accuracy in electron transport. These advances significantly improve single electron transport methodologies using SAWs for electron-quantum optics, contributing to the rapidly developing field of quantum information transport with electron shuttling, paving the way for future innovations in quantum information technology.

Contents

Chapter 1

Introduction

1.1 Quantum information processing

Development of the semiconductor industry has led to miniaturization of basic device dimensions of computers, which has resulted in remarkable progress in achieving higher speeds, lower power consumption, and higher integration. As a result, the scale at which quantum effects can no longer be ignored is fast approaching, and quantum information processing devices are attracting attention. Quantum computers, which perform quantum information processing to manipulate and transmit information based on the principles of quantum mechanics, are a next-generation technology that will bring a major breakthrough to today's information society [DI00]. In classical computers, the information is described by the smallest unit that takes a value of 0 or 1, called a bit, and as many states as there are bits can be represented (2^N states with N bits), but only one state of information can be represented at a given moment. On the other hand, in a quantum computer, the information is described by a wavefunction consisting of superposition of two states

($|0>$ and $|1>$). When there are N quantum bits (qubits), it is possible to have information in all of the 2^N possible combinations at a given moment. Research on quantum computing began in the 1960s [MR14], but it was not clear whether they could perform faster calculations than classical computers, so mostly theoretical research was conducted [Ben80, IY88]. However, the situation changed dramatically in 1994 when Peter W. Shor of Bell Laboratories demonstrated a quantum algorithm that can solve prime factorization at high speed with a very small error probability [Sho94]. The prime factorization of integers with a large number of digits cannot be performed on a realistic time scale even with the most powerful supercomputers, which guarantees the security of public key cryptosystems such as RSA. However, if a quantum computer is realized, prime factorization will be executed at high speed, and the security of cryptography will be ruined, which will have an extremely large social impact. For this reason, experiments with quantum computers in real physical systems have been accelerated. In 2019, Google succeeded in solving a computational problem that would take the world's fastest supercomputer 10,000 years to solve in 3 minutes and 20 seconds with a quantum computer that uses superconductivity. They announced that this demonstrated quantum supremacy for the first time in the world [AAB$^+$19]. There are various candidates for systems to realize quantum computers, including trapped ions [CZ95], neutral atoms [BCJ$^+$00], photons [KLM01], and electrons and holes in semiconductors [LD98], as well as superconducting circuits [NPT99]. Other major information technology companies such as IBM and Intel, and start-ups, are developing quantum computers using their own methods. Recently, IBM announced the "IBM Quantum Condor," a processor with 1121 qubits. Atom Computing has also announced a processor with 1180 qubits. So quantum computers

with more than 1000 qubits are now available. In addition, some quantum computers are already available as computing resources via the cloud. In this way, some of these systems are beginning to see utilization at the level of Noisy Intermediate-Scale Quantum devices (NISQ): quantum computers that perform quantum computations without error corrections, where cumulative errors mainly limit the scale of the quantum calculations. Nevertheless, it is considered to be meaningful for some practical calculations, such as quantum simulations [FMMC12]. However, in order to perform massively parallel computations, such as Shor's algorithm, it is essential to realize a large-scale fault-tolerant quantum computer. To accomplish this, there are still many milestones to be reached in each method, such as the realization of high-fidelity qubits and their large-scale integration, and the optimization of the operation and readout electronics. Among the studies aiming to achieve such milestones, in realizing large-scale integration of qubits, the connection of more and distant qubits and the generation and manipulation of entanglement between distant qubits are the key elements [FMT$^+$17, MBP$^+$18, SSX$^+$22, LKF$^+$23]. In other words, how to transmit quantum information coherently over long distances is required. In this vein, surface acoustic waves (SAWs), which have been shown to be able to transport electrons and their spins coherently and efficiently over long distances of more than μm [TEL$^+$19, BHT$^+$16, JMC$^+$21], have attracted particular attention as one approach in electron flying qubits and long-range connections between spin qubits.

1.2 Electron flying qubit

SAW-driven single-electron transport technology focuses on electrons in semiconductors and is attracting attention as one approach to electron flying qubits. Flying

qubits were initially intended to serve as communication links within a quantum computer [DI00], but recent research has shown that they can also function as stand-alone quantum processing units by manipulating photon number states in flight [PMS$^+$14]. With advances in photonic quantum computation [KLM01, KMN$^+$07], flying qubits are typically associated with photons [Lod17] and can in principle be scaled to millions of qubits, especially through the use of "time multiplexed" architectures. However, photons do not interact with each other, which poses difficulties for two-qubit gates that require interaction. On the contrary, flying qubit architectures can be built using other quantum systems such as electrons, which can be directly entangled via Coulomb interaction [BGM$^+$18, EWO$^+$21]. An electron flying qubit is defined by the presence of a single electron in two transport pathways. This quantum state is depicted on the Bloch sphere, with the classical states where the electron is in one of the two transport paths represented by the north and south poles of the sphere, and the probabilities of these states represented by the angular coordinates of the sphere θ and ϕ that make up the quantum state ψ:

$$|\psi\rangle \propto \cos\left(\frac{\theta}{2}\right)|0\rangle + \sin\left(\frac{\theta}{2}\right) \cdot \exp(i\phi)|1\rangle \tag{1.1}$$

The quantum states of flying electrons are fully controllable through an electron Mach-Zehnder interferometer setup, where the states of flying qubits undergo periodic oscillations due to coherent tunneling within the tunnel coupling region and the quantum phase is tuned by the potential and magnetic flux [YTB$^+$12]. A major challenge for the future is to perform such quantum state control at the level of single electrons and to generate non-local entangled quantum states by combining multiple electron flying qubits.

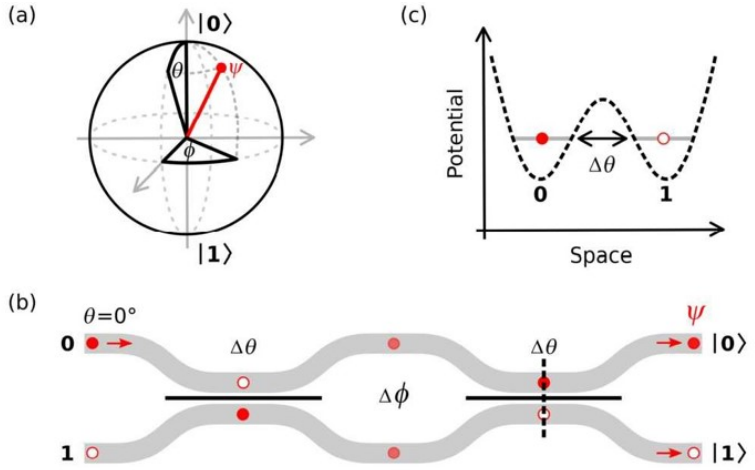

Figure 1.1: Electron flying qubit. **(a)** Bloch sphere showing the qubit state ψ defined by θ and ϕ. θ and ϕ can be controlled by the tunnel coupling and the phase shift, respectively. **(b)** Schematic of an electron two-path interferometer allowing precise adjustment of the qubit state via tunnel-coupling ($\delta\theta$) and the quantum phase ($\delta\phi$) picked up along transport across the central island. **(c)** Transverse potential landscape across the tunnel-coupling region with schematic indications of the qubit basis 0 and 1. This figure is adopted from [EWO+21]

1.3 Long-range connections between semiconductor spin qubits

As another approach, it has been shown that electron spins can be transported coherently by SAWs [BHT+16, JMC+21], making it a promising long-range connections between semiconductor spin qubits. Electron spins in semiconductor quantum dots (QDs) have attracted a great deal of attention because of their high coherence and affinity with long-cultivated semiconductor integration technologies, making them an advantageous system for large-scale and highly integrated applications. Spin qubits, where the spin-up (-down) state corresponds to 0 (1) state of a qubit, are expected to have high bit performance and integration, making them attractive as a physical system for quantum computing, and they are being actively studied. In the realization of a quantum computer, it is necessary to consider not only the integration of qubits but also the integration of

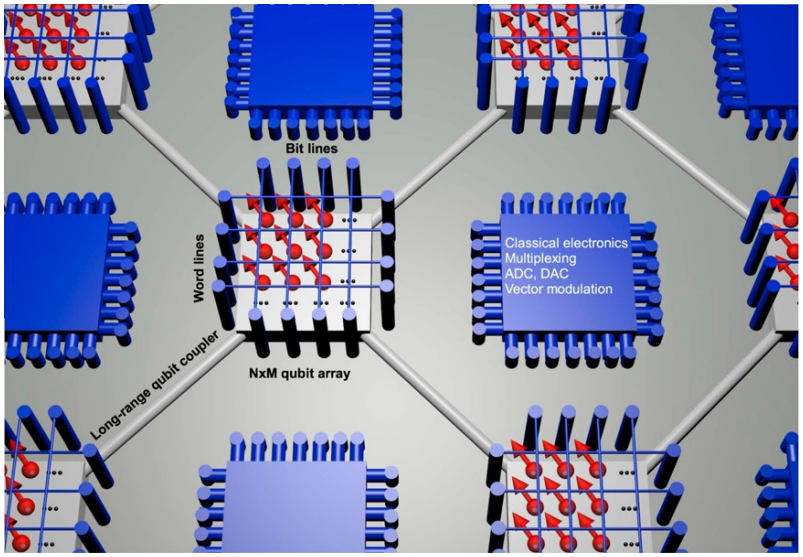

Figure 1.2: Sparse qubit array with local electronics. Long-distance qubit coupling opens up space for local electronics that can control a small dense qubit array. This figure is adopted from [VBC+17]

systems for manipulating and reading out spin states. Therefore, a proposal has been made to integrate such subsystems with multiple qubits in a qubit cluster as the smallest unit [VBC+17]. High scalability can be achieved by combining multiple clusters that are independent as a system. The challenge here is to develop a technology to connect the qubits separated by tens to hundreds of micrometers, which is necessary for the coupling between clusters, and the development of this technology is the key to the realization of a spin quantum computer.

1.4 Surface acoustic waves for quantum information processing devices

SAWs are a versatile phononic technology widely used in both industrial applications and basic research [DCS+19]. The technology for generating SAWs in electronic devices is mature, and SAW-generating devices are static, reliable, and can be fabricated stably

with lithographic techniques. Furthermore, since the speed of sound is much slower than the speed of light, the wavelength at the same frequency is 5 orders of magnitude shorter, making the devices smaller and thus easier to integrate into electronic devices. For these reasons, in industry, for example, nearly 100 frequency filters using SAWs are used in a wireless communication device such as a smartphone [IEE], SAW gas sensors have been introduced by gas manufacturers and semiconductor equipment manufacturers[YAN+10], and SAWs are used for the sensing and mixing of trace amounts of liquids [GARC17]. Alongside these industrial applications, the use of SAWs in basic research in the quantum field has recently been attracting attention. Elastic effects such as the piezoelectric effect can be used to couple with various degrees of freedom in solid-state devices, and studies have been reported in various fields. For example, applications to spin currents [KYM+17] and skyrmion generation [YSR+20] in the field of spintronics, coupling to superconducting qubits [GAK+14, MKP+17, NYTN17, MSVL18, BZK+18] and beam splitter development [QDA+23] in the field of quantum acoustics have been explored. Furthermore, in the field of electron-quantum optics, various studies have been conducted based on SAW-based single-electron transport techniques [HTY+11, MKF+11, SHSP05, BHT+16, TEL+19, JMC+21, ITL+21, EWO+21, WOE+22, WER+23]. One of the main goals of these studies is the development of next-generation quantum information processing devices.

1.5 Motivation of our work

In this thesis, we report our advancements in solving the essential problems of the SAW-driven single electron transport technique and to advance this technique. This tech-

nology enables precise manipulation of single electrons confined in nanoscale QDs using SAWs, and is attracting attention as an important component of quantum computers. However, several technical challenges exist at this stage. First, the fact that the shape of the SAW is generally sinusoidal and has a fixed time width limits the degree of freedom of transport operation. This constraint compromises the flexibility of electron transport. In addition, components of the SAW that are not directly involved in electron transport may have unwanted effects on the system, and techniques must be developed to eliminate them. Second, the physical mechanism of the electron transport process by SAWs has not been fully elucidated. In particular, the precise positional information of the electrons in the transport process is unclear, which causes uncertainty regarding the synchronous transport of electrons. This synchronization uncertainty is an important issue from the viewpoint of accurate manipulation of qubits. In this study, we provide a detailed analysis and propose solutions to these issues. In particular, we demonstrate position-specific transport of electrons to realize synchronous transport of electrons (Chapter 3), as well as the generation of SAW pulses optimized for single-electron transport (Chapter 2) and the application of this to a single-electron source based on a new operating principle (Chapter 4). In addition, a series of studies have provided insight into the significant adverse effects of electromagnetic crosstalk on the system. To address this issue, we proposed and demonstrated a new generation principle of SAWs that suppresses electromagnetic waves (Chapter 5). Through these improvements, we have enabled the simultaneous manipulation of multiple single electrons, further enhanced the scalability of the system, and advanced the SAW-driven single electron transport technique. These advances will be an important step toward the realization of SAW-based quantum information processing

devices.

1.6 This thesis

This thesis consists of six chapters. Next to this chapter (Chapter 1 ”Introduction”), in Chapter 2 ”Optimization of surface acoustic wave generation”, we summarize two experimental optimizations performed on SAW generation: material selection of interdigital transducers (IDTs) and development of single-cycle SAW pulse generation techniques. These optimizations are crucial to the success of the experiments in the chapters behind. It also describes the basic information and technique about the SAW generation and detection which form the basis for the experiments in the other chapters. In Chapter 3 ”In-flight distribution of an electron within a surface acoustic wave”, we demonstrate position-specific transport of electrons by performing time-of-flight measurements of single electrons transported via SAW trains between distant QDs by employing a SAW, obtained in Chapter 2, with a stronger confinement effect than the conventional one. In Chapter 4 ”On-demand single-electron source via single-cycle acoustic pulses”, we employ a single-cycle SAW pulse developted in Chapter 2 in a much simpler way – without any QD at the entrance or exit of a transport channel - to perform single-electron transport between distant electron reservoirs. The single-electron source we developed can emit single electrons on-demand with arbitrary delays on a ns time scale, due to the simplicity of our approach. In Chapter 5 ”Suppression of electromagnetic crosstalk by differential excitation for surface acoustic wave generation”, we addressed the persistent problem of electromagnetic crosstalk, as identified in Chapter 4. We studied a differential excitation method for IDTs to generate SAWs while reducing electromagnetic waves, and proposed

and demonstrated an essential solution: suppressing the generation of electromagnetic waves themselves. Finally, we summarize the results in this thesis and discuss the perspectives for applications in quantum information processing devices in the last chapter (Chapter 6, ”Conclusion and perspectives”)

Chapter 2

Optimization of surface acoustic wave generation method

In this chapter, we summarize two experimental optimizations performed on SAWs generation: material selection of IDTs and development of pulsed SAW generation techniques. It also describes an introduction to SAWs, and the design and fabrication of IDTs for SAW generation and detection and their measurement methods, as well as SAW generation and detection experiments, which form the basis for the experiments in the other chapters.

2.1 Introduction

We introduce a brief history, the basic properties of SAWs, and the SAW-driven single electron transport technique. SAWs were first reported mathematically by Lord Rayleigh in 1855 [Ray85]. The SAWs, often called Rayleigh waves, propagate across the free surface of an elastic solid at the sound speed specific to each material. SAWs have been

playing a major role in the development of seismology as waves propagating through the Earth's surface. However, in 1965, White and Voltmer proposed the IDT as a generator and receiver of SAWs [WV65], which led to a dramatic advancement in the application of SAWs to electronic devices. Basically, IDT has a very simple structure and fabrication method, so it was easy and inexpensive to create devices using the lithography technology of semiconductor manufacturing. Thereafter, various shapes of devices such as bandpass filters, resonators, oscillators, and matched filters have been developed and commercialized. These devices have been used in many practical systems such as smart phones and wireless devices. SAW devices have become indispensable in our daily lives.

Acoustic waves in solid materials induce a position change of atoms, which is identified as a displacement from the equilibrium state. This change is described quantitatively in term of strains. In the presence of such strain, an internal force is generated in order to return the material to its equilibrium state. This force is expressed in terms of stress. Acoustic waves are a propagation phenomenon consisting of stress and strain. These atoms move in elliptical orbits perpendicular to the surface (see Fig. 2.1), and the direction of this rotation determines the direction of SAW propagation. In counterclockwise rotation, the SAW propagates from left to right. The amplitude of the SAW is maximum at the surface and decays exponentially in the depth direction of the material; most of the power of the SAW is within a wavelength depth from the surface. The generation of SAW using an electrical input signal requires two requirements: a piezoelectric substrate and an interdigital transducer. Piezoelectricity allows electrical signals to be converted into mechanical deformation. When an electric field is applied to a piezoelectric material, a mechanical stress or strain is induced on the surface. This can generate SAWs on

the piezoelectric material. This mechanical deformation also induces an electric field, or voltage. Therefore, SAW propagating on a piezoelectric substrate is accompanied by an electric field. This coupling between the electrical and mechanical parts is important for the single electron transport.

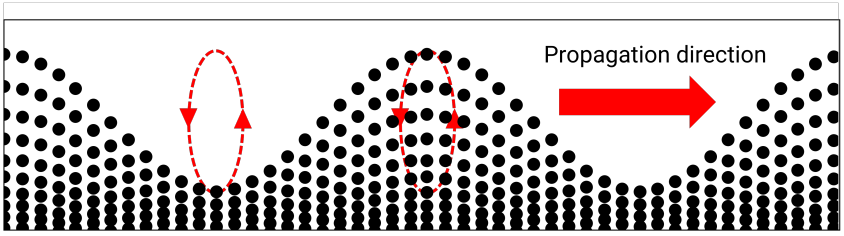

Figure 2.1: Representation of a surface acoustic wave during propagation. The dots represent the positions of the atoms. The dashed arrows represent the elliptical orbits of the atoms, and the straight arrows indicate the direction of SAW propagation.

SAWs excited on piezoelectric materials such as GaAs are accompanied by electric potential waves due to the piezoelectric effect. When SAWs are coupled with electric charges, an interesting property known as the acoustoelectric effect appears [WW57]. This results in an induced current due to the SAW. To be more specific, this is acoustic electron transport across quantum point contact (QPC) with gates as shown in Fig. 2.2. First, a negative voltage is applied to the gate to deplete the two-dimensional electron gas (2DEG) and prohibit the flow of bias drive current. In this state, a current is induced by using a SAW with sufficient power. Furthermore, the acoustoelectric current is found to be quantized in units of ef, where e is the charge of the electron and f is the frequency of the SAW. This is due to the trapping of a fixed number of electrons in the moving minimum of the SAW potential. In this experiment, it is shown that SAWs can induce QD-like confinement potentials along the propagation direction. These moving electric

potentials or QDs can confine and transport electrons at the sound speed. The idea of moving QDs has been applied to many applications. For example, to realize the current standard based on the revised SI [ZK03, Gib17]. The definition of ampere was given by the force generated between two infinitely parallel conductors, which was redefined in 2018 using elementary charges. Now, it is defined by the number of electrons flowing within a second. Quantum current sources using SAWs had been studied for many years [SMT+96, TSP+97, CTS+99, CTS+00, EPA02, PUL03, For17]. SAW-driven single-electron transport is also based on the dynamic QD mechanism. In this case, isolated single electrons in the QD are picked up by the SAW and remain at the potential minimum during transport. An interesting property that makes this system promising is that these electrons are located much higher than the Fermi level, so the interaction with other electrons is prevented during the transport.

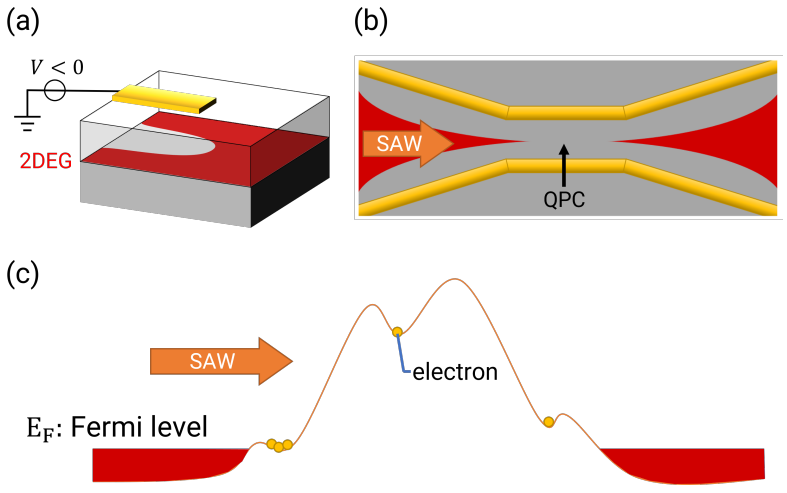

Figure 2.2: **(a)** Schematic diagram of the depletion of the 2DEG (in red) by the metal gate deposited on top of the substrate. **(b)** Top view of the formation of a quantum point contact (QPC). **(c)** Schematic diagram of single electron transport by surface acoustic wave (SAW).

Recently, single-electron transport between QDs over several tens of micrometers has been demonstrated [HTY+11, MKF+11, TEL+19], and coherent transport of electron spin has also been demonstrated [BHT+16, JMC+21].

2.2 Interdigital transducer (IDT)

An IDT consists of comb-shaped electrodes connected to different contacts, either top or bottom (see Fig. 2.3). When a voltage is applied, an electric field is generated in the gap between the metal fingers, causing mechanical strain due to piezoelectricity. When an oscillating voltage with a frequency $f_{\mathrm{SAW}} = v_{\mathrm{SAW}} / \lambda_{\mathrm{IDT}}$ according to the periodicity of the metal fingers of the IDT λ_{IDT} and velocity of SAW v_{SAW} is applied, a SAW with the same frequency f_{SAW} is effciently generated. Fig. 2.3 shows a basic SAW device with two IDTs. When a voltage is applied, a periodic electric field is generated in the input IDT on the left side of the figure, and SAW is generated due to the piezoelectric effect. At the output side, the receiver's output IDT acts in reverse to convert the SAW into an output voltage. In this way, the SAW device operates with only electrical signal input and output. Next, we introduce the IDTs used in this experiment.

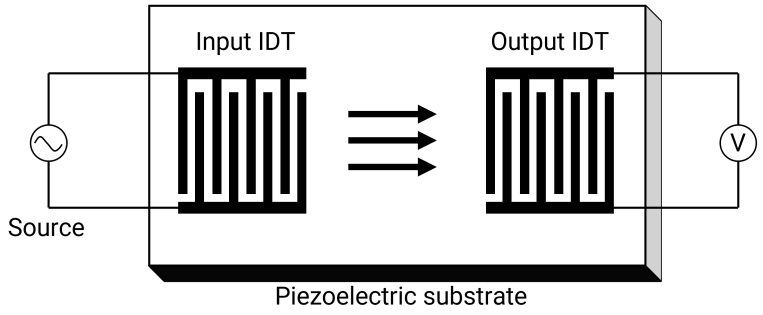

Figure 2.3: A basic surface acoustic wave device.

2.2.1 Single / double finger IDT

The most common IDT is known as a single finger IDT, which has a constant finger periodicity λ and a single resonant frequency f (see Fig. 2.4a). It is a two direction IDT; SAWs are generated and propagated on both sides of the device. Generated SAWs are

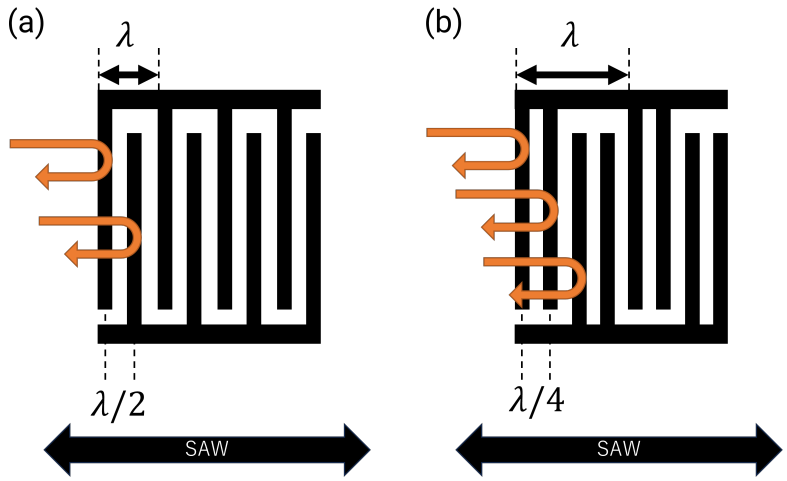

Figure 2.4: Structure of a single finger IDT (a) and a double finger IDT(b). λ is the period of the finger structure.

reflected by electrodes in the IDT. Each electrode only reflects weakly, but if the reflected waves are in phase, the reflection will be larger. In the case of a single finger IDT, the distance between the fingers is half of the wavelength λ of the IDT, so each reflection is added in phase, as shown in Fig. 2.4a. Cavity is created and the SAW is trapped as a standing wave for a certain time until it leaves the structure. This can be problematic if one is aiming for high transmission devices. A solution to this problem is a double finger IDT [BJSS72, VMW72], which has four fingers per period (see Fig. 2.4b). The distance between fingers is $\lambda/4$, and reflections from neighboring electrodes cancel out because their phases are different by 180°. Therefore, trapping acoustic waves can be avoided and it allows for more efficient SAW emission. On the other hand, the disadvantage is that the structure becomes smaller for the same frequency, which reduces the manufacturing resolution.

2.2.2 Chirp IDT

Chirp IDT can excite SAWs with a wide frequency band by varying the period λ of the IDT. In general, it varies linearly from large wavelength to small wavelength. In a

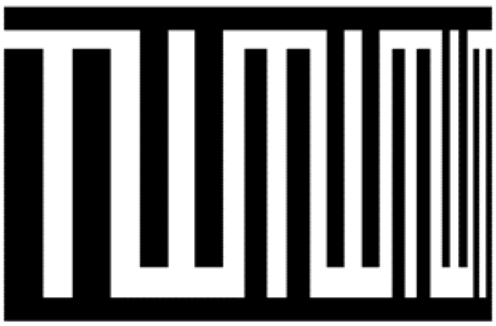

Figure 2.5: Structure of a chirp IDT with a double-finger structure.

recent report, SAWs with a frequency band of $0.2{\sim}1.2\,\mathrm{GHz}$ have been generated, albeit intermittently, by chirping Split-52 IDT [WHZ+18]. In this study, we developed a new chirpe IDT with a double-finger structure and used it for pulsed SAW generation. In the following text, chirp IDT refers to this double-finger ChirpIDT.

2.2.3 Other type of IDT

The specially shaped IDT, called Split52 IDT (see Fig. 2.6a) [SZA+15], consists of two fingers connected to each of the upper and lower contacts, and one floating finger. The distance between fingers is $\lambda/5$, where λ is the period of the IDT. The important feature of this IDT is that it can efficiently excite the frequency f_1 corresponding to the IDT period λ and its harmonics $f_n = nf_1 (n = 2, 3, 4, 6, \dots)$. Another special IDT is the Distributed Acoustic Reflection Transducers (DART) IDT (see Fig. 2.6b) [DSP+19, EAR+17], whose structure includes wider electrodes in width. This asymmetric structure results in stronger

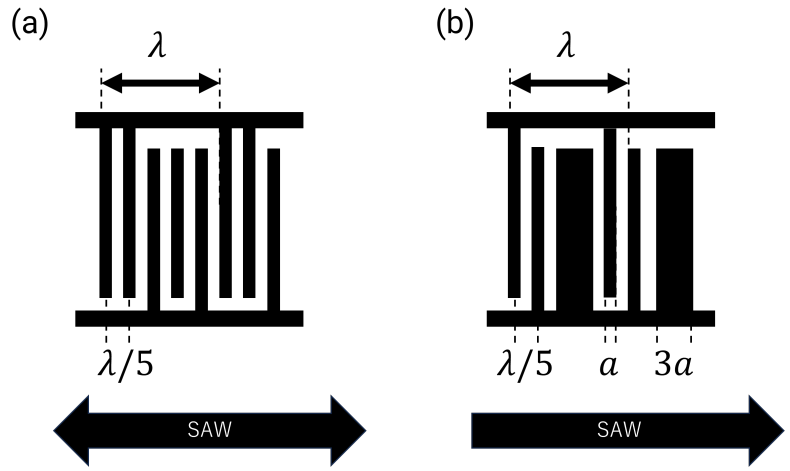

Figure 2.6: Structure of Split52 finger IDT (a) and Distributed Acoustic Reflection Transducers (DART) IDT(b). λ is the period of the finger structure, and a is the width of the finger.

scattering of waves propagating in one direction. Interference with the non-reflecting waves then produces SAW emission in one direction. This increases the transmission efficiency compared to IDTs that emit SAWs in both directions.

2.3 Design of IDT

2.3.1 Periodic structure IDT

In our experiments, the most important parameter for IDT is a wave length λ, which is the finger repetition period of the IDT (see Fig. 2.7). It determines the frequency of the surface acoustic wave f_{SAW} excited by the IDT from the equation $v_{\mathrm{SAW}} = f_{\mathrm{SAW}}\lambda$, where v_{SAW} is a velocity of the SAW. The value of v_{SAW} is almost $3\,\mu\mathrm{m/ns}$ on GaAs. This value varies with the weight of the metal used in the IDT, for example, $v_{\mathrm{SAW}}^{\mathrm{Au}} \approx 2.77\,\mu\mathrm{m/ns}$ for gold transducers, which is well known from former SAW-driven charge transport experiment [TEL+19]. The next most important parameter is the length of the IDT T. We express the length in units of time. This means that the actual length of the IDT

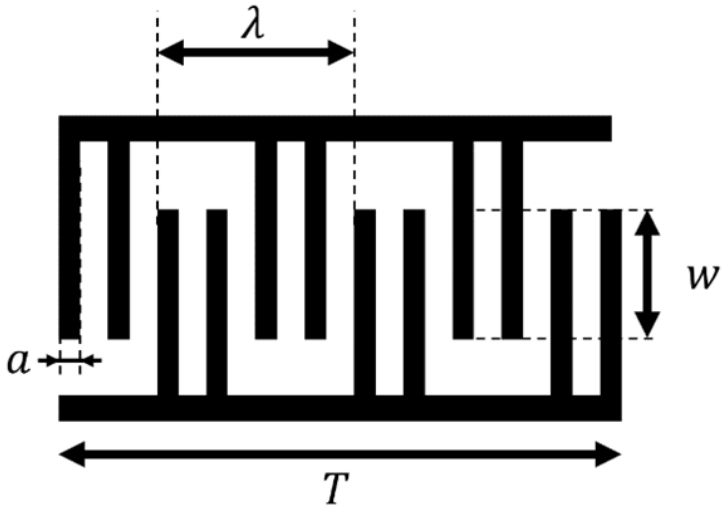

Figure 2.7: IDT design parameters of double finger IDT. The black regions are where metal is deposited.

is $v_{\mathrm{SAW}}T$. The reason for using units of time is that it corresponds to the rise time of the SAW generated by the IDT. Another parameter that is particularly relevant to fabrication is the design value of the width of each finger a. In a commonly used IDT, the width of the fingers and the gap are equal. In other words, for a double finger IDT the width of each finger is $\lambda/8$, for a split52 IDT the width of each finger is $\lambda/10$. Our IDTs are fabricated by electron beam lithography, and the drawing is typically more stable for higher dose. This results in the actual width of the fingers (on the order of several hundred nanometers) wider than that in the CAD design. To correct for this, we use the design value, which is the ideal finger width multiplied by a factor. As a result of the adjustment, the best value was obtained for each design. Values of 0.7 - 0.8 were used for most of the IDTs. Also, the width of the dense finger area, called the aperture w, was set to 30 µm for all IDTs. This value is selected to be sufficiently larger than the nanostructure used in our experiment and to give the real part of the IDT impedance closest to 50 Ω. (Optimization performed on an IDT with Ti/Au = 3 / 14 nm.)

2.3.2 Chirp IDT

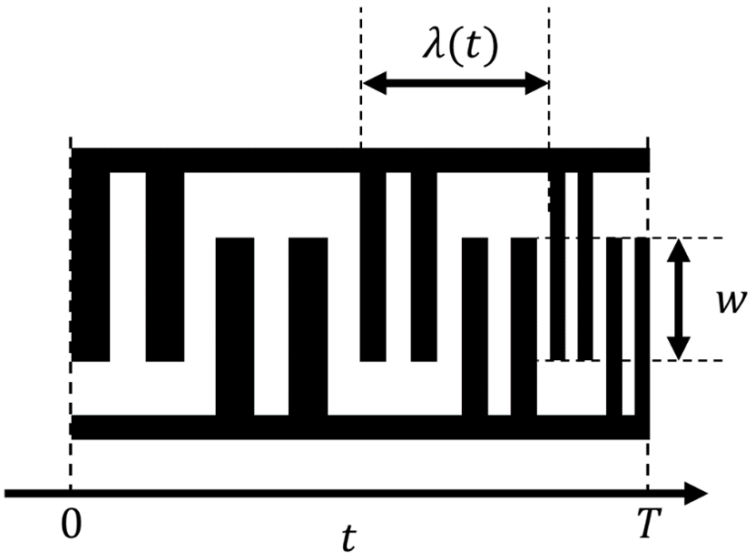

Figure 2.8: IDT design parameters of chirp finger IDT. The black regions are where metal is deposited.

SAW-driven single-electron transport has an intrinsic limitation related to the large spatial extent of the SAW train. The quantum state of the flying electron can be disturbed by SAW modulation during the dwell time in the stationary QDs [BHT+16]. Because of the presence of many potential minima accompanying the SAW (typically hundreds), it is furthermore difficult to transport the flying electron with accurate timing. To overcome the latter problem, a triggered SAW-driven sending process has been developed [TEL+19]. Requiring one radio-frequency line and one picosecond-voltage-pulse channel per QD, this method is fine for a few electron sources, but is difficult for further scalability. In addition, the triggering technique introduces unwanted electromagnetic crosstalk and potential charge excitation. Alternatively, replacing the periodic SAW train with a single-cycle acoustic pulse would deliver an elegant sending approach that brings less perturbation and naturally enables synchronized transport from a basically unlim-

ited number of sources. We employ Chirp IDT to generate a single strongly compressed acoustic pulse on demand.

In Chirp IDT, there are an additional parameter regarding the change in λ. In this study, the parameters are the minimum and maximum frequencies, f_{min} and f_{max}, and a function $f(t)$ that represents the frequency at each position $t(0 \sim T)$. In the design, the wavelength of the finger at each position is the corresponding $\lambda(t)$ obtained by $\lambda(t) = v_{\mathrm{SAW}}/f(t)$. Also, our chirp IDT has a finger pair for one period for each frequency. (see Fig. 2.8) We used two types of $f(t)$. The first is expressed by the following equation

$$f(t) = f_{\mathrm{min}} + \frac{f_{\mathrm{max}} - f_{\mathrm{min}}}{T} t \tag{2.1}$$

It varies linearly from the minimum frequency to the maximum frequency. We call this type “linear chirp IDT”. The second is a bit more complicated, with an exponential frequency change. The equation is as follows.

$$f(t) = Be^{\frac{t}{\tau}} + C \tag{2.2}$$

where B,τ and C are constants that are fitted from f_n obtained by dividing the area between f_{min} and f_{max} into n equal parts and t_n obtained by adding up the reciprocals of each element of f_n in turn satisfying the condition that the sum of t_n is almost equal to T. We call this type “exponential chirp IDT”. Fig. 2.9 shows the proportion of finger pairs that excite each frequency component in these chirp IDTs.

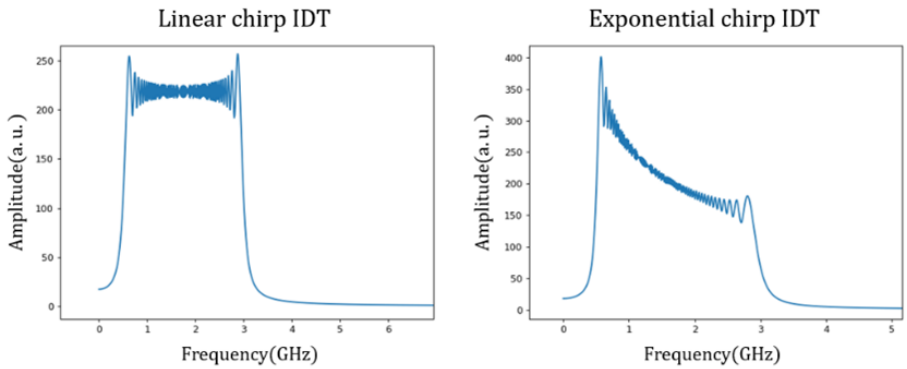

Figure 2.9: The proportion of finger pairs that excite each frequency component in linear and exponential chirp IDT.

2.4 Nanofabrication

The GaAs semi-insulating substrate is used. As will be discussed later, doped substrates are not suitable for SAW generation. We used GaAs semi-insulating substrates from DOWA and WaferTech. (see Table 2.1) The WaferTech substrate is the same as the one used for the substrate of the High Electron Mobility Transistor (HEMT) device. Although there is a difference in etch pit density (EPD) between these substrates due to the difference in crystal growth methods, it does not significantly affect the SAW properties.

Table 2.1: Information of GaAs wafers used in this study.

Maker	DOWA	WaferTech
Type	Semi-insulating	Semi-insulating
Resistivity	$\geq 10 \times 10^7 \Omega$cm	$\geq 10 \times 10^7 \Omega$cm
Crystal growth method	LEC	VGF
EPD	$\leq 2000\,\mathrm{cm}^{-2}$	$\leq 10 \times 10^5\,\mathrm{cm}^{-2}$

In GaAs, the $[1\bar{1}0]$ crystal directions are piezoelectric. All IDTs are fabricated to generate SAWs in the crystal direction of the piezoelectric material. As already mentioned, SAWs are generated by applying an AC voltage to an IDT, and their frequency is determined by the periodicity λ of the finger structure of the IDT and the velocity of the SAWs.

Considering the velocity of SAWs in GaAs, λ needs to be less than a micrometer in order to generate SAWs of several GHz. Furthermore, the width of each finger is $\sim \lambda/8$ in the case of double finger IDTs, which can be less than a hundred nanometers. To fabricate such a structure, we used electron beam lithography systems (Elionix ELS-7500a, Elionix ELS-BODEN, NanoBeam nB5). The IDTs were fabricated with Elionix ELS-7500a in Chapter 3, NanoBeam nB5 in Chapters 3, 4 and 5, and Elionix ELS-BODEN in Chapter 6.

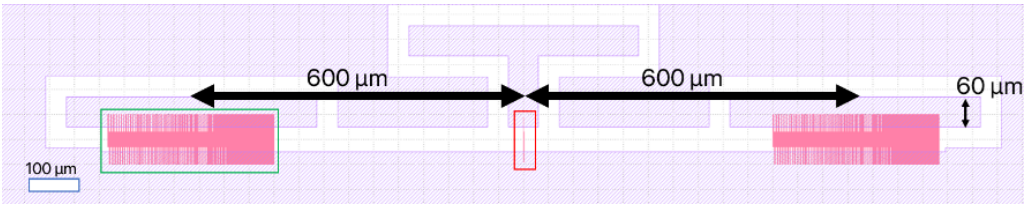

Figure 2.10: The design of a typical device with three IDTs used in this study for characterization of IDT. The shaded area is the metal, and the red dense structure is the IDT (Chirp IDT in this figure). The big metal pattern acts as a common ground pad, while the floating islands of metal are the pads for applying RF and measuring signals.

Table 2.2: Fabrication procedure of IDT in this study.

Step	Method	Description
1	Ultrasound cleaning	10 min in acetone (37 kHz, power50 %) + 10 min in IPA
2	Spin coat	PMMA 950 2 %, 4000 rpm, 60 s + 5 min @ 180 °C
3	Spin coat (2nd)	PMMA 950 2 %, 4000 rpm, 60 s + 5 min @ 180 °C
4	Lithography	Electron beam exposition
5	Development	30 s MIBK: IPA = 1: 3 + 30 s IPA
6	Sulfuric acid treatment	40 s H_2SO_4: DIH_2O = 1: 10 + 3 min DIH_2O
7	Metal deposition	Ti 3 nm @0.01 nm/s + Al or Au 27 nm @0.03 nm/s
8	Lift-off	At least 2 h in NMP @70 °C
9	Ultrasound	20 s in NMP (80 kHz, power 30 %)
10	Spin coat	AZ5214E, 3000 rpm, 30 s + 5 min @115 °C
11	Lithography	Maskless UV exposition
12	Development	3 min NMD3 (Shake sample with hands) + 1 min DI H_2O
13	Metal deposition	Ti20 nm @0.1 nm/s + Au100 nm @0.3 nm/s
14	Lift-off	At least 1 h in acetone
15	Ultrasound	1 min in acetone (80 kHz, power 30 %)

We use PMMA 950 as the EB resist, and coat it on the GaAs substrate with a thickness

of about 120 nm using a spin coater. If PMMA 950 2 % is used, adjust thickness by applying two spin coats. Also, by using PMMA 950 diluted with anisole and adjusting the concentration to 3 %, a thickness of 120 nm can be achieved by spin coating at 4000 rpm. After drawing, the exposed area is removed with the developer solution MIBK: IPA = 1: 3 and the surface is further treated with sulfuric acid (diluted 10 times with DI H_2O). The sulfuric acid treatment is used to remove the remaining resist and oxide film on the GaAs surface. After pattern formation, metal deposition is performed using an electron beam at ultra-high vacuum ($\sim 1 \times 10^{-7}$ Pa). We use the metal deposition equipment handmaded by National Institute of Advanced Industrial Science and Technology (AIST). It is capable of depositing Ti, Au, and Al with a resolution of subnanometer. Ti/Au 3/27 nm or Ti/Al = 3/27 nm is deposited. After that, the lift-off process is carried out to remove the metal by dissolving the resist with NMP (70 °C) to create a metal pattern, IDT. Previously, IDTs used in single electron transport devices were made of gold. This is because IDTs were fabricated at the same time as gate electrodes for forming QDs, etc., which are made of gold for the purpose to avoid complicated fabrication processes. However, in terms of generating SAWs using elastic effects, it is recommended to use lighter metals such as Al for IDTs. In this study, we fabricated IDTs made of aluminum. We also fabricated them in Au and compared the transfer characteristics of IDTs. The metal pads as shown in Fig. 2.10 for the measurements are fabricated by maskless UV exposure patterning (using equipment from Nano system solutions, Inc.) and vacuum deposition (using equipment from Eiko engineering, Inc.). AZ5214E is used as the photoresist, and it is coated on the GaAs substrate on which IDTs are fabricated by spin coating to a thickness of 1.62 µm. After developing, Ti/Au =20/100 nm is deposited. One point to note here is that when Al

is used as a material for IDT, it is recommended to use a developer solution adjusted to minimize the attack on Al (e.g. AZ developer for Merck Electronics, Inc.). Fig. 2.11 and 2.12 show optical microscopy (OM) and scanning electron microscopy (SEM) images of the fabricated double-finger and chirp IDTs, respectively. the uniformity of the metal electrodes over 100 µm reflects a well controlled nanofabrication process.

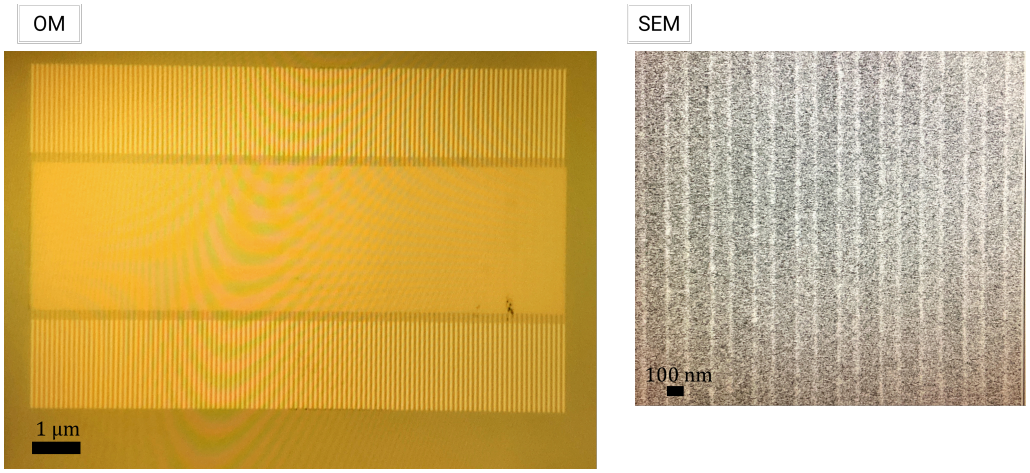

Figure 2.11: Optical microscope (OM) image and scanning electron microscope (SEM) image of the fabricated double finger IDT.

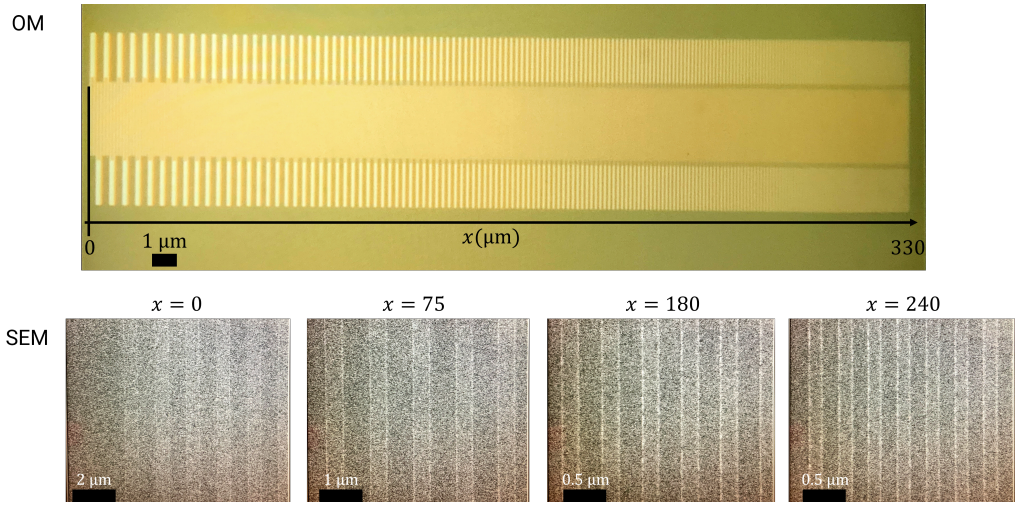

Figure 2.12: Optical microscope (OM) image and scanning electron microscope (SEM) image of the fabricated exponential chirp IDT.

2.5 Transmission characteristic of IDT

We discuss the evaluation of the transmission characteristics of IDT at room temperature. After describing the measurement setup and the method for observing SAW, the results and discussions are described. In particular, the influence of the material of the IDT on its properties will be investigated.

2.5.1 Measurement setup

We measured the transmission characteristics between two IDTs with a vector network analyzer. From the results, the frequency response and attenuation of the IDT can be obtained. Note that the transmission characteristics shown here are through two IDTs, and the actual characteristics of the IDT alone will be half of that. (In the case of the left and right IDTs having the same structure.) A VNA Keysight E5080A 9 kHz$\sim$9 GHz was used for this measurement. The contact to the device is performed by Cascade Microtech Elite300, which is a semi-automatic probe system with Picoprobe with GSG (Ground-Signal-Ground) configuration. This probe system is capable of contacting the sample at constant pressure. Ports 1 and 2 of the VNA are connected to two IDTs 1200 µm apart via the probes.

2.5.2 Fast Fourier transform filter

Since the results obtained directly by the VNA have a component of electromagnetic waves other than the SAW component, it is necessary to separate these components. Since the velocity of SAW ($\approx 3\,\mu\mathrm{m/ns}$) is much slower than that of electromagnetic waves

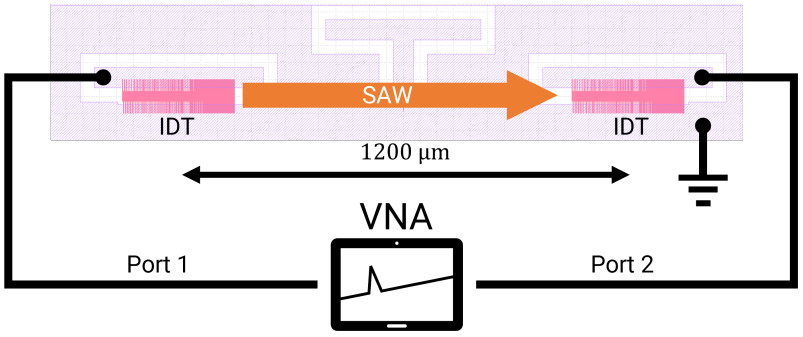

Figure 2.13: Measurement setup for transmission characteristic of IDT.

($3 \times 10^8\,\mathrm{m/s}$), when the measurement results obtained on the frequency axis are converted to data on the time axis by Fourier transform, each component can be clearly identified. Fig. 2.14 shows the case of the chirp IDT with a frequency band of 0.5 to 3.0 GHz as an example. Fig. 2.14a shows the raw data obtained by VNA, where the SAW signal is buried in the electromagnetic component. Fig. 2.14b shows the Fourier transform of this data. The electromagnetic wave component is strong around 0 s, and the SAW component appears after 360 ns. This value is appropriate because the distance between the IDTs is 1200 µm and the SAW velocity is $\approx 3\,\mu\mathrm{m/ns}$. By extracting only the SAW component surrounded by the yellow square in Fig. 2.14b and performing the inverse Fourier transform, the transmission characteristics of SAW can be obtained as shown in Fig. 2.14c. This filtering is applied to all VNA results in this paper using fast Fourier transform (FFT).

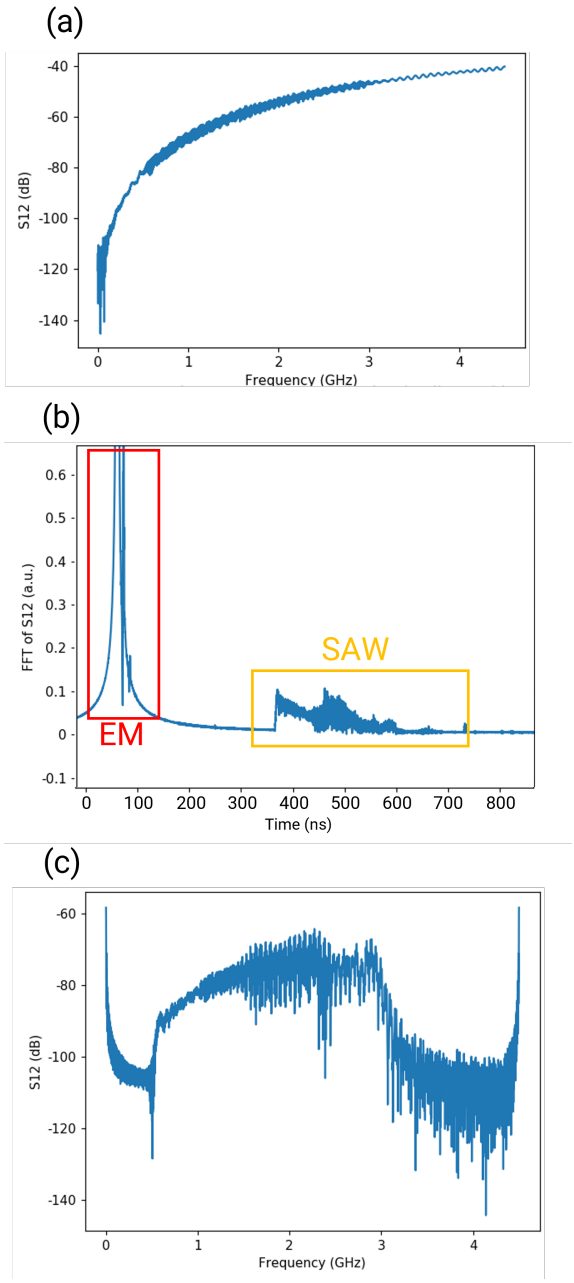

Figure 2.14: The method of extracting the components of surface acoustic wave using Fourier transform with the example of measuring the transmission characteristics of chirp IDT with the frequency band of 0.5 $\sim$ 3.0 GHz. **(a)** Raw data of frequency response of IDT by VNA. **(b)** Fourier transform data of (a) expressed in time axis. There is a component of electromagnetic wave (red square) at almost 0 s and a signal of surface acoustic wave (orange square) at the time corresponding to the distance between IDTs and the velocity of surface acoustic wave. **(c)** Frequency response of the surface acoustic wave generated by the IDT, obtained by extracting only the component of the surface acoustic wave in (b) and performing the inverse Fourier transform.

2.5.3 Double finger IDT

Conventional IDTs used for electron transport devices in GaAs are made of gold. This has the advantage of reducing the difficulty of the fabrication process because IDTs can be fabricated at the same time as fine structures such as gate electrodes for forming QDs. However, to maximize the use of elastic effects to generate SAWs, it is desirable to use a lighter metal such as aluminum for the IDTs. Fig. 2.15 shows the transmission

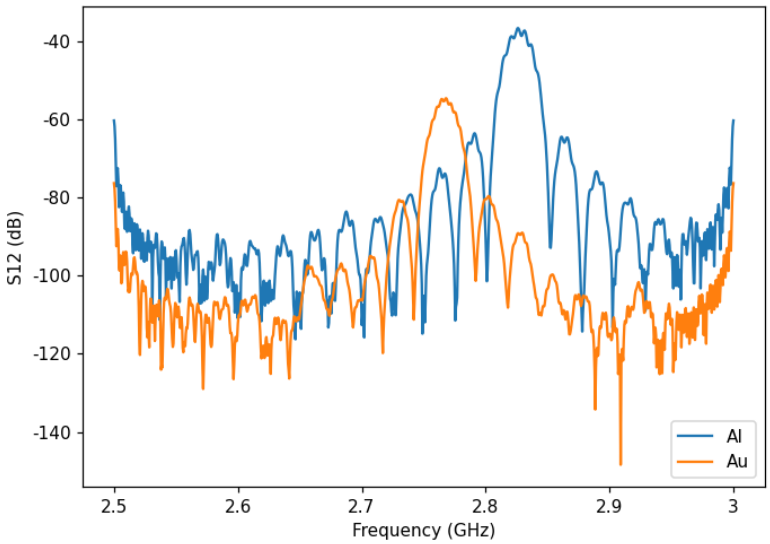

Figure 2.15: Transmission characteristics of double finger IDTs made of gold and aluminum.

characteristics of a double finger IDT ($\lambda = 1.0\,\mu\mathrm{m}$) made of gold and the same IDT made of aluminum. Both have the same λ, but the frequency of the excited SAW is different. There is a peak SAW signal at 2.81 GHz for aluminum and 2.77 GHz for gold. The SAW power also differs by about 20 dB depending on the metal of the IDT. This is caused by the difference in weight of the metal dumping on the GaAs surface. Aluminum has a density of $2.7\,\mathrm{g/cm^3}$, while gold has a density of $19.3\,\mathrm{g/cm^3}$. Gold is about seven times heavier than aluminum. Since SAW is a sound wave that travels along the surface of a material, if there is a heavy metal on the surface, the waves will be damped. As a result,

its velocity also decreases under metals. From $v_{\mathrm{SAW}} = f\lambda$, the average SAW velocity is obtained to be about 2.81 µm/ns for aluminum IDT and about 2.77 µm/ns for gold IDT.

2.5.4 Split52 IDT

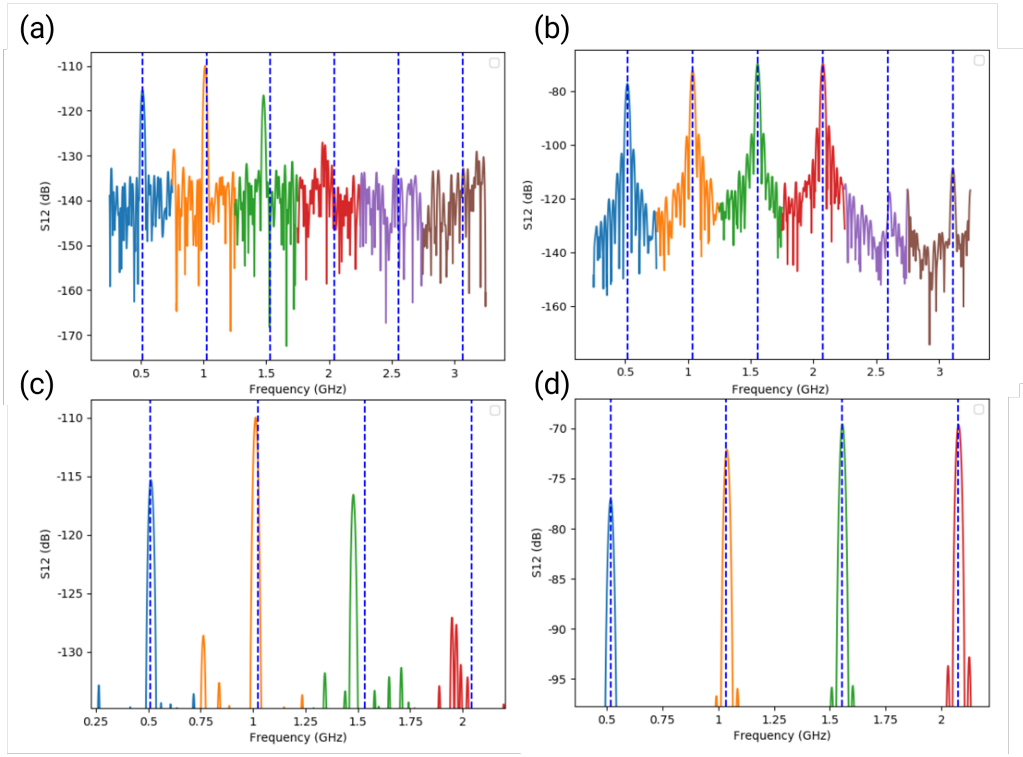

Figure 2.16: Transmission characteristics of split52 IDT with $\lambda = 5.5\,\mu\mathrm{m}$. The blue dotted lines represent each f_1 and its integer multiple frequency. (a), (c)made of gold. (b), (d) made of aluminum.

As mentioned in Chapter 2, the split52 IDT outputs a SAW with a fundamental frequency f_1 determined by the period λ of the IDT, and also a SAW with harmonics $f_n = nf_1(n = 2,3,4,6)$. In a previous study, split52 IDT with $f_1 = 144\,\mathrm{MHz}$ was fabricated to generate SAW up to the 6th harmonic (864 MHz) [SZA+15]. we fabricated split52 IDTs of $\lambda = 5.5\,\mu\mathrm{m}$ made of gold and aluminum. Then we measured transmission characteristics. Fig. 2.16a shows the frequency response of split52 IDT made of gold, showing the frequency shift that is also seen in the double finger IDT. In particular, the

higher the harmonics, the larger the frequency shift, and the frequency of the 4th harmonic shifts from $4f_1$ to about 60 MHz to the lower frequency side. On the other hand, split52 IDT made of aluminum, as shown in Fig. 2.16b, has all harmonics matching nf_1. The frequency changes to $f_1 = 5.2$ GHz due to the change in SAW velocity. Also, if you look at the values on the vertical axis of (a) and (b) (or (c) and (d)) in Fig. 2.16, you can see that by changing the IDT metal from gold to aluminum, the transmission characteristics improved by about 30 dB at each frequency (especially the 4th harmonic improved by 60 dB).

2.5.5 Chirp IDT

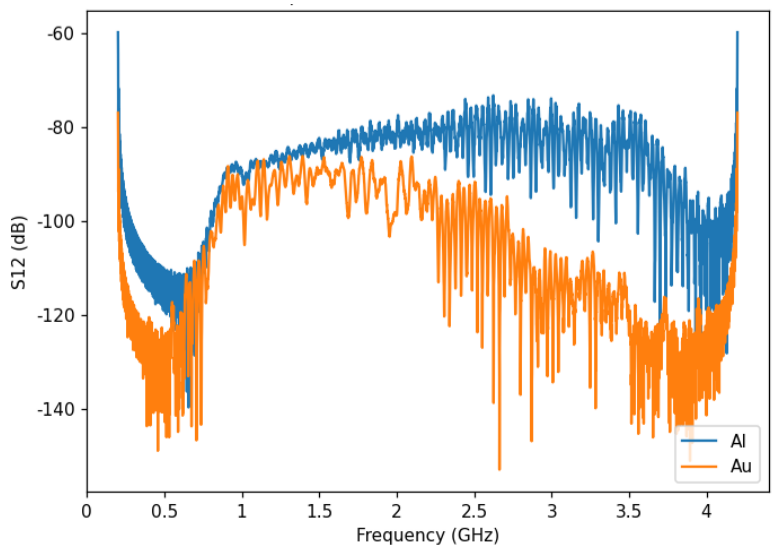

Figure 2.17: Transmission characteristics of exponential chirp IDT with $f_{\min} = 0.77$ GHz,$f_{\max} = 3.77$ GHz,and $T = 40$ ns made of gold and aluminum.

Transmission characteristics of exponential chirp IDT made of gold and aluminum with $f_{\min} = 0.77$ GHz, $f_{\max} = 3.77$ GHz and $T = 40$ ns are shown in Fig. 2.17. In the frequency range above 2 GHz, the strength of the SAW generated by the IDT made of gold tends to attenuate, while the strength of the SAW generated by the IDT made of

aluminum remains constant up to $f_{\max}$.

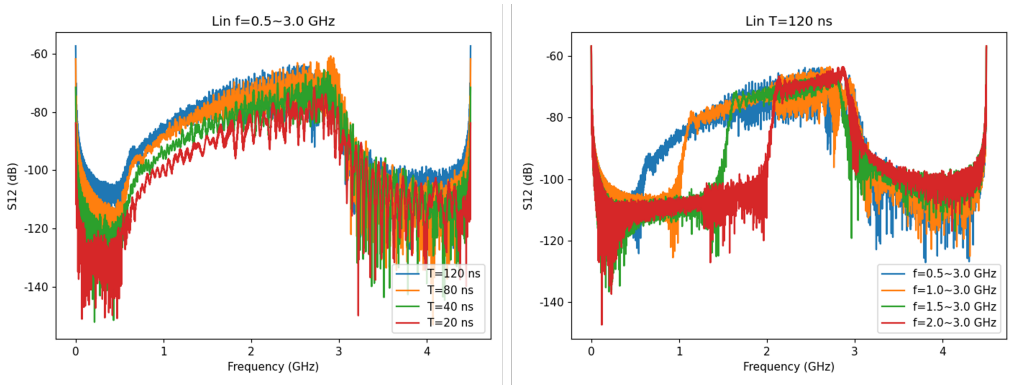

Figure 2.18: Transmission characteristics of linear chirp IDT with $f_{\max}$ fixed at 3 GHz and $f_{\min} = 0.5, 1.0, 1.5$,and 2.0 GHz, and $T = 20, 40, 80$,and 120 ns. Material of IDT is aluminum.

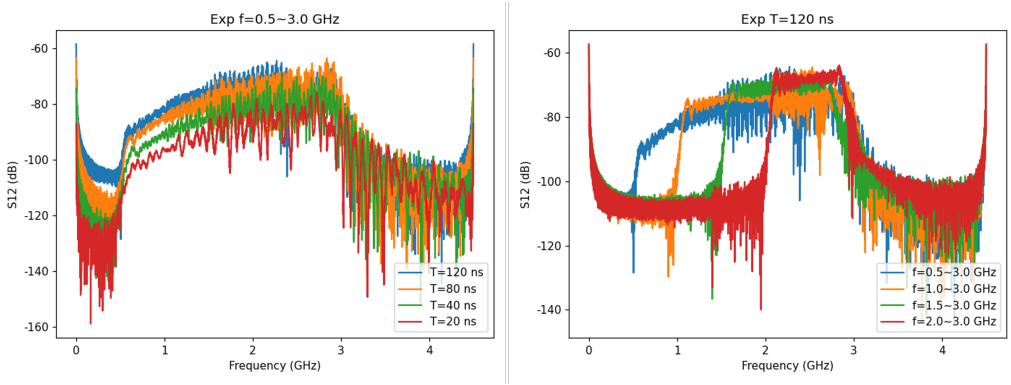

Figure 2.19: Transmission characteristics of exponential chirp IDT with $f_{\max}$ fixed at 3 GHz and $f_{\min} = 0.5, 1.0, 1.5$,and 2.0 GHz, and $T = 20, 40, 80$,and 120 ns. Material of IDT is aluminum.

Next, linear and exponential chirp IDTs with $f_{\max}$ fixed at 3 GHz and $f_{\min}$ and T varied were prepared and measured. The $f_{\min}$ is $0.5, 1.0, 1.5$,and 2.0 GHz, and T is $20, 40, 80$,and 120 ns. All IDT is made of aluminum. The results of each measurement are shown in Fig. 2.18 and 2.19. Comparison of linear and exponential chirp IDT in each condition shown in Fig. 2.20 shows that exponential chirp IDT has less difference in strength in each frequency band compared to linear chirp IDT.

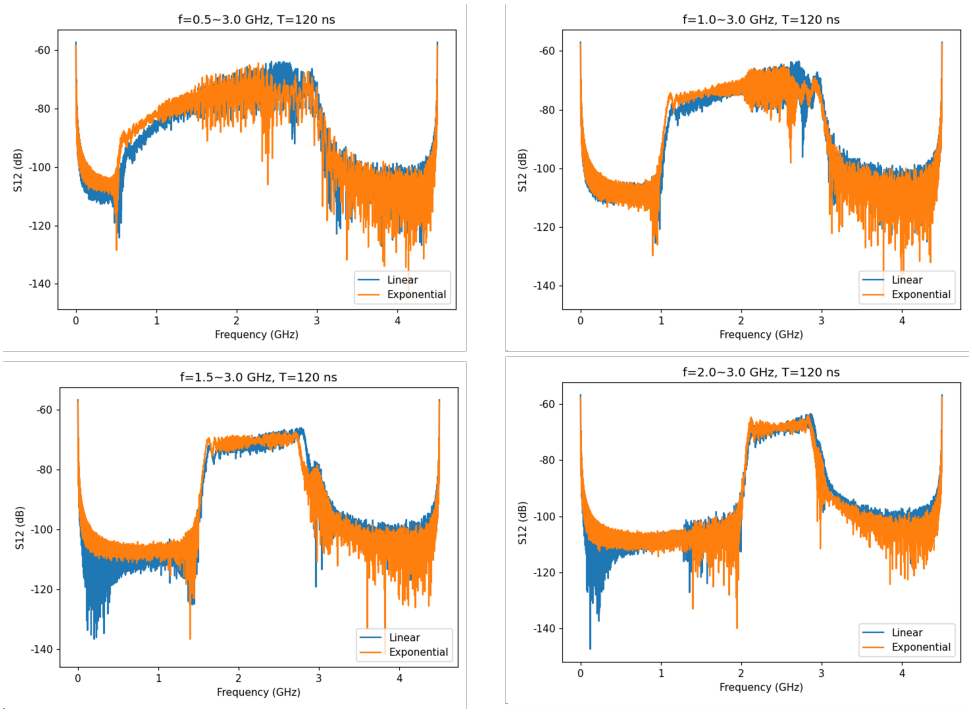

Figure 2.20: Comparison of transmission characteristics between linear and exponential chirp IDT with $f_{\max}$ fixed at 3 GHz and $f_{\min} = 0.5, 1.0, 1.5$,and 2.0 GHz, $T = 120$ ns. Material of IDT is aluminum.

2.6 Time-resolved measurement of IDT

We investigated the shape of SAWs generated by double finger IDTs, split52 IDTs and chirp IDTs by time-resolved measurements. In particular, we focus on the effect of the input voltage parameter. Our purpose is to generate SAWs with shapes other than sine waves and especially single minimum SAWs. We show experimentally that this is possible by superposing waves of different frequencies using chirp IDT. Single minimum SAWs can only be achieved with pulses that excite all frequencies at the right timing and strength.

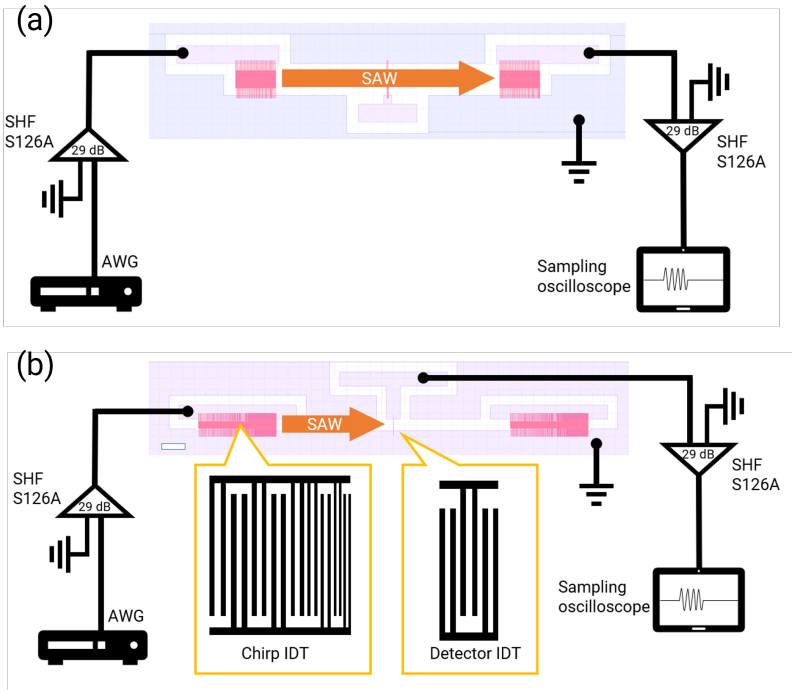

Figure 2.21: Measurement setup for time-resolved measurement of IDT.

2.6.1 Measurement setup

A shape of the SAW is measured by time-resolved measurement. Fig. 2.21a shows a measurement setup using a same IDT design on left and right. Split52 IDT was measured with this setup. Fig. 2.21b shows a setup using a broadband IDT as a detector, and double finger IDT and chirp IDT was measured with this setup. A nanosecond voltage pulse is used to excite one IDT. The generated SAW propagates to the other IDT at a distance of several hundred micrometers, and the voltage generated between the fingers of the IDT when the SAW arrives is measured by a sampling oscilloscope. A voltage input to an IDT is generated by an arbitrary waveform generator (AWG). Keysight M8195A is employed. Its sampling rate is set to be 64 GS/s, so the shortest pulse is about 15 ps (full width at half maximum). The peak-to-peak maximum value of the AWG output voltage is limited to 1 V. We used an amplifier with a gain of 29 dB (SHF S126S) to input a voltage

amplitude of 2.2 V to an IDT. Oscilloscopes used are Keysight 86100C for setup (a) and Keysight N1094A for setup (b). Pattern-lock mode is used and average is 1000 times.

2.6.2 Broadband detection

Due to the reverse piezoelectric phenomenon, an electrical signal is generated and can be captured by a high-speed oscilloscope when a SAW crosses an other IDT. For the IDT that functions as a detector to exhibit optimal performance, it must be engineered to align with the anticipated bandwidth of the incoming signal. Typically, the frequency behavior of a conventional IDT comprising N elements with a resonance frequency of f_0 is closely represented by a sinc function [Mor07]:

$$H(f) \propto \frac{\sin \pi N(f - f_0)/f_0}{\pi N(f - f_0)/f_0} \tag{2.3}$$

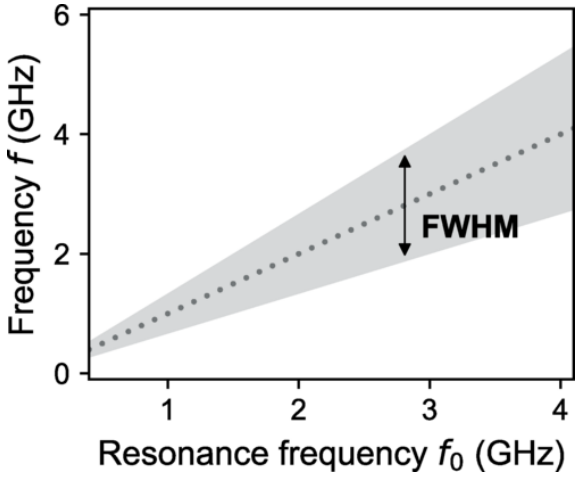

Figure 2.22: Detection bandwidth. Pass band of a regular IDT with $N = 1.5$. The shaded area indicates the FWHM of the transmission peak. The vertical double-headed arrow indicates the employed resonance frequency of the detector IDT, $f_0 \approx 2.81$ GHz.

Subsequently, one can calculate the full width at half maximum (FWHM) to be f_0/N. Considering the broad bandwidth of the chirped pulse, we reduce the count of detector

electrodes to a singular one, resulting in $N = 1.5$ when considering a set of adjacent grounded fingers. Displayed in Fig. 2.22 is the frequency passband corresponding to this arrangement as a function of f_0. To ensure accurate detection of the SAW, especially at frequencies up to 3 GHz, we have selected an IDT periodicity of $\lambda_0 = 1\,\mu\text{m} (f_0 \approx 2.81\,\text{GHz})$.

2.6.3 Double finger IDT

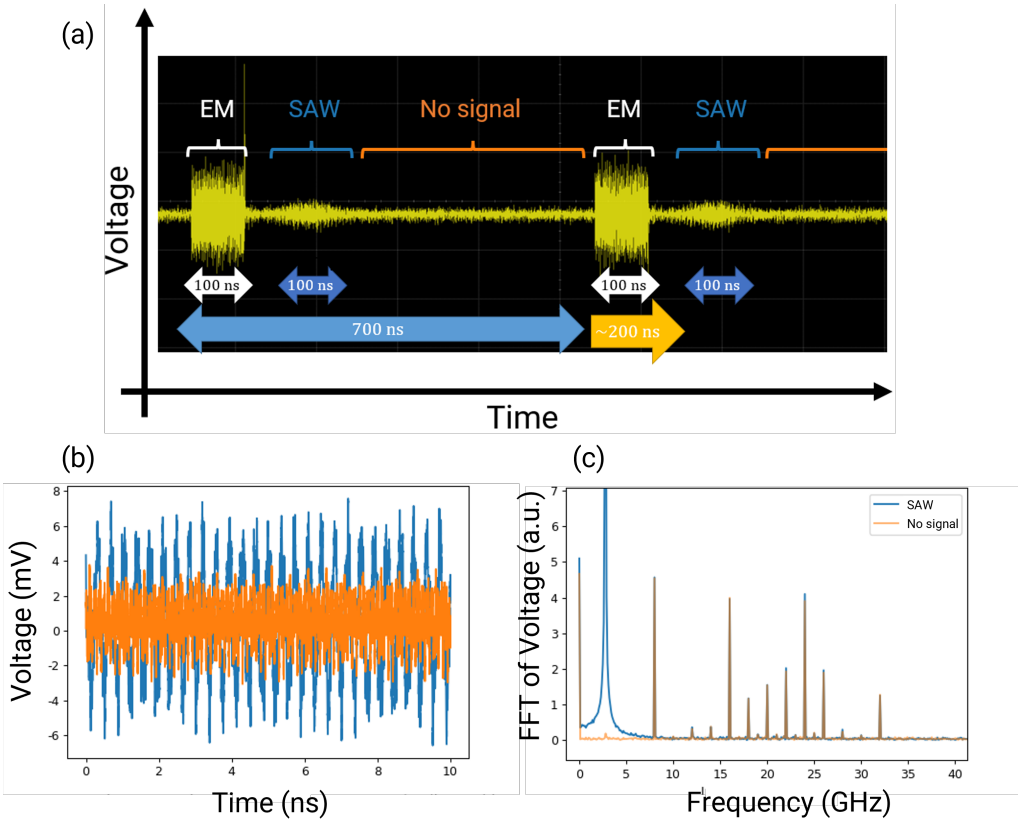

Figure 2.23: **(a)** Time scale and position of each signal. **(b)** The blue line is the surface acoustic wave signal part of (a), and the orange line is the No signal part of (a), measured by the oscilloscope. **(c)** The Fourier transform of the respective result in (b).

In time-resolved measurements, signals from an IDT can be observed on the nanosecond scale, so it is easy to distinguish between the electromagnetic wave component and the SAW component. Fig. 2.23a shows the signal observed at a detector IDT when a

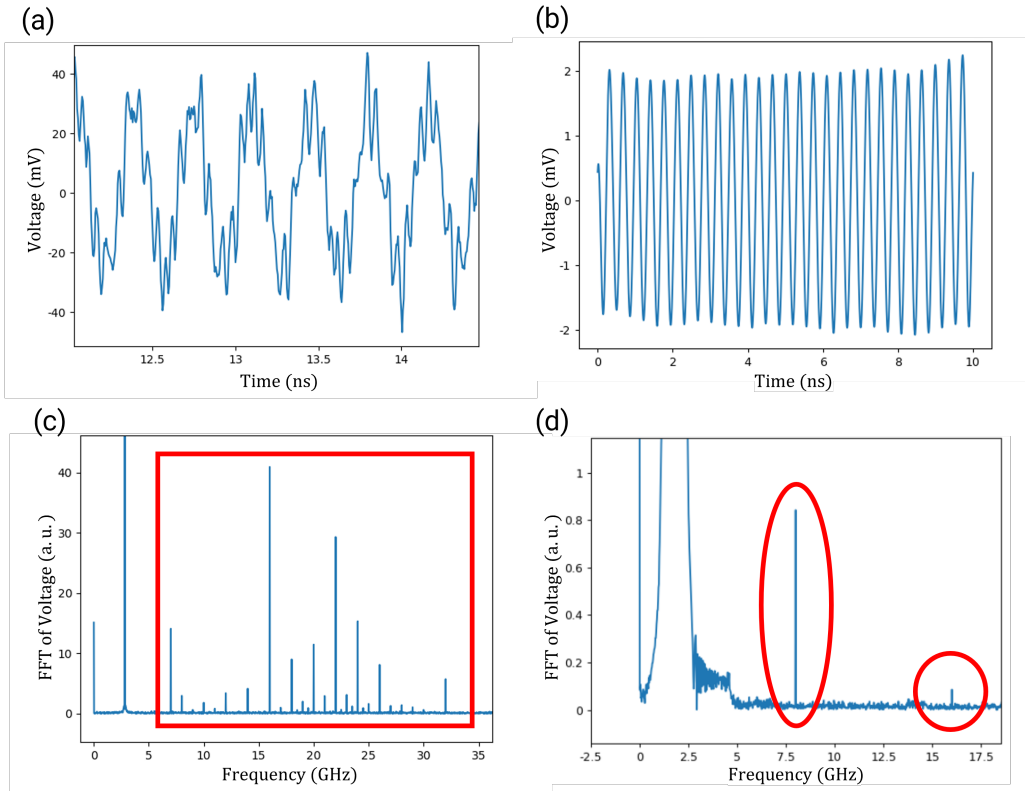

Figure 2.24: **(a)** Raw data of the time-resolved measurement including the component of surface acoustic waves generated by the double-finger IDT with $\lambda = 1.0\,\mu\text{m}$. **(b)** The result after filtering out the signal other than the surface acoustic wave from the data in (a). **(c)** Fourier transform of the data in (a). There is a signal at surface acoustic wave frequency (2.81 GHz) and high frequency noise (red squares). **(d)** Same type of data as (c) but measured with an attenuator instead of an IDT. The attenuator is chosen to have same attenuation as the IDT at 2.81 GHz ($-70\,\text{dB}$), and there is similar high frequency noise (red circles) as with the IDT.

2.81 GHz sine wave is input to the double finger IDT with $\lambda = 1.0\,\mu\text{m}$ and $T = 40\,\text{ns}$. Since the distance between the IDT that excites SAW and the detector IDT is 600 µm, there is a delay of $600(\mu\text{m})/2.81(\mu\text{m/ns}) \approx 210(\text{ns})$ between the time SAW is excited and the time it is detected. Therefore, the input was set to a 700 ns repetitive signal with a duty ratio of $1/7$ (Sine wave is 100 ns) in order to clearly distinguish between an electromagnetic wave component and a SAW component. Fig. 2.24a shows the observed SAW signal. A signal with a period of about 350 ps corresponding to the SAW frequency of 2.81 GHz is observed, but the noise is large. As shown in Fig. 2.24c, the Fourier transform of the measurement result shows that there are several components with high frequencies.

To confirm that these components are not components of SAW, we performed two measurements. First, the IDT part was replaced with an attenuator and the same measurement was performed. The level of attenuation was set to $-70\,\mathrm{dB}$, which is equivalent to the attenuation of the IDT at 2.81 GHz. The results are shown in Fig. 2.24d, the components at higher frequencies such as 8 GHz and 16 GHz were visible, although they were attenuated compared to the case with the IDT. Next, we compared the signal of SAW with the signal of the area where neither EM nor SAW components exist as shown in Fig. 2.23b, c. Comparing the results of the Fourier transform, it was confirmed that all the high frequency components except for the SAW exist also for the no signal part. By subtracting the noise data obtained here from the noisy SAW results, we can observe a clear SAW signal as shown in Fig. 2.24b. From these two measurements, it is clear that the high frequency noise exists even without IDT and without SAW. In other words, this noise is not caused by the IDT or SAW. Also, since these noises are attenuated when the attenuator is used instead of the IDT in the measurement, it was confirmed that these high frequency components are not through the IDT. The results of time-resolved measurements after this section are filtered to suppress components other than SAW.

2.6.4 Split52 IDT

split52 IDT is able to generate SAWs of multiple frequencies. This allows us to achieve additive Fourier synthesis as defined in equation 2.4, 2.5. In order to generate the desired waveform, it is necessary to superimpose the components of each frequency with ideal strength and phase. In this context, ”ideal” means that the characteristics of each frequency component of the surface acoustic are actually generated matches the tar-

get waveform.

$$A_{\text{sawtooth}}(t) = \sum_{n=1,2,3,\ldots} n^{-1} \sin 2\pi n f_1 t \tag{2.4}$$

$$A_{\delta\text{pulse}}(t) = \sum_{n=1,2,3,\ldots} \cos 2\pi n f_1 t \tag{2.5}$$

To achieve this, it is necessary to take into account SAWs generation characteristics of the IDT. As can be seen from the transmission characteristics obtained from the VNA measurements, the strength of the SAW output from the IDT differs depending on the frequency. In the case of our IDT, Fig. 2.16b shows that there is a difference in SAW voltage amplitude of about 6 dB, twice on a voltage basis, between the fundamental frequency of 0.52 GHz and the 4th harmonic of 2.08 GHz.

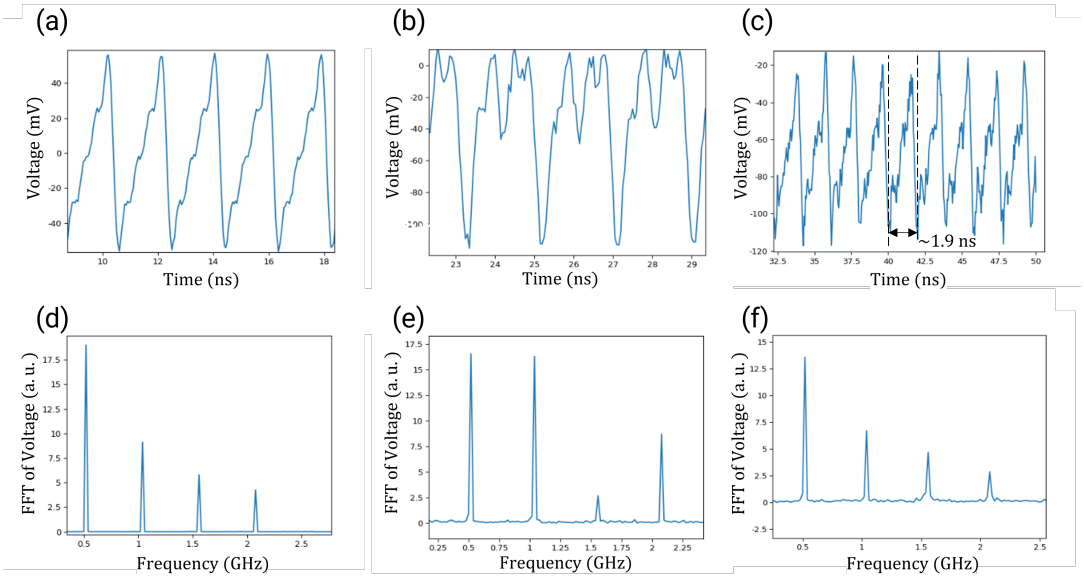

Figure 2.25: **(a)** Sawtooth waves generated by additive Fourier synthesis of frequency components at $f = 0.52, 1.04, 1.56$, and 2.08 GHz using AWG. **(b)** Surface acoustic wave generated by inputting the waveform of (a) into the split52 IDT. **(c)** Sawtooth SAW generated by the split52 IDT with the adjusted input signal. (d), (e), and (f) Fourier transforms of (a), (b), and (c), respectively.

In this experiment, we measured split52 IDT with $\lambda = 5.5\,\mu$m, $T = 40$ ns, and used four frequencies of SAWs, $f_1 = 0.52$ GHz, $f_2 = 1.04$ GHz, $f_3 = 1.56$ GHz, and $f_4 = 2.08$ GHz. The additive Fourier synthesis of these frequencies generates a sawtooth wave

and a delta pulse. A sawtooth wave signal consisting of the four frequency components, as shown in Fig. 2.25a, was generated by the AWG, input to the split52 IDT, and detected by the IDT of the same type about 900 µm away. As shown in Fig. 2.25b, the detected signal is not shaped like a sawtooth wave due to the difference in strength and phase of the SAW at each frequency generated from the IDT. The comparison between the Fourier transform of the detected signal (Fig. 2.25e) and the Fourier transform of the sawtooth wave of the input signal (Fig. 2.25d) shows that the strength of each frequency component is scattered. By extracting the relative relationship of strength and phase shift of SAWs at each frequency from the Fourier transform of the detected signal, and applying the correction to the signal input from the AWG to the IDT, a sawtooth SAW could be detected as shown in Fig. 2.25c. From its Fourier transform shown in Fig. 2.25f, we can see that the strength of SAW at each frequency is corrected.

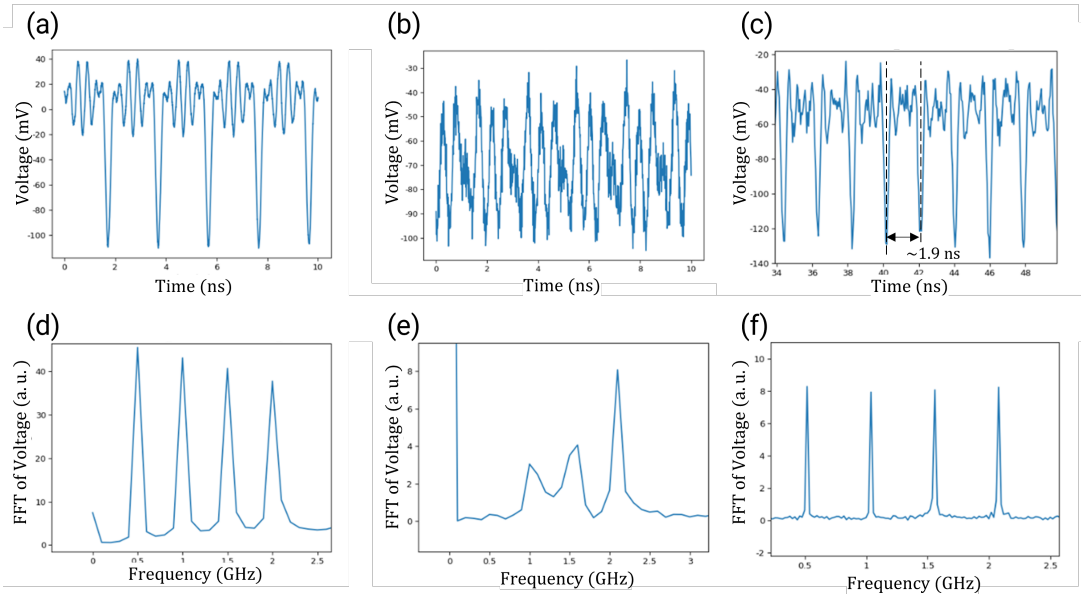

Figure 2.26: **(a)** δ pulse generated by additive Fourier synthesis of frequency components at $f = 0.52, 1.04, 1.56$, and 2.08 GHz using AWG. **(b)** Surface acoustic wave generated by inputting the waveform of (a) into the split52 IDT. **(c)** δ pulse generated by the split52 IDT with the adjusted input signal. (d), (e), and (f) Fourier transforms of (a), (b), and (c), respectively.

A same technique was used to generate a δ pulse. The period of the signal generated

by such an additive Fourier synthesis depends on the lowest frequency of the superposition frequency. Since the fundamental frequency, or lowest frequency, of the split52 IDT is 0.52 GHz, the period of the generated sawtooth wave and δ pulse is $1/0.52\,\mathrm{GHz} = 1.9\,\mathrm{ns}$ in this experiment. By synthesizing SAWs of multiple frequencies by additive Fourier synthesis in this way, SAWs with arbitrary shapes can be generated. Once such a shape is formed, the SAW propagates while maintaining its shape because it has linear dispersion.

2.6.5 Chirp IDT: pulsed SAW generation

We investigated linear chirp IDT and exponential chirp IDT. To avoid confusion in this section, values related to the design value of the IDT are indicated with the superscript IDT, while values related to the input signal generated by the AWG are indicated with the superscript s as necessary. In order to perfectly superimpose all frequencies to produce a single minimum SAW, it is necessary that all SAWs at each frequency are in phase. This means that we need to excite SAWs of each frequency at a proper timing. The physical parameters of the IDT are fixed after fabrication. Therefore, only the parameters related to the input signal to the chirp IDT can be adjusted. We need to excite each frequency SAWs continuously, so we use a chirp signal as the input signal, which changes its frequency as a function of time. In general, a chirp signal is defined as follows

$$y(t) = A \sin \phi(t) \tag{2.6}$$

, where A corresponds to the amplitude and $\phi(t)$ is the time-dependent phase. This phase can be obtained from the frequency $f(t)$, as the area underneath

$$\phi(t) = \phi_0 + 2\pi \int_0^t f(\tau) d\tau \tag{2.7}$$

, where ϕ_0 is the initial phase. $f(t)$ is given by equations 2.1 and 2.2 for linear chirp and exponential chirp, respectively. Thus, the phases are obtained as

$$\phi(t) = \phi_0 + \pi \frac{f_{\text{max}}^{\text{IDT}} - f_{\text{min}}^{\text{IDT}} f}{T^{\text{IDT}}} t^2 + 2\pi f_{\text{min}}^{\text{IDT}} t \tag{2.8}$$

and

$$\phi(t) = \phi_0 + 2\pi B\tau(\exp t/\tau - 1) + 2\pi Ct \tag{2.9}$$

, respectively. These chirp pulse sweeps continuously while the frequency of each finger pair in the designed IDT is discrete. This is not a problem for the IDT, because the frequency response is also continuous, as shown in Fig. 2.17. Since it is necessary to include more frequencies to get close to the ideal single minimum, or δ pulse, we used a chirp IDT with $f_{\text{min}} = 0.5\,\text{GHz}$ and $f_{\text{max}} = 3.0\,\text{GHz}$, which is the widest bandwidth among the IDTs we fabricated.

One of the most important parameters related to the input signal for the superposition of SAWs of all frequencies is T^{s}. The fabricated chirp IDT has a structure where the frequency increases from left to right. By inputting a signal that changes from low to high frequency, a compressed SAW of each frequency element is generated on the right side of the IDT. Therefore, it is ideal to excite the SAW at the right end of the IDT when the SAW generated at the left end of the IDT reaches the right end of the IDT.

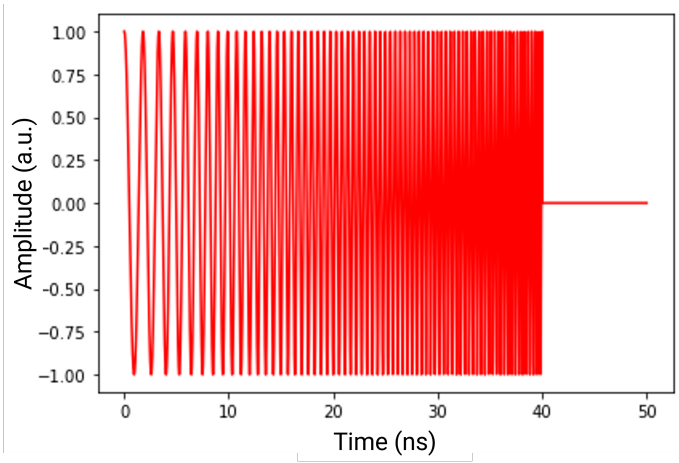

Figure 2.27: Example of a chirp pulse whose parameters are $f^s_{\mathrm{max}} = 3.0\,\mathrm{GHz}$, $f^s_{\mathrm{min}} = 0.77\,\mathrm{GHz}$ and $T^s = 40\,\mathrm{ns}$.

There is a parameter of IDT, T, which is the length of the IDT in time, and the IDT was designed with $v^{\mathrm{IDT}}_{\mathrm{SAW}} = 2.77\,\mu\mathrm{m/ns}$ in this experiment. However, this value is a commonly used velocity for GaAs under an IDT made of gold. We should note that $T^{\mathrm{IDT}} \neq T^{\mathrm{s}}$ for optimal compression in an IDT made of aluminum. When the SAW velocity changes, the frequency of the excited SAW, which corresponds to the period of the finger pair of the IDT, also changes. The velocity of SAW in GaAs with aluminum on top is about $2.81\,\mu\mathrm{m/ns}$. In other words, the IDT was designed to excite SAWs with frequencies between 0.5 and 3.0 GHz, but strictly it should be shifted by $\sim 100\,\mathrm{MHz}$. In this experiment, the input signal frequency was fixed at $f^{\mathrm{s}}_{\mathrm{min}} = 0.5\,\mathrm{GHz}$ and $f^{\mathrm{s}}_{\mathrm{max}} = 3.0\,\mathrm{GHz}$ because the deviation is small compared to the whole bandwidth of 2.5 GHz and the exact SAW velocity at each IDT needs to be derived, which is not a stable parameter. Fig. 2.28 shows compressed SAWs observed at a detector IDT when a chirp signal with different T^{s} is input to a linear chirp IDT with $T^{\mathrm{IDT}} = 120\,\mathrm{ns}$. At around $T^{\mathrm{s}} = 116\,\mathrm{ns}$, the SAW is at its most compressed state, which means that SAWs of all frequencies are superposed. At $T^{\mathrm{s}} = 120\,\mathrm{ns}$, the low frequency component reaches the detector IDT first.

This means that when high frequency SAWs are generated, the low frequency ones have already left the IDT. Conversely, at $T^{\mathrm{s}} = 112\,\mathrm{ns}$, the high frequency components reach the detector IDT first.

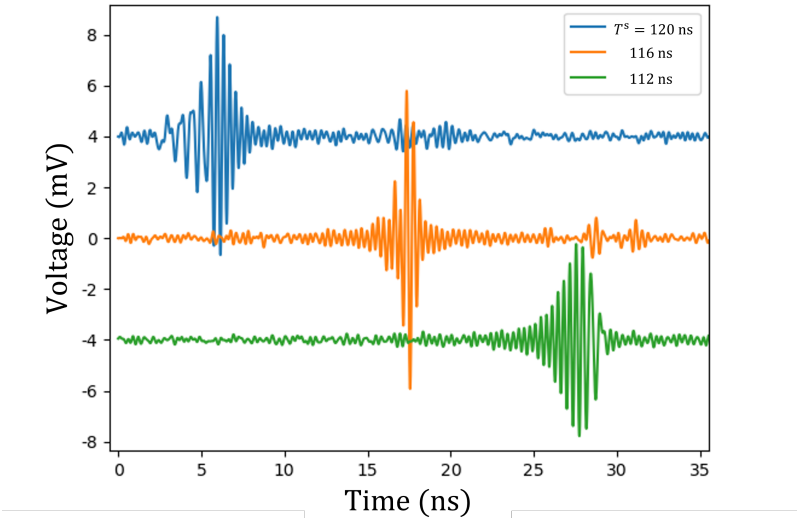

Figure 2.28: Compressed surface acoustic wave output from linear chirp IDT when varying the input signal length T^{s}.

Since a linear chirp IDT has a structure in which the frequency changes linearly, ideal excitation can be achieved by adjusting T^{s} even when the actual SAW velocity is different from the SAW velocity assumed in the design. However, since exponential chirp IDT has a structure in which the frequency changes exponentially, if the SAW velocity changes, the designed frequency and the ideal finger position do not match perfectly. To solve this problem, we corrected the fitting parameters used in generating the input signal. For chirp signal correction, we use the f_n^{IDT} of frequencies and the corresponding t_n^{IDT} of finger positions in time units which were used for fitting the function 2.2 during chirp IDT design, and the corrected SAW velocity $v^{\mathrm{s}}_{\mathrm{SAW(corrected)}}$. λ^{IDT} and finger position is consistent. First, f_n^{IDT} and t_n^{IDT} are corrected by the following equations, respectively.

$$f_n^{\mathrm{s}} = f_n^{\mathrm{IDT}} \times (v^{\mathrm{s}}_{\mathrm{SAW(corrected)}} / v^{\mathrm{IDT}}_{\mathrm{SAW}}) \tag{2.10}$$

$$t_n^{\mathrm{s}} = t_n^{\mathrm{IDT}} \times \left(v_{\mathrm{SAW}}^{\mathrm{IDT}} / v_{\mathrm{SAW(corrected)}}^{\mathrm{s}}\right) \tag{2.11}$$

Using the obtained f_n^{s} and t_n^{s}, we can now fit the function 2.2 to get the corrected fitting parameters B^{s},τ^{s},and C^{s}. The time-dependent phase obtained by replacing the fitting parameters in equation 2.9 with these corrected parameters is used to generate the corrected chirp signal.

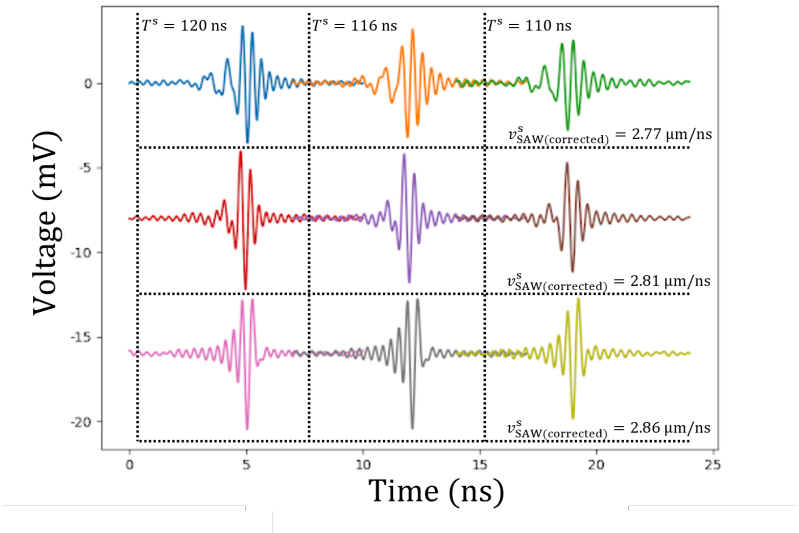

Figure 2.29: The change in the compressed surface acoustic waves generated by the exponential chirp by adjusting the length of the input signal $T^{\mathrm{s}} = 110, 116$ and $120\,\mathrm{ns}$ and correcting for the frequency chirp by the corrected velocity of the surface acoustic wave $v^{\mathrm{s}}_{\mathrm{SAW(corrected)}} = 2.77, 2.81$ and $2.86\,\mu\mathrm{m/ns}$. There is an offset of $-8, -16\,\mathrm{mV}$ in the y-axis direction.

Fig. 2.29 shows the change in the compressed SAW generated by the exponential chirp by adjusting the length of the input signal T^{s} and correcting for the frequency chirp by the corrected velocity of the $v^{\mathrm{s}}_{\mathrm{SAW(corrected)}}$. Comparing each row (constant $v^{\mathrm{s}}_{\mathrm{SAW(corrected)}}$), we can see that the change in T does not significantly affect the SAW superposition. In contrast, the comparison of each column (constant T^{s}) shows that the correction of frequency chirp is important for single minimum generation in exponential chirp. The middle row ($v^{\mathrm{s}}_{\mathrm{SAW(corrected)}} = 2.81\,\mu\mathrm{m/ns}$) has the highest compression ratio among

the three cases. We adjusted the parameters for linear chirp IDT and exponential chirp IDT at $T^{\mathrm{IDT}} = 20, 40, 80$,and 120 ns to find the condition with the highest maximum amplitude, that is, the optimum superposition of all SAWs. The single-minimum SAWs obtained under each optimum condition are shown in Fig. 2.30. Comparing linear chirp and exponential chirp, the maximum amplitude of exponential is about 1.5 times smaller than that of linear for the same T^{IDT}. However, the amplitude of the side with the strongest amplitude is smaller in the exponential chirp. As a result, the single minimum SAW generated by the exponential chirp is closer to the delta pulse than the one generated by the linear. This is an consistent result because the transmission characteristics obtained by the VNA show little difference in strength between each frequency. For single electron transport, we think that exponential chirp is better than linear one because it is less likely to cause unexpected transport at amplitudes other than the strongest.

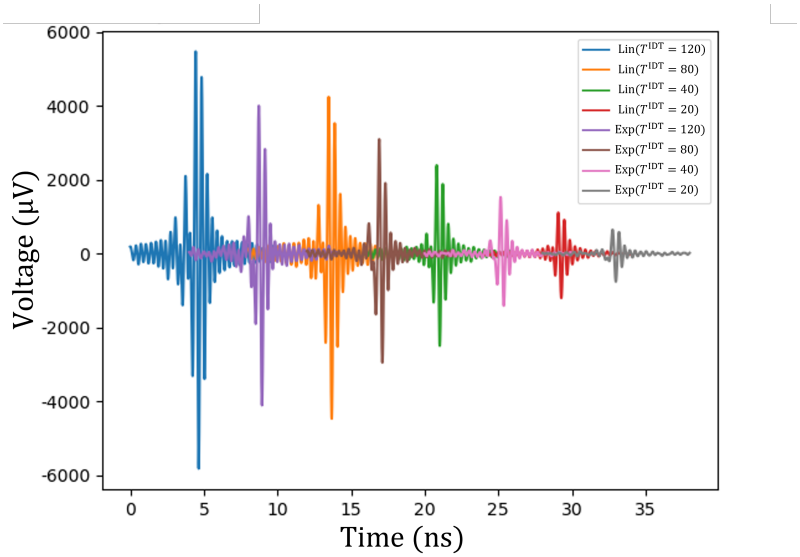

Figure 2.30: The optimal single-minimum surface acoustic waves obtained with linear chirp IDT and exponential chirp IDT as a result of parameter adjustment by T^{s} and $v^{\mathrm{s}}_{\mathrm{SAW(corrected)}}$. T^{IDT} indicates the length of the IDT, which is 20, 40, 80,and 120 ns.

Next, we evaluated the strength of the single-minimum SAW in electron transport devices. In Fig. 2.31, we compare the SAW generated by a double-fingered IDT made of

Au with $T^{\mathrm{IDT}} = 40\,\mathrm{ns}$, which has been conventionally used for single electron transport in GaAs, with a single-minimum SAW generated by an exponential chirp IDT made of aluminum with $T^{\mathrm{IDT}} = 120\,\mathrm{ns}$. The measurements were performed in the same measurement system and the power of the signal input to the IDT was also the same. Both have a peak-to-peak voltage amplitude of about $5\,\mathrm{mV}$. This means that the exponential chirp IDT made of aluminum with $T^{\mathrm{IDT}} = 120\,\mathrm{ns}$ can produce SAWs that are capable of single electron transport.

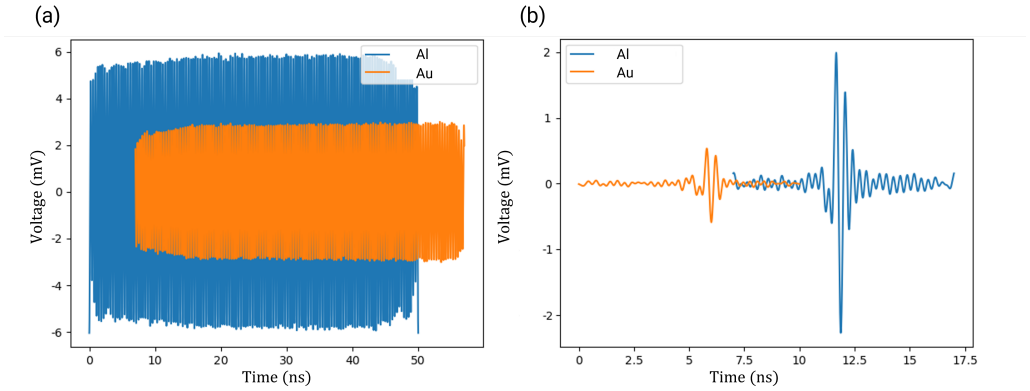

Figure 2.31: Surface acoustic waves generated by different types of IDTs measured in the same measurement system with the same power signal input. The blue line indicates the result of an IDT made of aluminum and the orange line indicates the result of an IDT made of gold. (a) SAWs generated consistently by a double finger IDT with $T^{\mathrm{IDT}} = 40\,\mathrm{ns}$. (b) Single minimal SAW generated by the exponential chirp IDT with $T^{\mathrm{IDT}} = 120\,\mathrm{ns}$.

2.7 Conclusion

In this section, we describe the design and fabrication of IDTs and two measurement techniques related to SAW generation and detection, and optimization of SAW generation. Our optimization consists of two different improvements. The first is the improvement of the SAW generation efficiency due to the material of the IDT and the development of a pulsed SAW generation technique; we have shown that changing the

material of the IDT from gold to aluminum significantly improves the transfer characteristics of the IDT. This improves the generation intensity of SAWs and makes it possible to realize position-specific transport of electrons, as described below (Chapter 4). Furthermore, the frequency shift of the generated SAW caused by the weight of the IDT is also greatly improved, enabling SAW generation at the desired frequency even when multiple frequencies are involved. These improvements are a key factor in the success of the second optimization, the generation of pulsed SAWs with a single minimum. Because it is necessary to superimpose SAWs of multiple frequencies with the same intensity and in-phase. The development of pulsed SAWs greatly expands the degree of freedom of single electron control by SAWs and sets the standard for highly efficient electron transport techniques between QDs [WOE$^+$22]. Furthermore, it will open up new possibilities in experiments that have been conducted with ordinary SAWs, leading to the development of scalable on-demand single electron sources as described below (Chapter 5).

Chapter 3

In-flight distribution of an electron within a surface acoustic wave

3.1 Introduction

SAWs have large potential to realize quantum-optics-like experiments with single flying electrons employing their spin or charge degree of freedom. For such quantum applications, highly efficient trapping of the electron in a specific moving QD of a SAW train plays a key role. Probabilistic transport over multiple moving minima would cause uncertainty in synchronisation that is detrimental for coherence of entangled flying electrons and in-flight quantum operations. It is thus of central importance to identify the device parameters enabling electron transport within a single SAW minimum. A detailed experimental investigation of this aspect is so far missing. Here we fill this gap by demonstrating time-of-flight measurements for a single electron that is transported via a SAW train between distant stationary QDs. Our measurements reveal the in-flight distribution

of the electron within the moving acousto-electric quantum dots of the SAW train. Increasing the acousto-electric amplitude, we observe the threshold necessary to confine the flying electron at a specific, deliberately chosen SAW minimum. Investigating the effect of a barrier along the transport channel, we also benchmark the robustness of SAW-driven electron transport against stationary potential variations. Our results pave the way for highly controlled transport of electron qubits in a SAW-driven platform for quantum experiments.

The use of sound enables nanoelectronic implementations that often resemble quantum-optics experiments within an original acousto-electric solid-state framework. A prominent example of this development is SAW technology, which is well-established in consumer-electronics industry and currently celebrates its revival in quantum science[For17, BGM$^+$18, DCS$^+$19]. The acousto-electric medium can serve for instance as resonator [GAK$^+$14, MKP$^+$17, ASG$^+$19] or messenger[SZC$^+$18, BSZ$^+$19] of quantum information from superconducting qubits. However, a SAW can also be employed to transport a charged quantum system as a whole what is particularly interesting for semiconductor-qubit architectures[VBC$^+$17] and experimental investigations of quantum nonlocality with Fermions[BBB$^+$00]. The acousto-electric potential modulation of the SAW drags a single electron with its quantum properties from one surface-gate defined QD through a transport channel to another QD [HTY$^+$11, MKF$^+$11, BHT$^+$16]. The SAW-driven transport technique allows high transfer efficiency $P > 99\%$ even in single-electron circuits of coupled transport channels[TEL$^+$19]. Owing to this robustness, the acousto-electric method is capable to shuttle spin-entangled electron pairs between distant QDs without significant additional decoherence[JMC$^+$21]. The exact transport process remains however an aspect that is yet

not fully understood: Is the electron loosely surfing on a shallow potential wave or is it well-confined within a specific location of the wave train?

To study the physics of electron-transfer techniques, time-resolved measurements have emerged as a useful and reliable tool[SHH04]. In the quantum-Hall regime, fast voltage-pulse probing has been employed to study the interaction of edge states[KKH$^+$14] and it was applied to demonstrate the dynamics of single electrons emitted from a QD pump[KJE$^+$16a]. Recently, time-of-flight measurements have been performed in a similar manner in non-chiral mesoscopic conductors[RAG$^+$18]. For SAW-driven single-electron transport, pulsing techniques have been proposed[HTY$^+$11] and were applied to trigger single-electron transport at a specific location of the acousto-electric wave train [TEL$^+$19, JMC$^+$21]. However, detailed time-of-flight measurements have not yet been performed.

Here we present a pulse-probe technique that allows the measurement of the electrons in-flight distribution as it passes with the SAW at a specific point of a transport channel. To perform the time-of-flight measurement, we first apply a ps-voltage pulse to the reservoir gate (R) of the source QD, which allows us to load the electron into a specific SAW minimum. Subsequently, we apply another ps-pulse on a barrier gate (#1 or #2) that is placed along the transport channel as the SAW train passes with the flying electron. Sweeping the delay of this probe event, we scan the presence of the electron and map its in-flight distribution for each SAW minimum. By changing the acousto-electric amplitude we estimate the threshold necessary to confine the electron in the initially loaded SAW minimum. Introducing a local surface-gate controlled barrier along the transport channel, we investigate in addition the effect of a stationary potential variation on the in-flight

distribution and compare the experimental results to potential simulations. The present time-resolved investigation provides an important benchmark for the acousto-electric amplitude and the potential homogeneity that is required to perform robust SAW-driven qubit transport and in-flight quantum operations.

3.2 Experimenatl setup

The experiment is performed at a temperature of about 20 mK within a ^{3}He/^{4}He dilution refrigerator. A Si-modulation-doped GaAs/AlGaAs heterostructure serves as basis of the investigated sample that is schematically shown in Fig. 3.1a. The 2DEG that is located 110 nm below the surface has an electron density of $n \approx 2.7 \times 10^{-11}$ cm^{-2} and a mobility of $\mu \approx 10^6$ cm^{2}V^{-1}s^{-1}. The main component of the sample is a surface-gate-defined transport channel whose ends are equipped with a quantum dot (QD) serving respectively as single-electron source and receiver. A SEM image of the transport channel is shown in Figure 3.1b with schematics indicating the experimental setup. The Schottky gates of the nanostructure are made out of a metal stack of 3 nm titanium and 14 nm gold. During the cool down a voltage of 0.3 V is applied to all electrodes. At low temperature, we completely deplete the 2DEG lying below the 20 µm-long transport channel and control the source and receiver QD via a set of negative voltages. The occupation of each QD is sensed via the current flowing through an adjacent QPC.

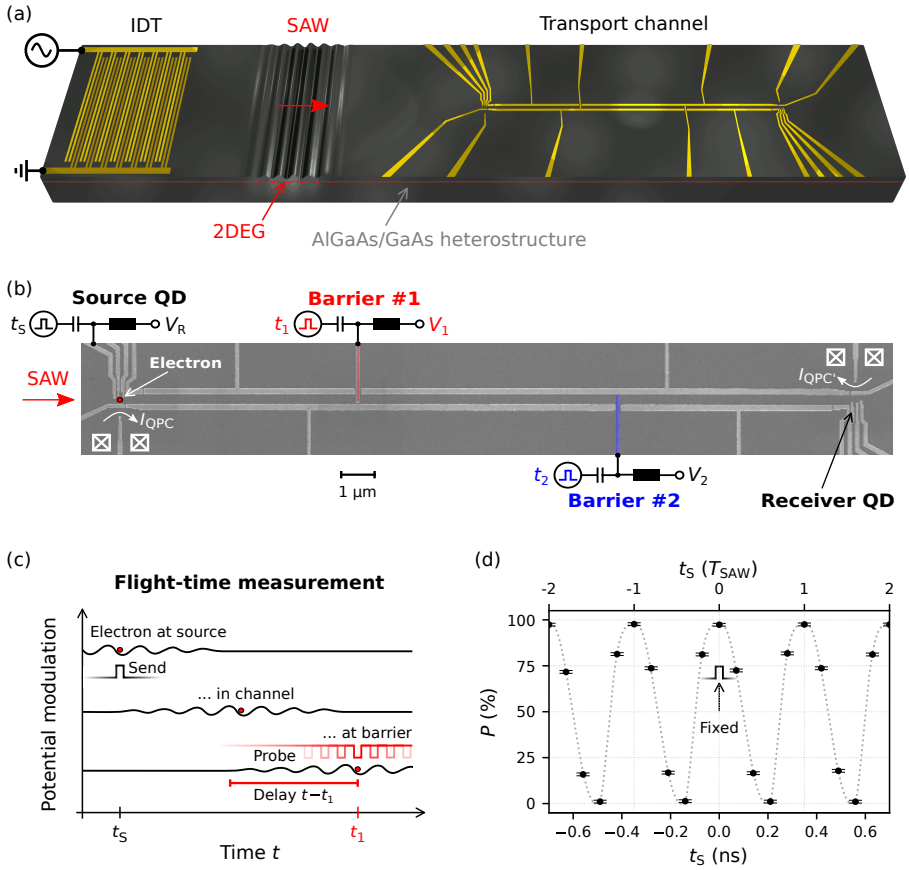

Figure 3.1: Experimental setup. **(a)** Schematic the AlGaAs/GaAs sample showing an interdigital transducer (IDT) that launches a SAW train towards the surface-gate defined transport channel. **(b)** SEM image of transport channel showing source and receiver quantum dots (QD) with schematic indication of quantum-point-contact (QPC) charge detectors and the voltage-pulse to perform the time-of-flight measurement. **(c)** Schematics showing principles of the controlled sending process at the source and principle of the time-of-flight measurement. **(d)** Transfer probability, P, as function of the sending pulse t_S. The probability values P are obtained from $N = 13\,000$ single-shot transmissions with error $\Delta P = 1/\sqrt{N}$. The dotted line serves as guide to the eye. The arrow indicates the delay of the sending pulse that is kept fixed for the time-of-flight measurements.

3.3 Flight-time measurement

An IDT is placed far to the left of the nanostructure which allows single-shot emission of a SAW train – with 1 µm wavelength – that propagates with a speed of $v_{SAW} \approx 2.86\,\mu m/ns$ towards the transport channel. The SAW wavelength λ_{SAW} is determined by the period of the metallic fingers of the IDT. For the presently investigated device the SAW wavelength is 1 µm. From the measured resonance frequency of the IDT, $f_0 =$

2.86 GHz, the SAW velocity is deduced from $v_{\mathrm{SAW}} = \lambda_{\mathrm{SAW}} \cdot f_0$. The input signal for the IDT stems from an output channel of an AWG. In order to shuttle a single electron from one QD to the other, we employ the potential modulation that accompanies the SAW in the piezoelectric substrate. At the depleted transport channel, this acousto-electric modulation forms a train of potential minima that is capable to move the electron. We trigger the SAW-driven sending event via the reservoir gate (R) of the source QD that is connected to an AWG output. To carry out the time-of-flight measurement, additionally, two barriers (#1 and #2) are placed along the channel that are also linked to AWG outputs.

Before the emission of the SAW train, an electron is loaded at the source QD and prepared in a protected configuration where the acousto-electric wave cannot pick up the electron. In this sending configuration a slight potential variation is however sufficient to move the electron from the stationary source QD into one of the moving QDs that accompanies the SAW train along the transport channel – see red schematic in Figure 3.1c. At the same time, we prepare the receiver quantum dot in a configuration where we can catch the moving electron. Figure 3.1d shows the transfer probability as function of the source-pulse delay, t_{S}. As in previous investigations[TEL$^+$19], we find that t_{S} must coincide with a specific acousto-electric pressure phase of the SAW in order to enable the electron's transfer from the stationary source QD into a specific location within the SAW.

To perform the time-of-flight measurement, we fix the timing of the sending trigger ($t_{\mathrm{S}} = 0\,\mathrm{ns}$) and sweep the delay of a probe pulse t at the according barrier over the arrival window of the SAW. We have chosen the probe-pulse width as two fifths of the SAW period T_{SAW} in order to optimize pulsing efficiency and time resolution. The delay of the probe pulse is stepped in multiples of the period T_{SAW} with a time offset enabling coinci-

dence with the pressure phase of the SAW. If the probe pulse overlaps with a certain SAW minimum, it enables thus a potentially present electron to pass. Otherwise, the passage of the electron is blocked leaving the electron behind the barrier in the subsequent SAW period. Let us first consider the hypothetical case where the electron is well-confined in a specific SAW minimum. In this case, the transfer probability is zero for a barrier-pulse delay before the electron arrival. For any delay in the pressure phase after the arrival, the electron is on the other hand certainly transmitted, since it is blocked before the barrier until the probe pulse is present. Following this measurement approach, the instantaneous distribution of the electron within the passing SAW train, $D(t)$, is directly reflected via the derivative of the transfer probability, P, with respect to the time-delay, t, of the probe pulse if the effect of the barrier pulse is fully deterministic (block or transmit). We estimate the uncertainty in $D(t)$ via error propagation as approximately three times the error of $P = 1/\sqrt{N}$ where N indicates the number of single-shot transfers. For a deterministic probe pulse and single-minimum transport, $D(t)$ should follow a delta function at the SAW location expected from the triggered sending event (t_S).

Let us first perform the time-of-flight measurement at the maximum achievable IDT input power of about 288 mW (24.6 dBm). Based on SAW-modulated Coulomb-peak data[TEL$^+$19, SKF$^+$06] , we estimate that this input power introduces a SAW with amplitude $A_{SAW} \approx (24 \pm 3)$ meV. We estimate the expected arrival time (t_1) at barrier #1 from its distance to the source QD (x_1) as $t_1 = x_1/v_{SAW} \approx (2.23 \pm 0.05)$ ns. Sweeping the delay of the probe pulse on barrier #1 over the time window around t_1, we measure the transfer probability $P(t)$ as shown in Fig. 3.2a. The data follows a step function that is centered at t_1 what verifies the deterministic effect of the barrier pulse and transport

in a specific SAW position. It is important to note, that the binary probing process is achieved via the sample design allowing a spatial separation of the probing barrier to the catching event at the receiver QD. Evaluating the electron distribution $D(t)$, we find that the electron is confined during transport with a certainty of $(97 \pm 2)\%$ at the position of the SAW train ($t - t_1 = 0$), where the electron was initially loaded with the ps-voltage pulse. We suspect that even more confinement is achievable if the SAW amplitude would be further increased.

In order to investigate this aspect in more detail, let us focus on the threshold of SAW amplitude below which confinement breaks down. For this purpose, we repeat the time-of-flight measurement at the first barrier with gradually decreasing SAW amplitude as shown in Fig. 3.2b. At a SAW amplitude of about 19 meV, we observe partial electron arrival one SAW minimum earlier than expected ($t - t_1 = -T_{\mathrm{SAW}}$). For a SAW amplitude below 15 meV, we find the arrival distribution also spreading over SAW minima subsequent to the expected location. We quantify the magnitude of electron displacement by plotting $D_0 = D(t_1)$ as function of the SAW amplitude as shown in Fig. 3.2c. The data shows significant ($D_0 > 95\%$) in-flight confinement of the transported electron for a SAW amplitude exceeding a threshold of (24 ± 3) meV. The course of the data indicates that increased SAW amplitude indeed allows maximization of in-flight confinement.

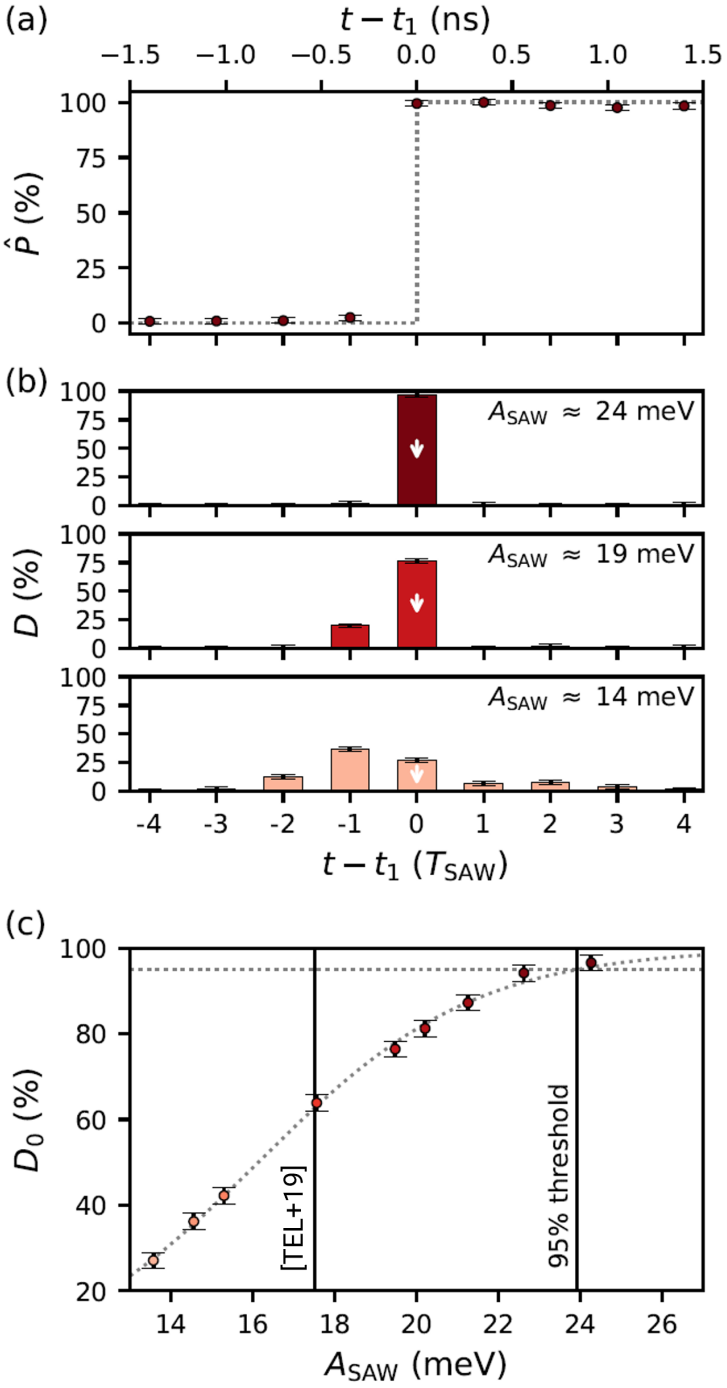

Figure 3.2: Time-of-flight measurement at barrier #1. **(a)** Normalized transfer efficiency $\hat{P}$ as function of delay on the probe pulse t. Each data point is derived from $N = 25\ 000$ single-shot transmissions with error $\Delta P = 1/\sqrt{N}$. The dotted line shows a step function centered at the expected arrival time t_1. **(b)** In-flight distribution $D(t)$ of the electron within the SAW train for different values of the peak-to-peak SAW amplitude A_{SAW}. The data is obtained via the normalized derivative of $P(t)$ with uncertainty $\Delta D \approx 3 \cdot \Delta P$. The arrows indicate the confinement fidelity $D_0 = D(t_1)$. **(c)** D_0 as function of SAW amplitude A_{SAW}. The dotted curves show a guide to the eye (sigmoid function) and the 95% threshold. The two vertical lines indicate the SAW amplitude employed in a previous work[TEL$^+$19] and the amplitude for significant confinement.

3.4 The effect of a potential barrier

The presence of two controllable barriers along the transport channel allows to study the effect of an intermediate potential variation on the time-of-flight distribution. For this purpose, we probe the electron's arrival at the second barrier. There, we expect the electrons passage at a time of $t_2 = x_2/v_{\mathrm{SAW}} \approx (4.86 \pm 0.05)$ ns where x_2 indicates the distance of barrier #2 to the source QD. On the first barrier, we apply no voltage pulse, but only change the static voltage V_1. Figure 3.3a shows data of such a time-of-flight measurement with intermediate barrier. Here, we keep the SAW amplitude at the maximum achievable value. Despite the presence of the intermediate barrier, the data shows a confinement fidelity $D_0 > 80\%$ in the voltage range between $-217\,\mathrm{mV}$ to $-25\,\mathrm{mV}$. Beyond this range, we observe a rapid drop of D_0 due to in-flight transitions of the electron in neighboring SAW minima. The presence of the intermediate barrier causes a reduction of the confinement fidelity compared to a smooth potential along the transport channel.

3.5 Discussion via potential simulations

To understand the experimental result better, let us compare the time-of-flight data to potential simulations along the transport channel. The potential calculation is performed via the commercial Poisson solver nextnano[BZA$^+$07] assuming a frozen charge layer and deep boundary conditions[HCR$^+$18]. As input parameters, we consider the gate geometry and the voltages applied as well as the intrinsic properties of the heterostructure. Figure 3.3c shows the course of the resulting potential minimum U_{min} across the

first barrier for three values of the voltage V_1 beyond the 80%-confinement threshold. It can be seen that even the optimal barrier gate setting produces a change in potential of nearly 20 meV. This would inhibit electron transport by SAWs, which have a maximum amplitude of 24 meV in this experiment, and would have a particularly large effect for weak SAWs. The blockade of the electron for a very high ($V_1 < -217$ mV) and very low ($V_1 > -25$ mV) potential barrier is caused by different effects. For increasingly negative barrier voltage, a potential barrier is formed. Interestingly, the formation of the barrier comes along with the event, where the electron arrives one SAW minimum earlier as apparent in Fig. 3.3a for $V_1 = -275$ mV at $t - t_2 = -1 \cdot T_{\mathrm{SAW}}$. We speculate that the advancement is caused via non-adiabatic transitions of the electron in excited states when ramping against the barrier. For increasingly positive voltage such as $V_1 = 0$ mV, we observe on the other hand mainly transitions in subsequent SAW minima ($t - t_2 > 0$) due to trapping in a quantum-dot like potential structure. The time-of-flight measurement at the second barrier shows that single-minimum transport is feasible even if significant potential gaps are present along the transport channel. We suspect that maximized acousto-electric confinement (via increased SAW-amplitude and -frequency) enables single-electron transfer that is fully protected against local potential variations.

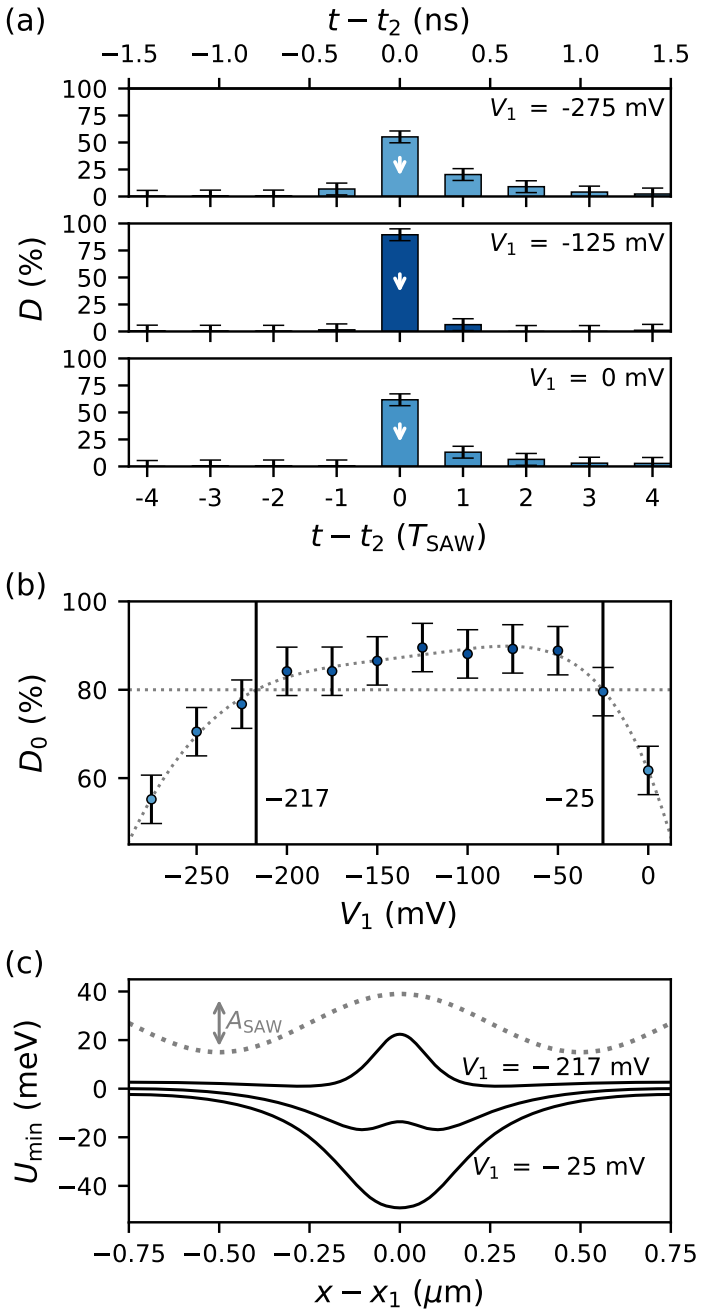

Figure 3.3: Time-of-flight measurement at barrier #2. **(a)** In-flight distribution $D(t)$ of the electron within the SAW-train for selected voltages V_1 applied on the first barrier gate. The measurement is performed with maximum SAW amplitude of about 24 meV. Each data point is derived from $N = 3\ 000$ single-shot transmissions with undertainty $\Delta D \approx 3/\sqrt{N}$. **(b)** Confinement fidelity $D_0 = D(t_1)$ for different values of V_1. The dotted curves show a guide to the eye (polynomial fit) and the 80% threshold. **(c)** Minimum U_{min} of the electron potential across the first barrier three selected voltages: -217 mV, -121 mV and -25 mV. The dotted curve shows the potential modulation of the applied SAW for comparison with indication of its peak-to-peak amplitude A_{SAW}.

3.6 Conclusion

The ability to detect the exact location of a SAW-transported electron is essential to identify the critical device parameters enabling single-electron transport within a specific, deliberately chosen SAW minimum and thus flying-qubit implementations. Employing a pulse-probe technique, we have demonstrated time-of-flight measurements revealing the arrival distribution of such a flying electron for each moving potential minima that accompanies the SAW along a transport channel. As we send a SAW train with sufficiently large peak-to-peak amplitude – that is (24 ± 3) meV for the presently investigated device –, the time-of-flight data indicates an electron-confinement fidelity exceeding 95% within a specific moving QD. Investigating the effect of an intermediate surface-gate-defined barrier within the transport channel, we demonstrate a confinement fidelity larger than 80% over a voltage range of about 200 mV despite the presence of the local potential variation. Our measurements show that acousto-electric in-flight confinement plays the key role to make a SAW-driven single-electron circuit robust. We anticipate that our experimental findings foster the development and application of SAW-generation approaches [SZA$^+$15, EAR$^+$17, DSP$^+$19, NRK20] paving the way for SAW-driven electron-quantum-optics implementations [BSR00, ASLO$^+$17, SKG$^+$17, LLASB20] and quantum-metrology applications[SMT$^+$96, TSP$^+$97, CTS$^+$99, CTS$^+$00, EPA02, PUL03]. In fact, this achievement has enabled the previously impossible synchronous transport of multiple single electrons, and has led to experiments in which single electrons are transported synchronously from two quantum dots, collide in a coupled quantum wire, and observe antibunching due to Coulomb interactions

[WER+23].

Chapter 4

On-demand single-electron source using surface acoustic wave pulses

4.1 Introduction

A typical setup for a single-electron source using SAWs combines a QD, a transport channel, and an IDT. A single electron is prepared in the QDs and transported along the depleted transport channel by the SAWs. By using sufficiently strong SAWs, the transport of electrons becomes highly robust, and an electron is transferred while confined to a specific potential minimum of the SAWs as described in Chapter 3. This allows us to control the transfer timing of an electron and hence synchronized transfer of single electrons from multiple single-electron sources is possible. Another important development is a technique to generate a single-cycle SAW pulse using a chirp IDT as described in Chapter 2. Employing the SAW pulse for single-electron transfer allows us to synchronize the timing of electron transport from multiple single-electron sources without ps-triggering

each QD [TEL$^+$19]. This is advantageous for scaling up the system since we do not need to implement an RF line for each QD used as a single-electron source. On the other hand, in these previous studies, the single electron ejected had to be prepared in the quantum dot first. Thus, each single-electron source required a QD and a complex fast voltage sequence. This indicates that there is still room for improvement in the scalability of the system. Furthermore, the time-consuming electron preparation process is a speed limiting factor for the entire electron flying qubit system that utilizes single electron charges in flight.

For metrology applications, regular SAWs are used with a depleted quantum rail consisting of two metal gates to realize a quantized current source [SMT$^+$96, TSP$^+$97, CTS$^+$99, CTS$^+$00, EPA02, KFB$^+$06]. Electric potential modulations accompanied by the SAWs pick up an integer number of electrons directly from the Fermi sea and transfer them over the quantum rail. As a result, the current, $I = nef$, where n is an integer, e is the elementary charge, and f is the frequency of the SAWs. Here when a single-cycle SAW pulse rather than regular SAWs is used with a depleted quantum rail, an on-demand single-electron source rather than a continuous quantized current source can be realized. In contrast to the single-electron source with a QD, the electron capturing process before applying SAWs is not required. Hence, its operation could be faster. Furthermore, a chirp IDT can generate multiple SAW pulses with arbitrary delays, making it possible to generate single electrons with flexible arbitrary delays. So far, for metrology high accuracy electron pumping (an error rate $\leq 10^{-6}$) is reported in other methods [KMZS96, SDF$^+$15, YGK$^+$16, BKL$^+$07]. SAW pumps have not been actively studied for standard application due to its limited accuracy (an error rate $\geq 10^{-4}$), nevertheless

their application to quantum information processing may not require the same level of high accuracy as the current standard, and as mentioned above, active research is underway.

Based on this idea, in this chapter, we actualize an on-demand single-electron source consisting of a chirp IDT and a quantum rail for enabling the implementation of electron flying qubits with beam-splitters [ITL+21, WER+23]. We evaluate the performance of this single-electron source by repeatedly operating the single-electron source and by measuring the accuracy of the generated quantized current. In addition, we demonstrate that the delay between the successively transferred single electrons can be arbitrarily adjusted. Finally, we investigate the effect of electromagnetic crosstalk generated by driving the IDT on the accuracy of the single-electron source.

4.2 Experimental setup

The experiment is performed within a 4 K pulse tube refrigerator. A Si-modulation-doped GaAs/AlGaAs heterostructure is used to fabricate the sample. The 2DEG that is located at 100 nm below the surface has an electron density of $n \approx 2.8 \times 10^{11}\,\mathrm{cm}^{-2}$ and a mobility of $\mu \approx 9 \times 10^{5}\,\mathrm{cm}^{2}\mathrm{V}^{-1}\mathrm{s}^{-1}$. Fig. 4.1a shows a schematic diagram of the device and the experimental setup. The device contains a quantum rail with a lithographic width of 0.8 µm and a length of 2 µm, defined by surface Schottky gates. The gates are made of a thin metal film consisting of 3 nm titanium and 14 nm gold. During the cooldown of the device, a voltage of 0.35 V is applied to all the gates. The 2DEG around the gates is depleted by applying negative voltages. Fig. 4.1b shows a conductance across the quantum rail as a function of the voltage V_t and V_b. For this measurement, we

inject a current by applying a DC bias voltage (336 μV) to the contact O_r and measure the current recovered from the contact O_l. In the following measurements, we set the voltages V_t, V_b to be more negative than -2.1 V, where the current driven by the bias voltage does not flow. A chirp-IDT is placed on the sample surface 1.4 mm to the left of the quantum rail. The surface electrodes of the IDTs are made of a thin metal film consisting of 3 nm titanium and 27 nm aluminum. To reduce internal reflections at resonance, we employ a double-electrode pattern for the IDT. The IDT aperture is 30 μm, and the SAW propagation direction is along [110]. The IDTs are designed and simulated with the homemade open-source Python library "idtpy" [NOT]. A signal for generating SAW is produced by an AWG (Keysight M8190A). This signal subsequently passes through two high-frequency amplifiers (SHF S126A and ZHL-4W-422+) at room temperature before being inputted into the chirp IDT. The generated SAW can be observed by a high-speed sampling oscilloscope (Keysight N1094B DCA-M) via the broadband detector IDT after being amplified by a broadband amplifier (SHF S126A) at room temperature.

4.3 SAW pulse for single-electron generation

Here a chirp IDT is designed to generate SAWs with frequencies ranging from 0.5 GHz to 3.0 GHz. By applying an appropriately time-dependent high-frequency voltage to this IDT, it is possible to generate strongly compressed SAW pulses. The gray solid line in Fig. 4.1c is a strongly compressed SAW pulse observed by the detector IDT. This waveform is distorted from the actual shape of the SAW that passes through the quantum rail, due to the frequency bandwidth of the detector. To find the waveform of the SAW transporting electrons, we performed a simulation using the impulse-response model. First, we

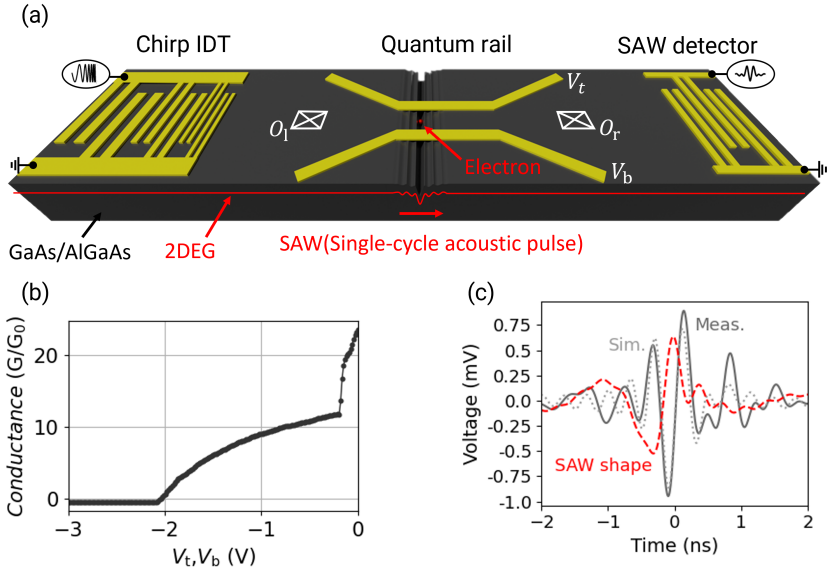

Figure 4.1: **(a)** Experimental setup. Schematic of a chirp IDT emitting a compressed SAW towards a quantum rail and a broadband SAW detector, showing a perspective view of the sample that is realized via a metal surface gate in a GaAs/AlGaAs heterostructure. **(b)** Conductance across the quantum rail as a function of the voltages V_t and V_b. The current is measured from the ohmic contact O_l while applying a DC bias voltage (336 µV) to the ohmic contact O_r. $G_0 = 2e^2/h$, where e is the electron charge and h is the Planck constant. **(c)** Trace of the broadband detector's response to the compressed SAW generated by the chirp IDT (gray solid line) with impulse-response simulation (light gray dotted line) and the corresponding SAW shape (red dashed line) which is derived by deconvolving the detector response to remove the contribution of the detector IDT in the simulation. The measurement is performed at 4 K.

simulated the waveform of the SAW including the detector-IDT component (light gray dotted line in Fig. 4.1c). Then, by subtracting the detector-IDT component, the waveform of the SAW in the device was simulated (red dashed line in Fig. 4.1c). The result indicates that a SAW pulse with one dominant minimum can be generated. What we would like to focus on here is the shape of the SAW pulse. This shape is optimized to smoothly pick up single electrons from the Fermi sea and transport them across the depleted quantum rail, which differs from the symmetrical shape as generated in Chapter 2. As a result of optimization, an asymmetric SAW pulse with a sharp edge after the minimum value was obtained.

4.4 On-demand single electron generation

It has been demonstrated that acousto-electric currents can be generated by applying SAWs to a depleted quantum rail [SMT+96]. Here the superposition of the longitudinal dynamic potential of the SAW and the transversal confinement potential of the quantum rail forms a train of moving QDs that picks up electrons from the Fermi sea and carries them across. The average number of electrons carried in each dynamic QD is determined at the entrance of the quantum rail by the balance between the potential gradient towards the entrance of the quantum rail and the confinement potential of the moving potential minima. When the potential gradient of the dynamic QD becomes steeper due to changes in the voltage of the quantum rail or the waveform profile of the SAW, the spacing between the energy levels of the electrons in the QD widens and the charging energy of the QD increases. For a sufficiently large charging energy, the number of electrons within each dynamic QD is stably quantized. When each dynamic QD contains n electrons, where n is an integer number, the device works as a continuous quantized-electron source and generates a quantized current, $I = nef$, where f is the frequency of the sinusoidal SAW. Here we investigate such a quantized current source with the single-cycle acoustic pulse shown above. By repeatedly sending the SAW pulse to the depleted quantum rail we generate an observable quantized current and evaluate the accuracy of the single-electron transport by each SAW pulse from the stability of the current quantization. In this experiment, we set the repetition period of the SAW pulse to $T_{\mathrm{cycle}} = 1280\,\mathrm{ns}$. When the number of electrons transported by each SAW pulse is quantized to an integer number n, the quantized current, $I = ne/T_{\mathrm{cycle}}$, is expected to be observed. Since we can arbitrarily

control the timing of the SAW-pulse generation with a chirp IDT, this electron source can be considered as an on-demand quantized electron source.

Fig. 4.2 displays the acousto-electric current as a function of the gate voltage of the quantum rail for different SAW amplitudes. When the gate voltage is swept to a more negative value, the potential gradient at the entrance of the quantum rail increases. As a result, a smaller number of electrons is transported across the depleted quantum rail by the SAW-dynamical potential. For the smaller SAW amplitude, the potential gradient of the SAW-dynamical potential is smaller and the charging energy of the dynamic QD at the entrance of the quantum rail is not large enough to have a stable number of electrons in each dynamic QD. This results in the acousto-electric current smoothly decreasing as a function of the gate voltage. In contrast, for the larger SAW amplitude, the charging energy increases, and a kink is developed at e/T_{cycle}. To evaluate the quantization of the acoustic-electric current, we focus on the region where the gradient of the kink is the flattest as indicated in red dots in Fig. 4.2. We calculated the normalized difference,

$$I_{\mathrm{N}} = |(I_{\mathrm{ave}} - e/T_{\mathrm{cycle}})/(e/T_{\mathrm{cycle}})|,$$

between the average of measured acousto-electric current I_{ave} and ideal estimated value e/T_{cycle} with a combined standard uncertainty. The acoustic-electric current took into account the current without SAW as offset and the gain of the current amplifier calibrated by a standard resistance. As a result of the calculation, in the flattest region (the gate voltage width of 24 mV), the difference between the acousto-electric current and the theoretical quantized current is 3.7% or less . This indicates that the kink caused by the SAW well matched the ideal quantized current. This result implies that in the kink, the average

number of electrons in each SAW pulse is close to one. Around there, the device can be operated as an on-demand single electron source.

In this method, single electrons can be generated without preparing electrons, offering faster operation than conventional on-demand single-electron sources using SAWs. Additionally, the interval of SAW pulses can be flexibly controlled, making it possible to generate single electrons with any desired delay as discussed in the following section.

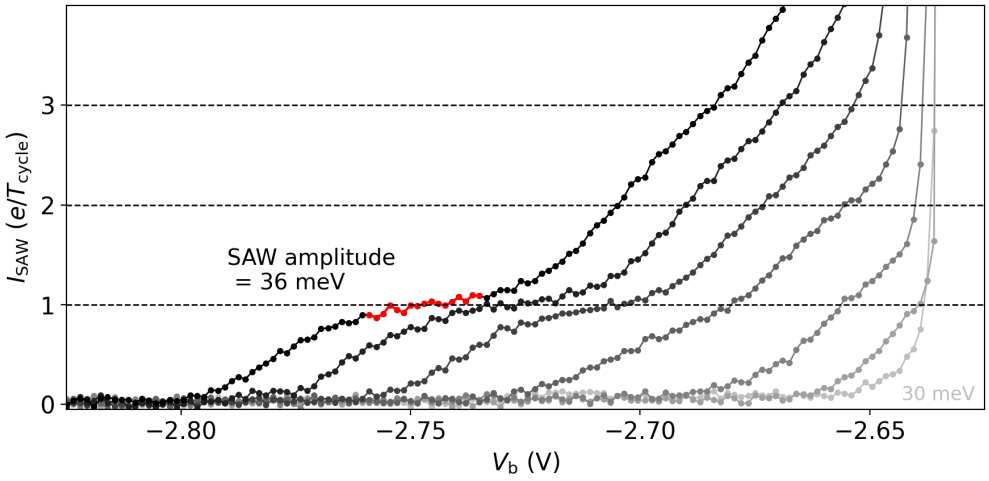

Figure 4.2: Acousto-electric current, I_{SAW}, induced by the compressed SAW pulse as a function of the voltage V_b with $V_u = -2.2$ V. The SAW amplitude varies from 30 meV to 36 meV (from right to left) . The range indicated in red is a flat region where the gradient is less than a certain value of the most left curve .

4.5 Single-electron generation with an arbitrary delay

In the previous section, the interval between successive SAW pulses was set to 1280 ns, which is longer than the length of the SAW generation signal of 130 ns. By setting the interval longer, the SAW generation signals did not overlap each other. However, it is also possible to generate SAW pulses with shorter intervals by purposely overlapping the SAW generation signals. In this section, we use this technique to verify the operation of

a single electron pump with arbitrarily controlled delay and explore its potential for high-speed operation. One limitation to keep in mind is the maximum output power of the high-frequency amplifier used: when two SAW generation signals overlap, the maximum amplitude of the individual SAW pulses only reaches half the normal amplitude. This limitation reduces the flatness of the quantized current kink. Nevertheless, despite this reduced flatness, our data still exhibit distinguishable characteristics of a single-electron pump as the kinks seen in Fig. 4.3. Fig. 4.3 presents the acousto-electric current as a function of the gate voltages when we control the delay between two successive SAW pulses within T_{cycle} between 2 ns and 30 ns. The kinks will appear at $2e/T_{\mathrm{cycle}}$ since we send two SAW pulses within T_{cycle}. For the delays shorter than 9 ns the kinks appear at unstable positions. Whereas, for the delays larger than 9 ns the $2e/T_{\mathrm{cycle}}$ quantization current is stably observed. We attribute this result to the presence of small acoustic fluctuation before and after the main acoustic minimum. These extra fluctuations of the SAW pulse overlap with the main minimum of the other SAW pulse, preventing stable electron generation. When a chirp IDT with a wider frequency bandwidth is developed, such extra fluctuation can be suppressed, and a shorter delay time than 9 ns would be possible. In principle, the delay time can be shortened down to the width of the primary minimum, which is approximately 1 ns in this study. In our current chirp IDT, the delay can be arbitrarily controlled above 9 ns.

4.6 Effect of electromagnetic crosstalk

For the stable electron-pump operation, the influence of electromagnetic crosstalk has to be taken into account. In the process of exciting an IDT to generate a SAW, an elec-

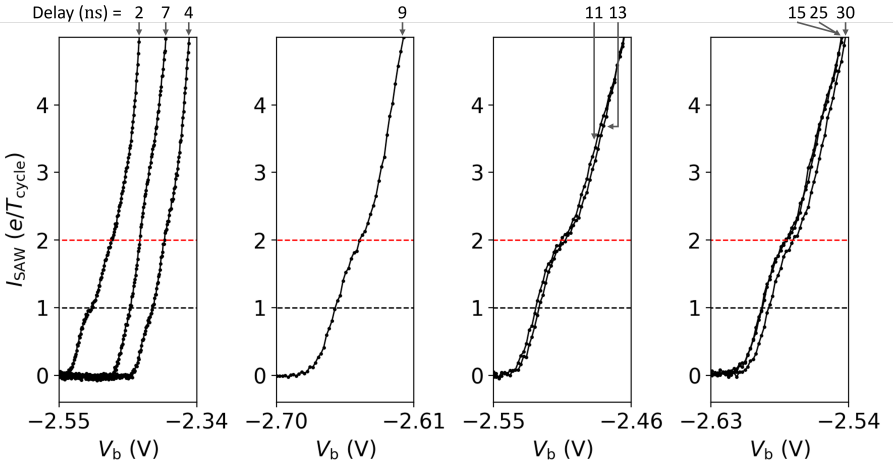

Figure 4.3: Acousto-electric current, I_{SAW}, as a function of the voltage V_{b}. Two SAW pulses within T_{cycle} with changing delay between the pulses. Delay (ns) is indicated above each curve. The red line indicates the expected quantized current $2e/T_{\mathrm{cycle}}$. Each measurement was performed under optimal conditions (i.e. different gate voltages and cool downs) for the SAW-pulse shape at each delay. Thus, the range of V_b varied for each measurement. For clarity, each set of curves is displayed in separate panels.

tromagnetic wave is concurrently emitted from the IDT. This emanation disrupts the surrounding potential of the nanostructures such as the quantum rail, thereby impeding the stability of electron-pump operations. In previous single-electron transfer experiments with SAWs, the difference in velocity between SAWs ($v_{\mathrm{SAW}} = 2.81\,\mu\mathrm{m/ns}$) and electromagnetic waves was used to avoid the simultaneous arrival of SAWs and electromagnetic waves to the nanostructures and to suppress the influence of such crosstalk. The influence of electromagnetic crosstalk on a single-electron pump using a standard IDT has been discussed and pointed out as an important problem previously [KFB$^+$06]. There, the crosstalk was suppressed by the pulsed operation of the IDT and by avoiding the simultaneous arrival of SAWs and electromagnetic waves. When a standard IDT with a single resonant frequency is excited by pulsed sinusoidal waves, a narrow frequency bandwidth of the standard IDT results in a finite rise (fall) time of SAWs, where a gradual change of the SAW amplitude makes single-electron pump operation unstable. As a result, it

is not possible to avoid the influence of electromagnetic crosstalk with a standard IDT while keeping a highly accurate single-electron pump operation. On the other hand, the SAW pulses generated by our chirp IDT do not have a rise (fall) time but only a single-potential minimum transporting electrons. Therefore, we can arbitrarily switch on and off the driving of the chirp IDT without degrading the stability of electron-pump operations. In the present device, from the distance between the IDT and the quantum rail, the SAW reaches the quantum rail approximately 505 ns after its generation at the IDT. The electromagnetic crosstalk propagates with a velocity of light and reaches the quantum rail immediately after its generation at the IDT. The influence of the crosstalk can be suppressed by shifting the timing of the SAW pulse arrival at the quantum rail and the timing of the SAW generation signal input to the IDT as shown in Fig. 4.4a. Fig. 4.4b shows the influence of the electromagnetic crosstalk on acousto-electric transport. Here, the number of SAW pulses within one cycle T_{cycle} is fixed at 2, changing only the timing of the SAW pulses. As a result, for one condition (red curve in Fig. 4.4b) the SAW pulses and electromagnetic waves reach the quantum rail at the same time and hence the crosstalk effect exists. For the other case (blue curve in Fig. 4.4b), by avoiding the simultaneous arrival the crosstalk effect is suppressed. When the crosstalk effect exists, stable electron pumping is disturbed and acousto-electric current smoothly changes as a function of the gate voltages. On the other hand, when the crosstalk effect is properly suppressed, a kink appears at the expected value $2e/T_{\mathrm{cycle}}$.

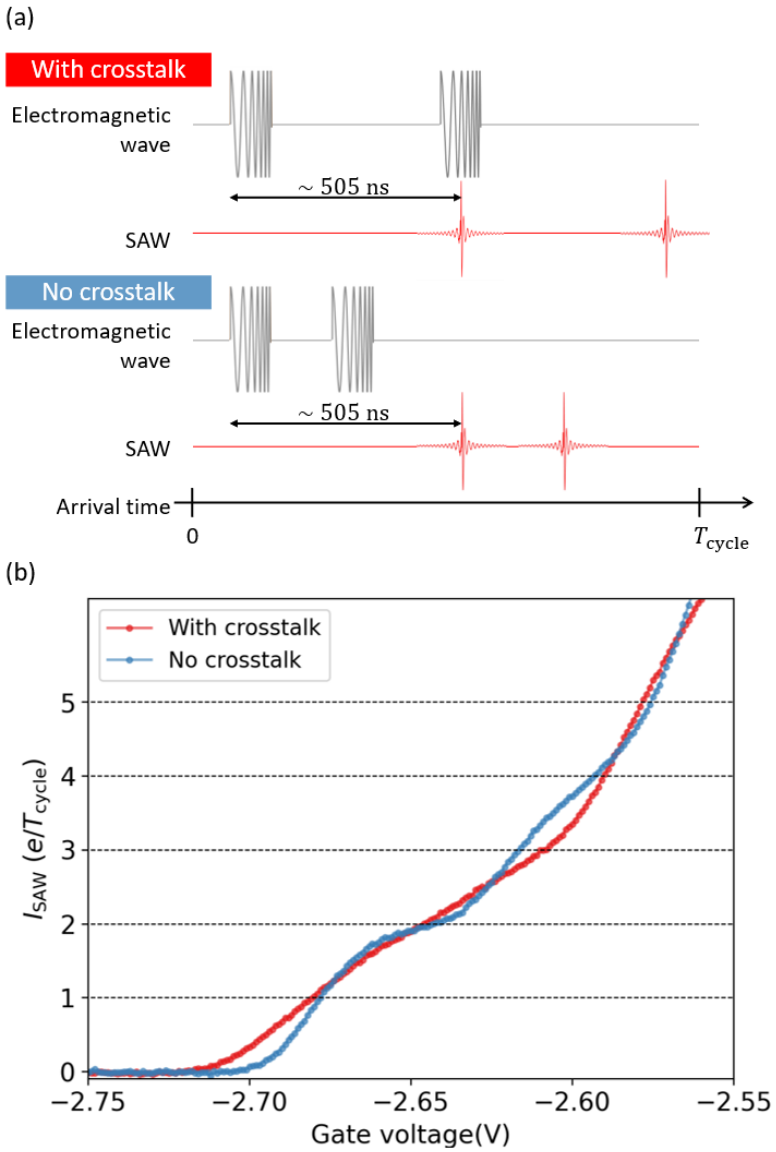

Figure 4.4: **(a)** Schematic of the arrival time of electromagnetic waves and SAW pulses at the quantum rail. The SAW arrives at the quantum rail approximately 505 ns after generation at the IDT. **(b)** Acousto-electric current, I_{SAW}, as a function of the voltage V_{b} with $V_{\mathrm{u}} = -2.06\,\mathrm{V}$ with and without crosstalk.

4.7 Conclusion

In essence, we have demonstrated a simple on-demand single-electron source amalgamating chirp SAW pulses with a quantum rail. We evaluated its performance from the observation of the quantized acousto-electric current generated by repeatedly operating the source. Under the optimal operation condition, the mismatch of 3.7% or less compared to the ideal operation. This single-electron source negates the need for dynamic gate operations to prepare a single electron into the QD, which stands in stark contrast to the formerly demonstrated single-electron source with chirp SAW pulses [WOE+22]. Furthermore, we demonstrated the flexible control of a delay between successive single-electron transfers. Meanwhile, the shortest delay time is limited to 9 ns and the operation accuracy is limited by the maximum available SAW amplitude. The former limitation could potentially be overcome by expanding the bandwidth of a chirp IDT. The latter can be ameliorated by enhancing the conversion efficiency between IDT input signals and SAWs, achievable through the utilization of a thin film of stronger piezoelectric materials than GaAs such as ZnO, $LiNbO_3$ or AlN, or by fine-tuning the impedance mismatch in the IDT. With the improvements the accuracy of the single-electron pump operation will also be enhanced. As the width of the quantum rail (0.8 µm in this work) is much narrower than the wavefront of the SAW ($\sim$ 30 µm in this work and can be even wider), synchronized operations of multiple single-electron sources can be implemented by simply putting multiple quantum rails within the wavefront of a SAW. Notably, each quantum rail can be implemented with at least two or fewer static voltage inputs and does not require complex voltage manipulation. These characteristics facilitate the integration of

many parallel single-electron sources and encourage scale-up of electron flying qubit architectures.

Another important insight gained from this work is the impact of the SAW potential shape on electron transport. A SAW pulse, generated by a chirp IDT, is a superposition of broadband SAWs, thus permitting the deformation of the SAW pulse shape through appropriate adjustment of the input signal to the IDT. This study required significant deformation of the SAW pulse into an optimized asymmetric shape, in order to directly extract an electron from the Fermi sea instead of the QD. It indicates that the previously used symmetric SAW waveform was not the most suitable for electron transport and suggests the direction for further optimization. This insight is not only beneficial for research using SAW but also has important implications for studies on the electron transport process in nanostructures [LKF$^+$23, SSX$^+$22].

Additionally, we explored the effect of the electromagnetic field emitted directly from the IDT on the accuracy of the single-electron source. It has been presented as a factor to degrade the accuracy of electron transfer and pulse modulation of SAWs has been proposed as a solution for that [KFB$^+$06]. However, the narrow bandwidth of the IDT prevented the fast enough pulse modulation to eliminate the influence of the electromagnetic crosstalk. In contrast, the large bandwidth of our chirp IDT and a single-cycle SAW pulse originating from it allow us to completely separate the timing of single-electron transfer across the quantum rail and the arrival of the electromagnetic crosstalk. We clearly demonstrate that the elimination of the crosstalk indeed improves the accuracy of electron transport.

For further improvement of this technique, single-shot measurements using a QD to

detect the generated single electrons are expected to provide additional information on accuracy. In addition, to clarify the distribution of single electrons within a SAW pulse, barrier gates can be used, just like in flight-time measurements [EWO$^+$21]. Furthermore, by making the barrier gate an overlapping gate that lays on top of the transport channel gates instead of cutting the transport channel gates, delicate adjustments that were previously necessary to prevent gap in the potential of the transport channel become unnecessary, allowing verification with a smoother potential of the transport channel.

The results obtained in this study gives important insights into the single-electron transport with moving electric potentials and contribute to the field of single-electron quantum optics using SAWs, such as building up a flying qubit system or quantum communication with single electron (or hole) to single photon conversion [HRC$^+$20]. This study represents steady progress towards the realization of quantum systems using single electrons, providing new techniques and insights that enrich the fundamental understanding of the field.

Chapter 5

Suppression of electromagnetic wave by differential excitation for surface acoustic wave generation

5.1 Introduction

Developments of SAWs often face the persistent problem of electromagnetic wave crosstalk as revealed in Chapter 4. High frequency components in experimental circuits to generate SAWs emit electromagnetic waves while generating SAWs. This electromagnetic wave is picked up by the metal gates of the target structure, which are used to conduct the intended experiments (e.g., the metal gates that define the quantum dots), and generates fluctuation of the electric potential in the target. This undesired fluctuation not only hides the desired effect by the SAW, but also interferes with the SAW to produce a negative effect [KFB$^+$06, OWE$^+$24]. Indeed, this crosstalk is pronounced and should

be one of the reasons why quantum current sources using SAWs were eventually largely abandoned, despite great efforts over the years [SMT+96, TSP+97, CTS+99, CTS+00, EPA02, PUL03, For17].

In the field of electron-quantum optics, the crosstalk problem has been avoided by shifting the arrival timing of the electromagnetic wave and the SAW at the target structure where electrons are transported. This could be done by making the length of the SAW generation signal sufficiently shorter than the propagation time of the SAW from the generated position to the target structure. Since the electromagnetic wave propagates with the speed of light ($3 \times 10^8\,\mathrm{m/s}$), which is 5 orders of magnitude faster than the speed of SAWs ($\sim 3 \times 10^3\,\mathrm{m/s}$), it disappears immediately after we stop applying the SAW generation signal and before the SAW arrives at the target structure. Although this method allows for avoiding critical influence of the crosstalk, it severely limits the timing of SAW generation and continuous generation of SAW is prohibited. This inflexibility is a clear disadvantage for various applications. For example, in electron-quantum optics, it makes it difficult to scale up the system, where many single electrons are transferred by SAWs at different timings. In this study, we investigate the way not to avoid the crosstalk but to suppress it by devising the SAW generation method. With the developed method we have succeeded in radically reducing the electromagnetic crosstalk.

5.2 Concept of differential excite

SAWs are generated by using comb-shaped electrodes called an IDT on a piezoelectric substrate. Top part of Fig. 5.1a shows a typical scheme to generate SAWs, where one pad of the IDT is grounded while the other is excited by an ac voltage. In this study,

this scheme is called a single excitation. Here, IDTs with a double-finger pattern are employed. This type of IDT is often employed because it suppresses reflections of SAWs inside the IDT and improves conduction efficiency. When we apply an ac voltage whose frequency corresponds to the resonance frequency, f_{SAW}, determined by the period of the IDT fingers, λ, and the SAW velocity of the substrate, v_{SAW}, as $f_{\mathrm{SAW}} = v_{\mathrm{SAW}}/\lambda$ on the IDT, SAWs generated from each finger constructively interfere and strong SAWs propagate along the substrate towards the both directions. In this process, electromagnetic waves with the same frequency, f_{SAW}, are emitted from the metal pad where the excitation voltage is applied. In this study, we perform a differential excitation of the IDT as shown in the bottom part of Fig. 5.1a to suppress the radiation of the electromagnetic waves. In the differential excitation, the resonant ac voltage is applied to the both metal pads with a same amplitude but a phase shift of π between one to the other. Since the shape of the applied ac field is same for the differential excitation and the single excitation as depicted in Fig. 5.1a, SAWs are generated as in the case of the single excitation. Different from the single excitation, electromagnetic waves are emitted from the both pads. These electromagnetic waves have a phase difference of π and the amplitude is expected to be equal if the shapes of the metal pads are symmetrical. Since the wavelength of the electromagnetic waves, which is about 100 mm for $f_{\mathrm{SAW}} = 3\,\mathrm{GHz}$, are about 100 times longer than the scale of the IDT, which is typically less than 1 mm for the IDT with a resonant frequency in the GHz range, the two electromagnetic waves are expected to destructively interfere. As a result, the electromagnetic wave radiated from the IDT should be strongly suppressed.

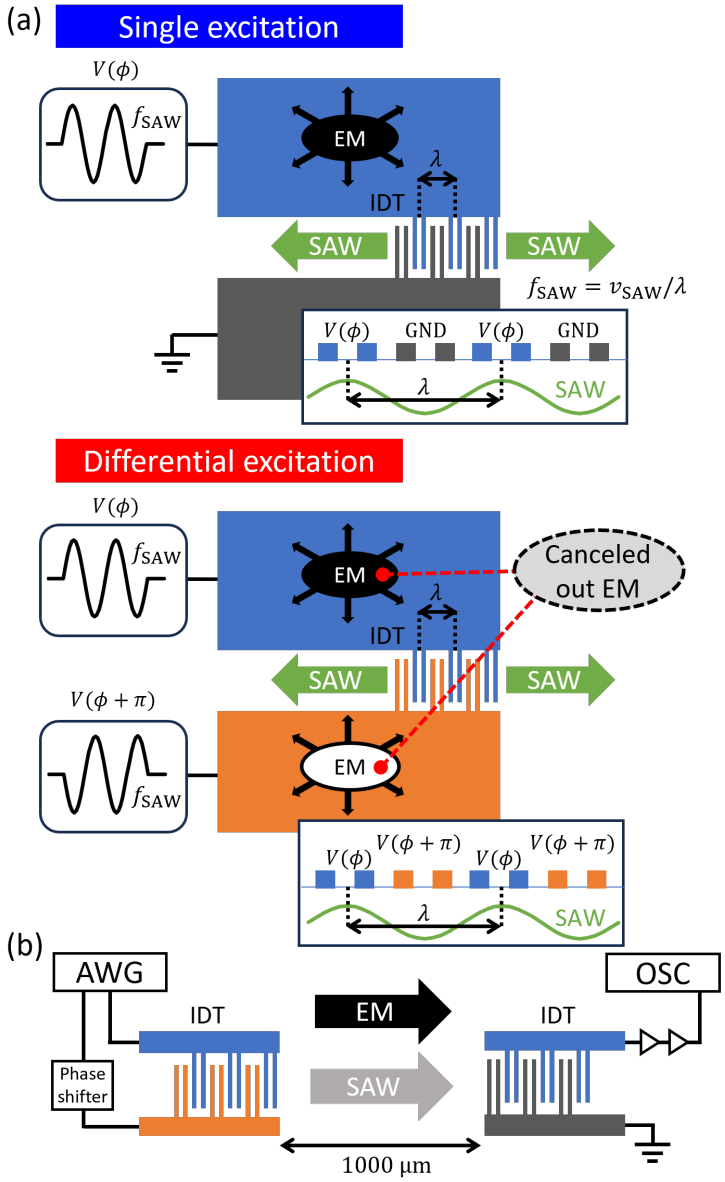

Figure 5.1: **(a)** Schematic diagram of the excitation method. Top: single excitation, bottom: differential excitation. The SAW generation signal $V(\phi)$ is input into the pads connecting to the comb-like electrodes of the IDT, and the SAWs and electromagnetic waves (EM) are generated. In the case of the single excitation, the electromagnetic wave originated from $V(\phi)$ is emitted from the high-frequency circuit such as metal pads. In the case of the differential excitation, the two types of electromagnetic waves originated from $V(\phi)$ and $V(\phi+\pi)$ destructively interfere with each other and cancel out. **(b)** Schematic diagram of the experimental setup and the device for the differential excitation.

5.3 Simulation of destructive interference

A simple simulation is performed to estimate the expected cancellation effect of electromagnetic waves due to the differential excitation. In this simulation, waves of the same frequency emitted from two different center points are modeled as electromagnetic waves and their interference with each other is calculated. Each center point is assumed to be the center of the metal pads to which the resonant ac voltage is applied. In our sample design, spacing of the two metal pads are $110\,\mu\mathrm{m}$. The waves emitted from both center points have a frequency of $1\,\mathrm{GHz}$, an equal amplitude of 1, and a velocity of $3 \times 10^8\,\mathrm{m/s}$. The phase of the wave from center point A is set to 0 and the one from center point B is set to π. This produces waves in perfectly opposite phases. These waves are calculated on a $1\,\mathrm{m}$ square two-dimensional plane so that the interference pattern could be easily checked. The circular waves are calculated taking into account the phase difference that depends on the distance from the center, and the amplitude is set to a constant value independent of distance. Fig. 5.2 shows the respective electromagnetic waves (Wave A and Wave B) in the top panels and the interference pattern resulting from the synthesis of both waves (Combined Wave) in the lower panels. In the lower left panel, the amplitude range of Combined Wave is set from -1 to 1, and the cancellation effect of the combined electromagnetic wave can be clearly observed. In the lower right panel, the amplitude range is set from -0.01 to 0.01 in order to confirm the detailed interference pattern. From this result, the cancellation effect of the electromagnetic waves is estimated to be over 99 %. The reason why a considerable suppression is estimated after taking into account the phase shift due to the difference in emission position of the two electromagnetic waves

is that the difference in emission position (110 µm) is small enough for the wavelength of the 1 GHz electromagnetic wave (300 mm). Similar results are also obtained at other frequencies commonly used for SAW generation signals (3 GHz - 4 GHz).

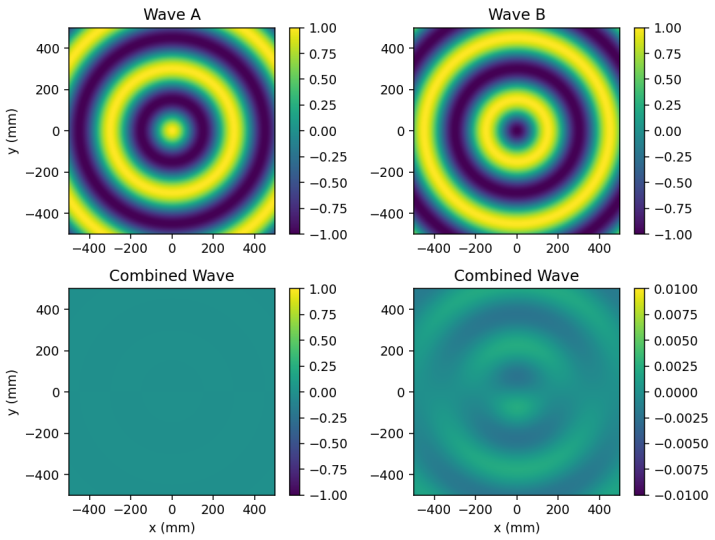

Figure 5.2: Two-dimensional simulation results of the cancellation effect due to the interference between two circular waves with opposite phases: Wave A and Wave B. The wave centers correspond to metal pads 110 µm apart on our device, where a resonant ac voltage is applied to excite SAWs. Top left: Wave A - a frequency 1 GHz, a phase 0, a velocity 3×10^8 m/s, from point A (0 µm,55 µm). Top right: Wave B - a frequency 1 GHz, a phase π, a velocity 3×10^8 m/s, from point B (0 µm,-55 µm). Lower left: Combined Wave - interference pattern resulting from the combination of Wave A and Wave B, showing the cancelation effect. Lower right: Combined Wave (Detailed View) - Detailed interference pattern with a narrowed amplitude range.

5.4 Expelimental setup

Next, we perform measurement of the device with a semi-automatic probe station at room temperature. The device is fabricated on a GaAs substrate and consists of IDTs and metal pads connected to the IDTs. The electrodes of the IDTs are fabricated using a standard electron-beam lithography with successive thin-film evaporation (metalization Ti 3 nm, Al 27 nm). The metal pads are fabricated using a standard photolithography

with successive thin-film evaporation (metalization Ti 20 nm, Au 100 nm). Two IDTs of the same design are placed facing each other in the direction of SAW propagation, at a distance of 1 mm, as shown in Fig. 5.1b. One IDT acts as a SAW generator and the other as a SAW detector. The both IDTs are designed to generate and detect SAWs at a resonant frequency of 1 GHz (λ =2.86 µm) and have 40 pairs of electrodes , an aperture of 30 µm. The SAW propagation direction is set to [110] direction. Contact metal pads (330 µm length and 60 µm width) are connected to the upper- and the lower-electrode sets of each IDT. High-frequency probes make contact with these pads, thus establishing a connection to the IDTs. These pads also act as a detector of electromagnetic waves. The resonant ac voltage to excite SAWs is provided by an AWG (Keysight M8195A) and fed through different coaxial cables to the upper and lower electrodes of the IDT, respectively, in the case of differential excitation. A phase shifter (WAKA 02X0442-00) is connected to one of the input lines for fine phase difference adjustment before the signal is input to the IDT. The phase shifter is adjusted and fixed so that there is minimal phase displacement at the probe when the same ac voltage is output from two channels of AWG. On the detector side, the set of lower electrodes is grounded (embedded in the surrounding ground pad). The set of upper electrodes is connected to a high-speed sampling oscilloscope (Keysight N1094B DCA-M) to observe the generated SAW and the electromagnetic wave. The detected signal is amplified by a series of broadband amplifiers (SHF S126A, ZHL-4W-422+).

5.5 Suppression of the electromagnetic waves

SAWs and electromagnetic waves are generated and observed with the single and differential excitation. To generate SAWs, we apply a sinusoidal signal at the resonance frequency, 1 GHz, with a time span of 60 ns and a peak-to-peak amplitude of 350 mV in a repetition period of 1520 ns. Here the time span of the signal, 60 ns, is chosen to be longer than 40 ns which is the minimum length to fully excite the IDT and to be shorter than the propagation time of SAWs between the IDTs, ~ 350 ns which is calculated from the distance between the IDTs (1 mm) and the SAW speed in GaAs ($\sim 2.81\,\mu\mathrm{m/ns}$). Since the electromagnetic waves emitted from the IDT propagate with the speed of light ($\sim 3 \times 10^8\,\mathrm{m/s}$), they reach the other detector IDT almost instantaneously in less than 10 ps. Therefore, when we perform a real-time detection of the signal at the detector IDT, we first observe the electromagnetic waves and later observe the SAW signal with a well-defined separation in the repetition period of 1520 ns. Here we apply the signal with the same amplitude for both the single and the differential excitation and hence the detected SAW signal is expected to be double for the differential excitation compared to the single. To compare the ratio between the amplitude of the SAW signal and the electromagnetic waves for both excitation methods we double the detected signal for the single excitation . Fig. 5.3 shows the signal measured with the sampling oscilloscope. The blue line is the data obtained when we perform the single excitation. The signal observed in the earlier time comes from electromagnetic waves and the one observed in approximately 350 ns later comes from SAWs. For the single excitation, the signal coming from electromagnetic waves is as large as the one coming from SAWs. The red line shows the data

obtained when we perform the differential excitation. The signal coming from SAWs

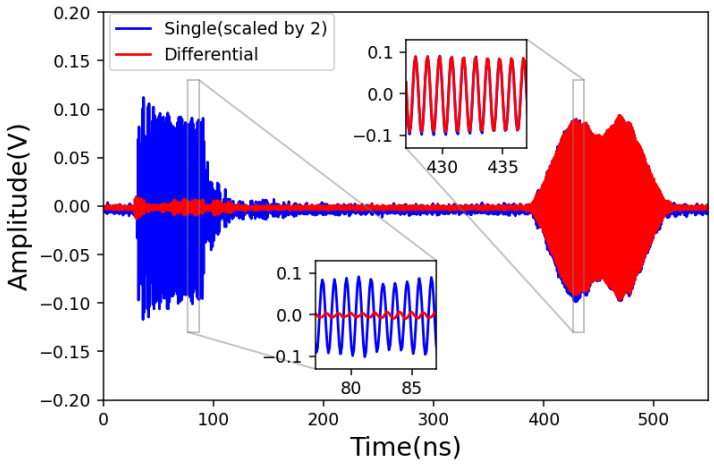

Figure 5.3: Time-resolved measurements on the IDT with the single excitation and the differential excitation. Trace of the detector response for the resonant ac voltage(1 GHz, a time span 60 ns, a peak-to-peak amplitude 350 mV). The blue line represents the SAW and the electromagnetic wave signals obtained from the single excitation, with the SAW on the right and the previously detected electromagnetic wave on the left. The red line represents the obtained signal from the differential excitation, where the SAW amplitude is similar to the single excitation while the electromagnetic component is significantly suppressed

.

is as large as the one from the single excitation. On the other hand, the signal coming from electromagnetic waves is strongly suppressed as expected from our simple simulation. Comparing the average values of the signal amplitude coming from electromagnetic waves from the single and the differential excitation, it is calculated that 92.4 % of the signal is suppressed for the case of the differential excitation. In our simple simulation, the electromagnetic-wave suppression of about 99 % is expected. The residual amount of the electromagnetic waves can be attributed to minute discrepancies between the two emitted electromagnetic waves due to the difference of response functions of the metal pads. These discrepancies manifested as time-dependence components that exhibited different phases and intensities and could not be addressed by simple adjustments of the phase or the amplitude of the SAW generation signal. Such fluctuations are considered

to be intricately related to high-frequency circuit components like a shape or a thickness of the metal pads. It suggests that optimization of these components is essential for even better suppression of the electromagnetic waves.

5.6 Spatial dependence of electromagnetic-wave suppression

Finally, we experimentally confirm the spatial dependence of the electromagnetic-wave suppression. For that purpose, we prepared the other device illustrated in the schematic in the middle of Fig. 5.4. On the left side, an IDT and metal pads having the same design as the device measured in Fig. 5.3 are placed. On the right side, multiple metal pads (220 µm in length and 60 µm in width) are arranged to pick up and detect electromagnetic waves. They are symmetrically arranged about the horizontal line passing through the middle of the IDT. The signal used to generate SAWs is the same as in Fig. 5.3. Each plot in Fig. 5.4 shows the signal coming from electromagnetic waves detected by the individual metal pads for the case of the single and the differential excitation. The change of the amplitude of the electromagnetic waves from the results in Fig. 3 can be attributed to the different sizes of the metal pads for detection. From these results, it is confirmed that the electromagnetic-wave suppression occurs similarly at all positions of the metal pads.

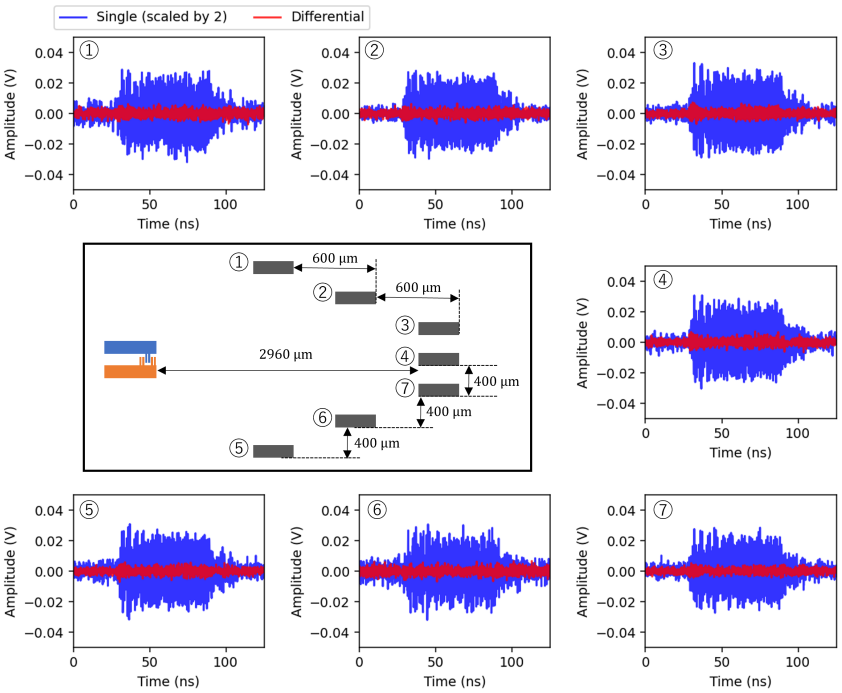

Figure 5.4: Spatial dependence of electromagnetic-wave suppression. A schematic of the sample is shown in the middle. Surrounding plots are electromagnetic waves detected on each metal pad with the single and the differential excitation. The numbers of the metal pads in the schematic correspond to the numbers of the plots. The suppression effect is almost same for all positions. The change in the amplitude of the electromagnetic waves from the results in Fig. 5.3 can be attributed to the different design of the metal pads for detection.

5.7 Conclusion

In conclusion, our study demonstrates the effectiveness of the differential excitation in mitigating electromagnetic crosstalk in SAW-based devices. The experimental results have shown that this approach is capable of nullifying over 90 % of the undesirable electromagnetic components, achieving a substantial reduction. This suppression of the electromagnetic crosstalk will certainly contribute to the improvement of the accuracy to control single flying electrons using SAW potentials [KFB$^+$06]. Furthermore, the spatial dependence of the electromagnetic wave cancellation effect has also been investigated. Consistent reduction in electromagnetic waves has been evident at all measured positions. This consistency is important for the scalability of SAW-based devices. In addition, although our experiments have been conducted at room temperature, we anticipate that the principles of the electromagnetic-wave suppression with the differential excitation are equally applicable in low-temperature environments. The electromagnetic-wave suppression has been investigated with a double-finger IDT in this study. However, it will be equally applicable to various types of IDTs [Mor07, LASS03, SZA$^+$15, EAR$^+$17, DSP$^+$19]. Our research focuses on fundamentally suppressing the electromagnetic crosstalk that has long hindered advancements of SAW-based single-electron control devices. The methodologies and insights obtained in this study are expected to significantly improve the scalability of SAW-based single-electron manipulation devices and make important contributions to the evolution of sophisticated SAW quantum information processing devices.

Chapter 6

Conclusion and perspectives

In conclusion, this work has made a contribution to the advancement of SAW-driven single electron transport technology, which is one of the approaches to the fundamental components of the rapidly growing field of quantum information processing. First, we investigated the material selection of IDTs and optimized the SAW generation technique. We enhanced the SAW generation intensity and generated SAWs with stronger confinement effect. This allows us to achieve position-specific single-electron transport, which is an important development in the stability and precision of SAW-driven electron transport [EWO$^+$21]. Thus, for the first time, the timing of single-electron transport in SAWs can be precisely controlled. This is an extremely important result that will serve as the basis for future experiments on single-electron transport in SAWs. As a result, electron collision experiments with two synchronized single-electron sources have recently been demonstrated in a SAW system [WER$^+$23]. Another optimization of the SAW generation technique was the development of a single-pulse SAW generation technique that minimizes unwanted effects on the system. Due in part to the optimization of SAW gen-

eration intensity, highly efficient transport of single electrons between distant quantum dots using this pulsed SAW has also been demonstrated [WOE$^+$22], and this technology could become a standard for future SAW electron transport. This pulsed SAW technique greatly expands the degree of freedom of single-electron transport and control, and opens up new possibilities for experiments that have been performed with conventional SAWs. One example is the combination of a pulsed SAW and a quantum wire, which leads to the development of on-demand single-electron sources [OWE$^+$24]. The system which can be implemented with a simple structure and operation brings advantages in scaling up SAW-based experimental systems and opens new avenues for synchronization of multiple single-electron sources. Furthermore, we have essentially solved the electromagnetic wave crosstalk problem, which was once again revealed to have a significant impact on electron transport. Our proposed differential excitation of IDTs is demonstrated to be effective in suppressing electromagnetic wave generation [OON$^+$24]. This suppression is essential for the realization of multiple single electron transport by SAWs and underscores the practicality of our efforts to enhance the scalability of the system for application to quantum information processing devices.

These our work are important advances toward the development of quantum information processing devices that utilize the charge or spin of electrons. In particular, they are directly important in the direction of realizing quantum computers based on SAW-based flying qubit architectures that utilize charge of electron, as we have already mentioned. Other systems that realize electron flying qubit architectures are Leviton [DJP$^+$13, EWC$^+$22] and hot electron [KJE$^+$16b], but these systems do not yet have detectors or are still in the process of being tested for their suitability for quantum in-

formation processing applications. SAWs already have the basic tools, such as a single electron source and a single electron detector, and the results of this thesis enabled the research toward the realization of two-qubit gates. On the other hand, in the direction of realizing a quantum computer based on a qubit architecture using spin of electron, the expected application of the SAW driven electron transport technology is the long-range spin qubit connection required for coupling between qubit clusters, which is essential for realizing large-scale qubit integration. Other systems for long-range connection of spin qubits are circuit-quantum electrodynamics (QED) and quantum dot array. Circuit-QED has a fast transport velocity, but coherent transport of spins of electrons has not yet been demonstrated. In addition, the advantage of transport velocity is not effective for sub-mm transport because it requires several hundred ns for information conversion before and after the transport [MBP+18]. Coherent transport has been reported using tunneling between quantum dots [FMT+17, FBR+17], but this method requires a large number of quantum dots to be connected in proportion to the transport distance, and is currently limited to transport between adjacent quantum dots (0.5 µm). Nevertheless, quantum dot arrays are consistent with integration of quantum dots, and methods to generate dynamic potentials by driving quantum dot arrays with multiple voltage inputs have been developed in recent years [LKF+23]. On the other hand, a method using SAWs has been shown to transport electrons and their spins coherently and efficiently over 6 µm in GaAs [BHT+16, JMC+21], and it is thought that the method can be extended to several hundred µm [SHSP05]. Furthermore, the transport is 30-40 times faster than that using quantum dot array, making SAWs a promising technology for transporting spins of electrons within the same substrate. However, the current research on quantum bits using electron spins is

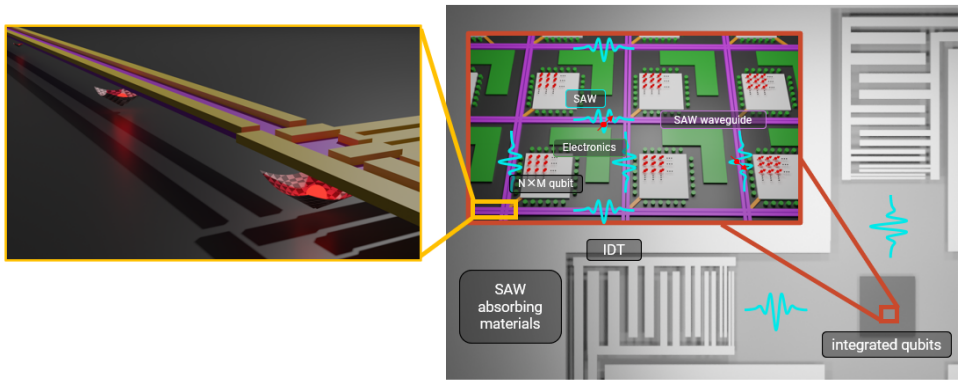

Figure 6.1: Proposed example implementation of spin qubit integration including SAW-based long-range coupling.

dominated by materials such as Si and Ge, not GaAs. Si and Ge do not have the piezoelectric properties required for SAW generation, so the SAW technique cannot be applied without modification. Piezoelectric properties can be introduced to non-piezoelectric substrates by layering thin films of piezoelectric materials such as ZnO and LiN, which have high piezoelectric effect, on the substrate surface. By such means, we believe that SAW-driven single electron transport technology can be introduced to these promising systems as spin qubits. From this perspective, the findings and techniques developed in this study for GaAs can be fully utilized in other systems. Possible obstacles include the complexity of the fabrication process for piezoelectric thin film layering and the need to leave a surface for the generation and propagation of SAWs. However, since these obstacles need to be considered only on the transport path by SAWs, the constraints are expected to be minimal. With this in mind, a proposed example implementation of spin qubit integration that includes SAW-based long-range coupling is shown in Fig. 6.1. Here, a cluster of N × M qubits and local electronics for controlling these bits as well as SAW waveguides are set up. The local electronics include ADC and DAC converters and vector modulation, minimizing the number of control lines needed to control the entire integrated qubit; the

SAW waveguide serves as a quantum information transfer path between each cluster, and the transport of electrons from the cluster to the transfer state by the SAW is done by the quantum bit array is envisioned. The IDTs for generating SAWs can be located outside of the integrated qubits, preventing the complexity of the integrated structure. The fast quantum information transport rate of the SAWs allows such an architecture to achieve maximum scalability compared to other methods in the range of qubit coherence times.

Finally, we highlight that some method, as those demonstrated, is not restricted only to single-electron transport. We anticipate applications of the chirp technique in hybrid-nanomechanical [MSF18], superconducting [YFK$^+$20] and spintronics [KYM$^+$17, YSR$^+$20] devices. For the latter in particular, short SAW pulses will enable time-resolved measurements of magnetization and domain wall displacement and will thus allow to replace optical techniques by sound [CGL$^+$21]. Moreover, the differential excitation of IDTs provides a new perspective for addressing the problem of electromagnetic crosstalk in SAW-based systems and opens up the possibility of application of SAWs in various fields of research such as spintronics and quantum acoustics.

Appendix

In the main text, the differences between the surface acoustic wave (SAW) pulses developed in Chapter 2 and conventional SAWs are described, but minor differences at the laboratory level were also observed. The following experiment is particularly interesting in terms of the relationship between the shape of the SAW and the transported single electron, as well as the behavior of the single electron during the transport process. This is an experiment in which we checked and conditioned the performance of receiver quantum dots (QDs) that capture electrons transported by SAWs. These experiments are performed as a preliminary preparation for single electron transport experiments between QDs by SAWs. To check the ability of the receiver QD to hold electrons, we prepared a single electron in the receiver QD and used charge sensors fabricated nearby to check whether the electron remained held even after the SAW passed through at various potentials. Fig. 1 shows one of the results, using our developed SAW pulse. The deep green indicates regions where electrons remained retained, and the bright green indicates regions where electrons were not retained. This kind of experiment has been performed in previous experiments using conventional SAWs, but in the case of this SAW pulse, the following phenomena, which had not been seen before, were observed even though the SAW intensity was the same and the device design was the same. When the negative

voltage applied to rqr is high, i.e., when the potential between the QD and reservoir is high, electrons are not retained. Also, when the negative voltage applied to cer is low, i.e., when the potential between the QD and the quantum wire is low, electrons are not retained. Although the high and low here are only relative expressions, more stable electron retention capability than this has been confirmed with ordinary SAWs.

As a result of trial and error, though, we were able to stabilize electron retention by making the potential of the quantum wire even higher relative to the potential of the quantum wire. From here, it is possible that the SAW pulse caused electrons to flow out of the receiver QDs into the quantum wires. It is also possible that the falling edge of the normal SAW had the effect of allowing electrons to settle in the receiver QD. Based on these considerations, the optimization of the design around the receiver QDs and source QDs to match the shape of the surface acoustic wave, This may be one of the keys to further improve the accuracy of electron transport in the future.

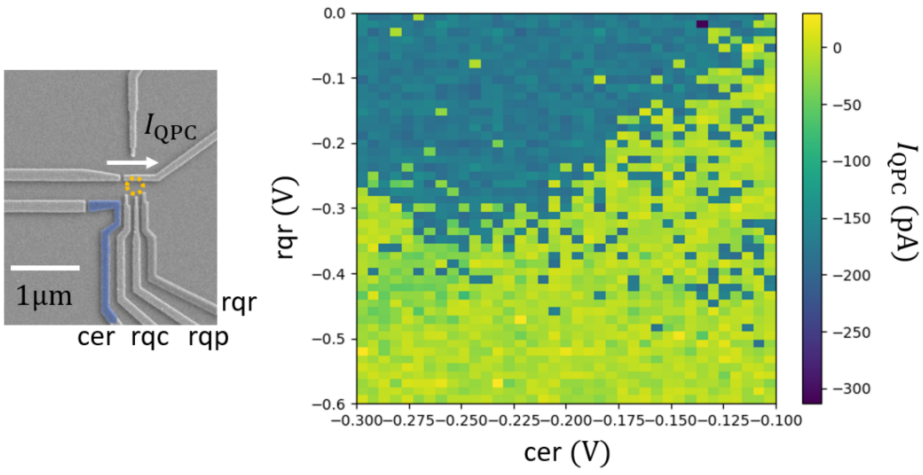

Figure 1: Electron holding performance of QDs.

Bibliography

[AAB+19] Frank Arute, Kunal Arya, Ryan Babbush, Dave Bacon, Joseph C. Bardin, Rami Barends, Rupak Biswas, Sergio Boixo, Fernando G. S. L. Brandao, David A. Buell, Brian Burkett, Yu Chen, Zijun Chen, Ben Chiaro, Roberto Collins, William Courtney, Andrew Dunsworth, Edward Farhi, Brooks Foxen, Austin Fowler, Craig Gidney, Marissa Giustina, Rob Graff, Keith Guerin, Steve Habegger, Matthew P. Harrigan, Michael J. Hartmann, Alan Ho, Markus Hoffmann, Trent Huang, Travis S. Humble, Sergei V. Isakov, Evan Jeffrey, Zhang Jiang, Dvir Kafri, Kostyantyn Kechedzhi, Julian Kelly, Paul V. Klimov, Sergey Knysh, Alexander Korotkov, Fedor Kostritsa, David Landhuis, Mike Lindmark, Erik Lucero, Dmitry Lyakh, Salvatore Mandrà, Jarrod R. McClean, Matthew McEwen, Anthony Megrant, Xiao Mi, Kristel Michielsen, Masoud Mohseni, Josh Mutus, Ofer Naaman, Matthew Neeley, Charles Neill, Murphy Yuezhen Niu, Eric Ostby, Andre Petukhov, John C. Platt, Chris Quintana, Eleanor G. Rieffel, Pedram Roushan, Nicholas C. Rubin, Daniel Sank, Kevin J. Satzinger, Vadim Smelyanskiy, Kevin J. Sung, Matthew D. Trevithick, Amit Vainsencher, Benjamin Villalonga, Theodore White, Z. Jamie Yao, Ping Yeh, Adam Zalcman, Hartmut Neven, and

John M. Martinis. Quantum supremacy using a programmable superconducting processor. *Nature*, 574(7779):505–510, 2019.

[ASG+19] Gustav Andersson, Baladitya Suri, Lingzhen Guo, Thomas Aref, and Per Delsing. Non-exponential decay of a giant artificial atom. *Nature Physics*, 15(11):1123–1127, 2019.

[ASLO+17] D. R. M. Arvidsson-Shukur, H. V. Lepage, E. T. Owen, T. Ferrus, and C. H. W. Barnes. Protocol for fermionic positive-operator-valued measures. *Physical Review A*, 96(5):052305, 2017.

[BBB+00] A. Bertoni, P. Bordone, R. Brunetti, C. Jacoboni, and S. Reggiani. Quantum Logic Gates based on Coherent Electron Transport in Quantum Wires. *Physical Review Letters*, 84(25):5912–5915, 2000.

[BCJ+00] H J Briegel, T Calarco, D Jaksch, J I Cirac, and P Zoller. Quantum computing with neutral atoms. *Journal of Modern Optics*, 47(2-3):415–451, 2 2000.

[Ben80] Paul Benioff. The computer as a physical system: A microscopic quantum mechanical Hamiltonian model of computers as represented by Turing machines. *Journal of Statistical Physics*, 22(5):563–591, 5 1980.

[BGM+18] Christopher Bäuerle, D Christian Glattli, Tristan Meunier, Fabien Portier, Patrice Roche, Preden Roulleau, Shintaro Takada, and Xavier Waintal. Coherent control of single electrons: a review of current progress. *Reports on Progress in Physics*, 81(5):056503, 2018.

[BHT+16] B. Bertrand, S. Hermelin, S. Takada, M. Yamamoto, S. Tarucha, A. Ludwig, A. D. Wieck, C. Bäuerle, and T. Meunier. Fast spin information transfer between distant quantum dots using individual electrons. *Nature Nanotechnology*, 11:672, 2016.

[BJSS72] T.W. Bristol, W.R. Jones, P.B. Snow, and W.R. Smith. Applications of Double Electrodes in Acoustic Surface Wave Device Design. *1972 Ultrasonics Symposium*, pages 343–345, 1972.

[BKL+07] M. D. Blumenthal, B. Kaestner, L. Li, S. Giblin, T. J. B. M. Janssen, M. Pepper, D. Anderson, G. Jones, and D. A. Ritchie. Gigahertz quantized charge pumping. *Nature Physics*, 3:343, 2007.

[BSR00] C. H. W. Barnes, J. M. Shilton, and A. M. Robinson. Quantum computation using electrons trapped by surface acoustic waves. *Physical Review B*, 62(12):8410–8419, 2000.

[BSZ+19] A. Bienfait, K. J. Satzinger, Y. P. Zhong, H.-S. Chang, M.-H. Chou, C. R. Conner, É. Dumur, J. Grebel, G. A. Peairs, R. G. Povey, and A. N. Cleland. Phonon-mediated quantum state transfer and remote qubit entanglement. *Science*, 364(6438):368–371, 2019.

[BZA+07] Stefan Birner, Tobias Zibold, Till Andlauer, Tillmann Kubis, Matthias Sabathil, Alex Trellakis, and Peter Vogl. nextnano: General Purpose 3-D Simulations. *IEEE Transactions on Electron Devices*, 54(9):2137–2142, 2007.

[BZK+18] Aleksey N. Bolgar, Julia I. Zotova, Daniil D. Kirichenko, Ilia S. Besedin, Aleksander V. Semenov, Rais S. Shaikhaidarov, and Oleg V. Astafiev. Quantum Regime of a Two-Dimensional Phonon Cavity. *Physical Review Letters*, 120(22):223603, 2018.

[CGL+21] Fa Chen, Xu Ge, Wei Luo, Renhao Xing, Shiheng Liang, Xiaofei Yang, Long You, Rui Xiong, Yoshichika Otani, and Yue Zhang. Strain-induced Megahertz Oscillation and Stable Velocity of an Antiferromagnetic Domain Wall. *Physical Review Applied*, 15(1):014030, 2021.

[CTS+99] J. Cunningham, V. I. Talyanskii, J. M. Shilton, M. Pepper, M. Y. Simmons, and D. A. Ritchie. Single-electron acoustic charge transport by two counterpropagating surface acoustic wave beams. *Physical Review B*, 60:4850, 1999.

[CTS+00] J. Cunningham, V. I. Talyanskii, J. M. Shilton, M. Pepper, A. Kristensen, and P. E. Lindelof. Single-electron acoustic charge transport on shallow-etched channels in a perpendicular magnetic field. *Physical Review B*, 62:1564, 2000.

[CZ95] J I Cirac and P Zoller. Quantum Computations with Cold Trapped Ions. *Physical Review Letters*, 74(20):4091–4094, 5 1995.

[DCS+19] P. Delsing, A. N. Cleland, M. J. A. Schuetz, J. Knörzer, G. Giedke, J. I. Cirac, K. Srinivasan, M. Wu, K. C. Balram, C. Bäuerle, T. Meunier, C. J. B. Ford, P. V. Santos, E. Cerda-Méndez, H. Wang, H. J. Krenner, E. D. S. Nysten, M. Weiß, G. R. Nash, L. Thevenard, C. Gourdon, P. Rovil-

lain, M. Marangolo, J.-Y. Duquesne, G. Fischerauer, W. Ruile, A. Reiner, B. Paschke, D. Denysenko, D. Volkmer, A. Wixforth, H. Bruus, M. Wiklund, J. Reboud, J. M. Cooper, Y. Fu, M. S. Brugger, F. Rehfeldt, and C. Westerhausen. The 2019 surface acoustic waves roadmap. *Journal of Physics D: Applied Physics*, 52:353001, 2019.

[DI00] David P DiVincenzo and IBM. The Physical Implementation of Quantum Computation. *Fortschritte der Physik*, 48(9-11):771–783, 2000.

[DJP+13] J. Dubois, T. Jullien, F. Portier, P. Roche, A. Cavanna, Y. Jin, W. Wegscheider, P. Roulleau, and D. C. Glattli. Minimal-excitation states for electron quantum optics using levitons. *Nature*, 502:659, 2013.

[DSP+19] É. Dumur, K. J. Satzinger, G. A. Peairs, Ming-Han Chou, A. Bienfait, H.-S. Chang, C. R. Conner, J. Grebel, R. G. Povey, Y. P. Zhong, and A. N. Cleland. Unidirectional distributed acoustic reflection transducers for quantum applications. *Applied Physics Letters*, 114(22):223501, 2019.

[EAR+17] Maria K. Ekström, Thomas Aref, Johan Runeson, Johan Björck, Isac Boström, and Per Delsing. Surface acoustic wave unidirectional transducers for quantum applications. *Applied Physics Letters*, 110(7):073105, 2017.

[EPA02] J. Ebbecke, K. Pierz, and F. Ahlers. Influence of the shape of a quasi-one-dimensional channel on the quantized acousto-electric current. *Physica E: Low-dimensional Systems and Nanostructures*, 12:466, 2002.

[EWC+22] Hermann Edlbauer, Junliang Wang, Thierry Crozes, Pierre Perrier, Seddik Ouacel, Clément Geffroy, Giorgos Georgiou, Eleni Chatzikyriakou, An-

tonio Lacerda-Santos, Xavier Waintal, D. Christian Glattli, Preden Roulleau, Jayshankar Nath, Masaya Kataoka, Janine Splettstoesser, Matteo Acciai, Maria Cecilia da Silva Figueira, Kemal Öztas, Alex Trellakis, Thomas Grange, Oleg M. Yevtushenko, Stefan Birner, and Christopher Bäuerle. Semiconductor-based electron flying qubits: review on recent progress accelerated by numerical modelling. *EPJ Quantum Technology*, 9(1):21, 2022.

[EWO+21] Hermann Edlbauer, Junliang Wang, Shunsuke Ota, Aymeric Richard, Baptiste Jadot, Pierre-André Mortemousque, Yuma Okazaki, Shuji Nakamura, Tetsuo Kodera, Nobu-Hisa Kaneko, Arne Ludwig, Andreas D. Wieck, Matias Urdampilleta, Tristan Meunier, Christopher Bäuerle, and Shintaro Takada. In-flight distribution of an electron within a surface acoustic wave. *Applied Physics Letters*, 119(11):114004, 2021.

[FBR+17] Takafumi Fujita, Timothy Alexander Baart, Christian Reichl, Werner Wegscheider, and Lieven Mark Koenraad Vandersypen. Coherent shuttle of electron-spin states. *npj Quantum Information*, 3(1):22, 2017.

[FMMC12] Austin G. Fowler, Matteo Mariantoni, John M. Martinis, and Andrew N. Cleland. Surface codes: Towards practical large-scale quantum computation. *Physical Review A*, 86(3):032324, 2012.

[FMT+17] H. Flentje, P.-A. Mortemousque, R. Thalineau, A. Ludwig, A. D. Wieck, C. Bäuerle, and T. Meunier. Coherent long-distance displacement of individual electron spins. *Nature Communications*, 8(1):501, 2017. the coherence of a two-electron singlet state is preserved when the electrons are

separated and displaced over 5μm around a closed loop in a three-dot system.

[For17] Christopher J. B. Ford. Transporting and manipulating single electrons in surface-acoustic-wave minima. *physica status solidi (b)*, 254(3):1600658, 2017.

[GAK+14] Martin V. Gustafsson, Thomas Aref, Anton Frisk Kockum, Maria K. Ekström, Göran Johansson, and Per Delsing. Propagating phonons coupled to an artificial atom. *Science*, 346(6206):207–211, 2014.

[GARC17] David B. Go, Massood Z. Atashbar, Zeinab Ramshani, and Hsueh-Chia Chang. Surface acoustic wave devices for chemical sensing and microfluidics: a review and perspective. *Analytical Methods*, 9(28):4112–4134, 2017.

[Gib17] Elizabeth Gibney. New definitions of scientific units are on the horizon. *Nature*, 550:312–313, 2017.

[HCR+18] H Hou, Y Chung, G Rughoobur, T K Hsiao, A Nasir, A J Flewitt, J P Griffiths, I Farrer, D A Ritchie, and C J B Ford. Experimental verification of electrostatic boundary conditions in gate-patterned quantum devices. *Journal of Physics D: Applied Physics*, 51(24):244004, 2018.

[HRC+20] T. K. Hsiao, A. Rubino, Y. Chung, S. K. Son, H. Hou, J. Pedrós, A. Nasir, G. Éthier Majcher, M. J. Stanley, R. T. Phillips, T. A. Mitchell, J. P. Griffiths, I. Farrer, D. A. Ritchie, and C. J. B. Ford. Single-photon emission from

single-electron transport in a saw-driven lateral light-emitting diode. *Nature Communications*, 11:917, 2020.

[HTY+11] S. Hermelin, S. Takada, M. Yamamoto, S. Tarucha, A. D. Wieck, L. Saminadayar, C. Bäuerle, and T. Meunier. Electrons surfing on a sound wave as a platform for quantum optics with flying electrons. *Nature*, 477:435, 2011.

[IEE] IEEE Future Networks Technology Roadmap Working Group 2017 IEEE 5G and beyond technology roadmap white paper.

[ITL+21] R. Ito, S. Takada, A. Ludwig, A. D. Wieck, S. Tarucha, and M. Yamamoto. Coherent beam splitting of flying electrons driven by a surface acoustic wave. *Physical Review Letters*, 126:070501, 2021.

[IY88] K Igeta and Y Yamamoto. Quantum mechanical computers with single atom and photon fields. In *International Conference on Quantum Electronics, Paper TuI4. Optica Publishing Group: TuI4.*, 1988.

[JMC+21] B. Jadot, P.-A. Mortemousque, E. Chanrion, V. Thiney, A. Ludwig, A. D. Wieck, M. Urdampilleta, C. Bäuerle, and T. Meunier. Distant spin entanglement via fast and coherent electron shuttling. *Nature Nanotechnology*, 16:570, 2021.

[KFB+06] M. Kataoka, C. J. B. Ford, C. H. W. Barnes, D. Anderson, G. A. C. Jones, H. E. Beere, D. A. Ritchie, and M. Pepper. The effect of pulse-modulated surface acoustic waves on acoustoelectric current quantization. *Journal of Applied Physics*, 100:063710, 2006.

[KJE+16a] M. Kataoka, N. Johnson, C. Emary, P. See, J. P. Griffiths, G. A. C. Jones, I. Farrer, D. A. Ritchie, M. Pepper, and T. J. B. M. Janssen. Time-of-Flight Measurements of Single-Electron Wave Packets in Quantum Hall Edge States. *Physical Review Letters*, 116(12):126803, 2016.

[KJE+16b] M. Kataoka, N. Johnson, C. Emary, P. See, J. P. Griffiths, G. A. C. Jones, I. Farrer, D. A. Ritchie, M. Pepper, and T. J. B. M. Janssen. Time-of-Flight Measurements of Single-Electron Wave Packets in Quantum Hall Edge States. *Physical Review Letters*, 116(12):126803, 2016.

[KKH+14] H. Kamata, N. Kumada, M. Hashisaka, K. Muraki, and T. Fujisawa. Fractionalized wave packets from an artificial Tomonaga–Luttinger liquid. *Nature Nanotechnology*, 9(3):177–181, 2014.

[KLM01] E. Knill, R. Laflamme, and G. J. Milburn. A scheme for efficient quantum computation with linear optics. *Nature*, 409(6816):46–52, 2001.

[KMN+07] Pieter Kok, W. J. Munro, Kae Nemoto, T. C. Ralph, Jonathan P. Dowling, and G. J. Milburn. Linear optical quantum computing with photonic qubits. *Reviews of Modern Physics*, 79(1):135–174, 2007.

[KMZS96] M. W. Keller, J. M. Martinis, N. M. Zimmerman, and A. H. Steinbach. Accuracy of electron counting using a 7-junction electron pump. *Applied Physics Letters*, 69:1804, 1996.

[KYM+17] D. Kobayashi, T. Yoshikawa, M. Matsuo, R. Iguchi, S. Maekawa, E. Saitoh, and Y. Nozaki. Spin Current Generation Using a Surface Acoustic

Wave Generated via Spin-Rotation Coupling. *Physical Review Letters*, 119(7):077202, 2017.

[LASS03] M. M. de Lima, F. Alsina, W. Seidel, and P. V. Santos. Focusing of surface-acoustic-wave fields on (100) GaAs surfaces. *Journal of Applied Physics*, 94(12):7848–7855, 2003.

[LD98] Daniel Loss and David P DiVincenzo. Quantum computation with quantum dots. *Physical Review A*, 57(1):120–126, 1 1998.

[LKF+23] Veit Langrock, Jan A. Krzywda, Niels Focke, Inga Seidler, Lars R. Schreiber, and Łukasz Cywiński. Blueprint of a Scalable Spin Qubit Shuttle Device for Coherent Mid-Range Qubit Transfer in Disordered Si/SiGe/SiO2. *PRX Quantum*, 4(2):020305, 2023. shift resist(Okazaki-san comment).

[LLASB20] Hugo V. Lepage, Aleksander A. Lasek, David R. M. Arvidsson-Shukur, and Crispin H. W. Barnes. Entanglement generation via power-of-swap operations between dynamic electron-spin qubits. *Physical Review A*, 101(2):022329, 2020.

[Lod17] Peter Lodahl. Quantum-dot based photonic quantum networks. *Quantum Science and Technology*, 3(1):013001, 2017.

[MBP+18] X. Mi, M. Benito, S. Putz, D. M. Zajac, J. M. Taylor, Guido Burkard, and J. R. Petta. A coherent spin–photon interface in silicon. *Nature*, 555(7698):599–603, 2018.

[MKF+11] R. P. G. McNeil, M. Kataoka, C. J. B. Ford, C. H. W. Barnes, D. Anderson, G. A. C. Jones, I. Farrer, and D. A. Ritchie. On-demand single-electron transfer between distant quantum dots. *Nature*, 477:439, 2011.

[MKP+17] Riccardo Manenti, Anton F. Kockum, Andrew Patterson, Tanja Behrle, Joseph Rahamim, Giovanna Tancredi, Franco Nori, and Peter J. Leek. Circuit quantum acoustodynamics with surface acoustic waves. *Nature Communications*, 8(1):975, 2017.

[Mor07] David Morgan. *Surface acoustic wave filters: with applications to electronic communications and signal processing. 2nd ed.* Oxford: Academic Press, 2007.

[MR14] Tal Mor and Renato Renner. Preface. *Natural Computing*, 13(4):447–452, 12 2014.

[MSF18] Leonardo Midolo, Albert Schliesser, and Andrea Fiore. Nano-opto-electro-mechanical systems. *Nature Nanotechnology*, 13(1):11–18, 2018.

[MSVL18] Bradley A. Moores, Lucas R. Sletten, Jeremie J. Viennot, and K. W. Lehnert. Cavity Quantum Acoustic Device in the Multimode Strong Coupling Regime. *Physical Review Letters*, 120(22):227701, 2018.

[NOT] Junliang-wang/idtpy: First release, https://doi.org/10.5281/zenodo.6107277, 2022.

[NPT99] Y. Nakamura, Yu. A. Pashkin, and J. S. Tsai. Coherent control of macro-

scopic quantum states in a single-Cooper-pair box. *Nature*, 398(6730):786–788, 4 1999.

[NRK20] Emeline D. S. Nysten, Armando Rastelli, and Hubert J. Krenner. A hybrid (Al)GaAs-LiNbO3 surface acoustic wave resonator for cavity quantum dot optomechanics. *Applied Physics Letters*, 117(12):121106, 2020.

[NYTN17] Atsushi Noguchi, Rekishu Yamazaki, Yutaka Tabuchi, and Yasunobu Nakamura. Qubit-Assisted Transduction for a Detection of Surface Acoustic Waves near the Quantum Limit. *Physical Review Letters*, 119(18):180505, 2017.

[OON+24] Shunsuke Ota, Yuma Okazaki, Shuji Nakamura, Takehiko Oe, Hermann Sellier, Christopher Bäuerle, Nobu-Hisa Kaneko, Tetsuo Kodera, and Shintaro Takada. Suppression of electromagnetic crosstalk by differential excitation for SAW generation. *Applied Physics Express*, 17(2):022002, 2024.

[OWE+24] Shunsuke Ota, Junliang Wang, Hermann Edlbauer, Yuma Okazaki, Shuji Nakamura, Takehiko Oe, Arne Ludwig, Andreas D. Wieck, Hermann Sellier, Christopher Bäuerle, Nobu-Hisa Kaneko, Tetsuo Kodera, and Shintaro Takada. On-demand single-electron source via single-cycle acoustic pulses. *Physical Review Applied*, 21(2):024034, 2024.

[PMS+14] Alberto Peruzzo, Jarrod McClean, Peter Shadbolt, Man-Hong Yung, Xiao-Qi Zhou, Peter J. Love, Alán Aspuru-Guzik, and Jeremy L. O'Brien. A variational eigenvalue solver on a photonic quantum processor. *Nature Communications*, 5(1):4213, 2014.

[PUL03] J. B. Hansen P. Utko, K. Gloos and P. E. Lindelof. An Improved 2.5 GHz Electron Pump: Single-Electron Transport through Shallow-Etched Point Contac ts Driven by Surface Acoustic Waves. *Acta Phys. Pol. A*, 103:533, 2003.

[QDA+23] H. Qiao, É. Dumur, G. Andersson, H. Yan, M.-H. Chou, J. Grebel, C. R. Conner, Y. J. Joshi, J. M. Miller, R. G. Povey, X. Wu, and A. N. Cleland. Splitting phonons: Building a platform for linear mechanical quantum computing. *Science*, 380(6649):1030–1033, 2023.

[RAG+18] Gregoire Roussely, Everton Arrighi, Giorgos Georgiou, Shintaro Takada, Martin Schalk, Matias Urdampilleta, Arne Ludwig, Andreas D. Wieck, Pacome Armagnat, Thomas Kloss, Xavier Waintal, Tristan Meunier, and Christopher Bäuerle. Unveiling the bosonic nature of an ultrashort few-electron pulse. *Nature Communications*, 9(1):2811, 2018.

[Ray85] Lord Rayleigh. On Waves Propagated along the Plane Surface of an Elastic Solid. *Proceedings of the London Mathematical Society*, s1-17(1):4–11, 1885.

[SDF+15] F. Stein, D. Drung, L. Fricke, H. Scherer, F. Hohls, C. Leicht, M. Götz, C. Krause, R. Behr, E. Pesel, K. Pierz, U. Siegner, F. J. Ahlers, and H. W. Schumacher. Validation of a quantized-current source with 0.2 ppm uncertainty. *Applied Physics Letters*, 107:103501, 2015.

[SHH04] G. Sukhodub, F. Hohls, and R. J. Haug. Observation of an Interedge Magne-

toplasmon Mode in a Degenerate Two-Dimensional Electron Gas. *Physical Review Letters*, 93(19):196801, 2004.

[Sho94] P.W. Shor. Algorithms for quantum computation: discrete logarithms and factoring. *Proceedings 35th Annual Symposium on Foundations of Computer Science*, pages 124–134, 1994.

[SHSP05] J. A. H. Stotz, R. Hey, P. V. Santos, and K. H. Ploog. Coherent spin transport through dynamic quantum dots. *Nature Materials*, 4:585, 2005.

[SKF+06] R J Schneble, M Kataoka, C J B Ford, C H W Barnes, D Anderson, G A C Jones, I Farrer, D A Ritchie, and M Pepper. Quantum-dot thermometry of electron heating by surface acoustic waves. *Applied Physics Letters*, 89(12):122104, 9 2006.

[SKG+17] M. J. A. Schuetz, J. Knörzer, G. Giedke, L. M. K. Vandersypen, M. D. Lukin, and J. I. Cirac. Acoustic Traps and Lattices for Electrons in Semiconductors. *Physical Review X*, 7(4):041019, 2017.

[SMT+96] J. M. Shilton, D. R. Mace, V. I. Talyanskii, Y. Galperin, M. Y. Simmons, M. Pepper, and D. A. Ritchie. On the acoustoelectric current in a one-dimensional channel. *Journal of Physics: Condensed Matter*, 8:L337, 1996.

[SSX+22] I. Seidler, T. Struck, R. Xue, N. Focke, S. Trellenkamp, H. Bluhm, and L. R. Schreiber. Conveyor-mode single-electron shuttling in si/sige for a scalable quantum computing architecture. *npj Quantum Information*, 8:100, 2022.

[SZA+15] Florian J. R. Schülein, Eugenio Zallo, Paola Atkinson, Oliver G. Schmidt,

Rinaldo Trotta, Armando Rastelli, Achim Wixforth, and Hubert J. Krenner. Fourier synthesis of radiofrequency nanomechanical pulses with different shapes. *Nature Nanotechnology*, 10(6):512–516, 2015.

[SZC+18] K. J. Satzinger, Y. P. Zhong, H.-S. Chang, G. A. Peairs, A. Bienfait, Ming-Han Chou, A. Y. Cleland, C. R. Conner, É. Dumur, J. Grebel, I. Gutierrez, B. H. November, R. G. Povey, S. J. Whiteley, D. D. Awschalom, D. I. Schuster, and A. N. Cleland. Quantum control of surface acoustic-wave phonons. *Nature*, 563(7733):661–665, 2018.

[TEL+19] S. Takada, H. Edlbauer, H. V. Lepage, J. Wang, P.-A. Mortemousque, G. Georgiou, C. H. W. Barnes, C. J. B. Ford, M. Yuan, P. V. Santos, X. Waintal, A. Ludwig, A. D. Wieck, M. Urdampilleta, T. Meunier, and C. Bäuerle. Sound-driven single-electron transfer in a circuit of coupled quantum rails. *Nature Communications*, 10:4557, 2019.

[TSP+97] V. I. Talyanskii, J. M. Shilton, M. Pepper, C. G. Smith, C. J. B. Ford, E. H. Linfield, D. A. Ritchie, and G. A. C. Jones. Single-electron transport in a one-dimensional channel by high-frequency surface acoustic waves. *Physical Review B*, 56:15180, 1997.

[VBC+17] L. M. K. Vandersypen, H. Bluhm, J. S. Clarke, A. S. Dzurak, R. Ishihara, A. Morello, D. J. Reilly, L. R. Schreiber, and M. Veldhorst. Interfacing spin qubits in quantum dots and donors—hot, dense, and coherent. *npj Quantum Information*, 3(1):34, 2017. Sparse qubit array with local electronics. Long-distance qubit coupling opens up space for local electronics that can control

a small dense qubit array. The estimated number of physical qubits required for solving relevant problems in quantum chemistry or code breaking is in the 106–108 range, using currently known quantum algorithms and quantum error correction methods.7, 8.

[VMW72] A.J. De Vries, R.L. Miller, and T.S. Wojcik. Reflection of a Surface Wave from Three Types of ID Transducers. *1972 Ultrasonics Symposium*, pages 353–358, 1972.

[WER+23] J. Wang, H. Edlbauer, A. Richard, S. Ota, W. Park, J. Shim, A. Ludwig, A. D. Wieck, H.-S. Sim, M. Urdampilleta, T. Meunier, T. Kodera, N.-H. Kaneko, H. Sellier, X. Waintal, S. Takada, and C. Bäuerle. Coulomb-mediated antibunching of an electron pair surfing on sound. *Nature Nanotechnology*, 18:721, 2023.

[WHZ+18] Matthias Weiß, Andreas L. Hörner, Eugenio Zallo, Paola Atkinson, Armando Rastelli, Oliver G. Schmidt, Achim Wixforth, and Hubert J. Krenner. Multiharmonic Frequency-Chirped Transducers for Surface-Acoustic-Wave Optomechanics. *Physical Review Applied*, 9(1):014004, 2018.

[WOE+22] J. Wang, S. Ota, H. Edlbauer, B. Jadot, P.-A. Mortemousque, A. Richard, Y. Okazaki, S. Nakamura, A. Ludwig, A. D. Wieck, M. Urdampilleta, T. Meunier, T. Kodera, N.-H. Kaneko, S. Takada, and C. Bäuerle. Generation of a single-cycle acoustic pulse: A scalable solution for transport in single-electron circuits. *Physical Review X*, 12:031035, 2022.

[WV65] R M White and F W Voltmer. DIRECT PIEZOELECTRIC COUPLING

TO SURFACE ELASTIC WAVES. *Applied Physics Letters*, 7(12):314–316, 1965.

[WW57] Gabriel Weinreich and Harry G. White. Observation of the Acoustoelectric Effect. *Physical Review*, 106(5):1104–1106, 1957.

[YAN+10] Yutaro Yamamoto, Shingo Akao, Hiroki Nagai, Toshihiro Sakamoto, Noritaka Nakaso, Toshihiro Tsuji, and Kazushi Yamanaka. Development of Multiple-Gas Analysis Method Using the Ball Surface Acoustic Wave Sensor. *Japanese Journal of Applied Physics*, 49(7S):07HD14, 2010.

[YFK+20] Masahiko Yokoi, Satoshi Fujiwara, Tomoya Kawamura, Tomonori Arakawa, Kazushi Aoyama, Hiroshi Fukuyama, Kensuke Kobayashi, and Yasuhiro Niimi. Negative resistance state in superconducting NbSe2 induced by surface acoustic waves. *Science Advances*, 6(34):eaba1377, 2020.

[YGK+16] G. Yamahata, S. P. Giblin, M. Kataoka, T. Karasawa, and A. Fujiwara. Gigahertz single-electron pumping in silicon with an accuracy better than 9.2 parts in 107. *Applied Physics Letters*, 109:013101, 2016.

[YSR+20] Tomoyuki Yokouchi, Satoshi Sugimoto, Bivas Rana, Shinichiro Seki, Naoki Ogawa, Shinya Kasai, and Yoshichika Otani. Creation of magnetic skyrmions by surface acoustic waves. *Nature Nanotechnology*, 15(5):361–366, 2020.

[YTB+12] Michihisa Yamamoto, Shintaro Takada, Christopher Bäuerle, Kenta Watanabe, Andreas D. Wieck, and Seigo Tarucha. Electrical control of a solid-state flying qubit. *Nature Nanotechnology*, 7(4):247–251, 2012.

[ZK03] Neil M Zimmerman and Mark W Keller. Electrical metrology with single electrons. *Measurement Science and Technology*, 14(8):1237, 2003.

Acknowledgment

First of all, I would like to express my heartfelt gratitude to my supervisor, Tetsuo Kodera. Since my undergraduate days, you have stimulated my curiosity, broadened my perspective, and wholeheartedly supported my passion for research. Whenever I faced uncertainty, you consistently guided me in the right direction. That I stand here today, enriched in spirit, is a testament to your significant influence. You have been the best supervisor for me.

I am endlessly grateful to Shintaro Takada. From you, I have learned not only experimental and fabrication techniques but also ways of thinking in the field of physics. The days spent with you at Tsukuba over the course of nearly five years have become a precious time in my life.

To everyone at Kodera Lab, I owe a great deal for the stimulating research discussions and emotional support. I extend my deepest thanks to Jun Yoneda, Raisei Mizokuchi, Ryutaro Matsuoka, Shimpei Nishiyama, and all the students of Kodera Lab. I am also thankful to the research support staff, Yuri Okuyama, Yukiko Hayashi, and Kaori Hashimoto, for always assisting.

I am grateful to Nobuhisa Kaneko, Michitaka Maruyama, Yuma Okazaki, Shuji Nakamura, Takehiko Oe, Yasuhiro Fukuyama, Daiki Matsumaru at the National Institute of

Advanced Industrial Science and Technology, for your daily advice and discussions regarding research and experimental equipment. I am thankful to Takahiro Mori and Kimihiko Kato for their immense help with electron beam lithography. I sincerely appreciate the enriching research environment provided to me. Furthermore, I would like to express my gratitude to Fusako Oyama for your support with various procedures and to Ikuhiko Saito and Yasuki Kawamura for the stimulating conversations we shared daily.

At Institute Néel, Christopher Bäuerle, Junliang Wang and Hermann Edlbauer had a significant impact on the quality of my SAW research. I am thankful for honing my skills and supporting me throughout the project. I am honored to have contributed to the outstanding achievements you have established. I am also grateful for Seddik Ouacel, Clément Geffroy, Aymeric Richard, and Lucas Mazzella, Matteo Aluffi making my two months at Institute Néel an even more remarkable experience.

My three-month stay at the University of Twente was an unforgettable and valuable experience. I thank W.G. van der Wiel for the warm welcome and Lorenzo Cassola for his support with the experiments. I also express my gratitude to the ”Everybody welcome to beer” group members, including Mohamadreza Zolfagharinejad, Reinier J.C. Cool, Emre Mulazimoglu, Marc Beuel, Femke J. Witmans, and Shaohua Kan, and dedicate beer to you all.

For my research on quantum annealers, which I started while experiments were not possible due to COVID-19, I really want to thank Tadashi Kadowaki and Ryunosuke Hamada at Denso, and Hidetoshi Nishimori. Their good advices based on theoretical physics and statistics provided me with a new perspective.

I owe a huge debt of gratitude to Tokyo Tech Academy for Super Smart Society

(WISE-SSS) and Cross the border! Tokyo Tech Pioneering Doctoral Research Project for making my PhD life fruitful. Without these support, I would not be here today.

Moreover, I am deeply thankful to the examiners who meticulously evaluated this thesis and my research.

My research has been made possible with the help of many people, and I would like to reiterate my sincere gratitude to everyone. Lastly, to my family, I express my profound appreciation for always supporting me unconditionally and without expecting anything in return.